



**UNIVERSITÀ DEGLI STUDI DI NAPOLI
FEDERICO II
POLO DELLE SCIENZE E DELLE TECNOLOGIE
FACOLTÀ DI INGEGNERIA**

— DIPARTIMENTO DI INGEGNERIA ELETTRICA —

**Theory, Design and Tests on a Prototype
Module of a Compact Linear Accelerator
for Hadrontherapy**

Daniele Davino

**Il coordinatore dei Corsi di Dottorato e Tutore
Prof. Luciano De Menna**

**TESI DI DOTTORATO DI RICERCA
IN INGEGNERIA ELETTROTECNICA**

XIII Ciclo

Contents

Introduction	iii
Chapter 1. Introduction to the Hadrontherapy	1
1. Some definitions on Radiation for Cancer	1
2. Advantages of Hadrontherapy	3
3. Hadrontherapy in the world	4
Chapter 2. Linac and SCL Accelerators	7
1. Fundamental definitions	8
2. Linear accelerators	11
3. SCL structures	14
4. LIBO Specifications	16
Chapter 3. Design Techniques for a Side Coupled Linac	23
1. Global Parameters of the Accelerator	25
2. Analysis of Coupled Cavities	27
3. Single cavity design	29
4. Bridge Couplers design	35
5. Coupling between Waveguide and Bridge Coupler	37
Chapter 4. Circuit Model	45
1. Transmission matrix representation	45
2. The perturbed transmission matrix	52
3. The perturbed resonant frequency	56
4. The perturbed axial field	59
5. Conclusion	64
Chapter 5. Radiofrequency Measurement	67
1. Introduction	67
2. RF Measurement on a single cavity	69
3. RF Measurement on coupled cavities	75
4. Bead pulling measurement	80
5. A tuning procedure for the LIBO module	83
6. The final steps of the tuning procedure	89
7. Measurement of the coupling between the module and the waveguide through an iris	92
Conclusions and Outlook	99
Bibliography	103

List of Figures	105
Acknowledgements	109

Introduction

This PhD thesis deals with the study and the development of the radiofrequency design of a module prototype for a linear accelerator intended to be used for hadrontherapy, a powerful cure of cancer.

Hadrontherapy is one of the most promising cures of cancer of which the scientific community is discussing about. The idea is to irradiate the tumor zone with a proton beam with a variable energy included within 60 and 250 MeV. This range allows the cure of deep tumors. The use of protons leads to a better distribution of the radiation dose in the tumor zone and to a lower dose delivered to the safe tissues.

This property is due to a physical phenomenon known as *Bragg's Peak*: the particles penetrate in the tissue and deliver the most part of their energy at a certain distance, the value of which depends on the initial energy. This fact, together with the improved 3D conformal techniques allowing a precise description of the target, gives a clear improvement of cancer treatment.

The hardest points in the development of an accelerator for such a purpose are the production costs and the overall dimensions of the structure. Both points are necessary for a feasible installation in medical centers and hospitals.

The first point can be partially solved if one thinks of a structure that uses already existing elements. For example, in several medical centers, small cyclotrons are already present and delivering a beam with an energy up to about 60 MeV. Such a beam is used either for the production of isotopes for medical purposes or for the treatment of superficial tumours, as the eye ones. Then, an accelerator which boosts the beam energy of a cyclotron can be used, rather than to use a bigger superconductive cyclotron which should be a more expensive solution.

The second requirement can be satisfied with the use of an high frequency compact linear accelerator. At the same time, this linear accelerator has to need few external components as the radiofrequency generators (klystrons) for example, and does not have to need expensive mechanical machining and complex tuning procedures.

The best compromise to satisfy these requirements seems to be the Side Coupled Linear Accelerator. The accelerator subject of this PhD thesis, LIBO (LInear BOoster), is of this type and it has been thought to be a modular structure; in fact the study has been made only for the first of nine modules, with the idea to deal with a proof of principle.

In the state of art of the linear accelerator design, many aspects are involved: the theoretical design, the numerical design and the experimental verification, namely the radiofrequency measurement. In this thesis all the aspects are covered, sometimes with less details and sometimes with more. This is due to the own nature of the work. It was developed during the effective design and construction of the module, up to all the practical details a construction needs, and for time reasons, sometimes the more known classical techniques were preferred. Nevertheless, several scientific ideas have come out in sight of an industrial productions of LIBO. First, the possibility to apply engineering criteria to the design; then, the possibility to have automatic measurement which should not need high qualified human contribution. All these points are stressed where it is the case.

Finally, we would spend some words about the agencies involved in this project. First the TERA Foundation, directed by Prof. U. Amaldi, where the first ideas were born. Then, the CERN in Geneva, where the most part of the construction and measurement has been made and where the project team was used to gather (the author has been spent almost the half part of his PhD at CERN). Next, INFN Sez. di Milano e Napoli who gave money and people to work on this project, and last but not least, the Dipartimento di Ingegneria Elettrica in Naples that has a good tradition in accelerator development and where the author has the privilege of doing his PhD.

In the **first chapter** a short introduction to the hadrontherapy is presented with a description of the main medical centers in the world that use hadrontherapy.

In the **second chapter**, we deal with an introduction to the linear accelerator, with the definition of the main parameters involved and the characteristics of coupled cavities. Particular emphasis is paid to the side coupled structure. In this chapter it is also presented LIBO structure with the radiofrequency, beam dynamic and mechanical aspects stressed as well.

In the **third chapter** the effective radiofrequency design of a side coupled linac with a *top-down* methodology is shown. All the aspects are covered: from the first numbers involved, up to the definition of the single cavities details, while in the **fourth chapter** a circuit model is presented which has the aim to give the sensitivity of the main parameters to mechanical tolerances. Numerical results are shown as well.

In the **last chapter** a detailed description of radiofrequency measurement on the prototypes is illustrated. Some innovative approaches are presented on the measurement of coupled cavities and a flux diagram of both mechanical and measurement procedure is commented.

CHAPTER 1

Introduction to the Hadrontherapy

In this chapter we will shortly introduce the basic principles of hadronic¹ radiotherapy.

In this sense, we will illustrate the advantages connected to the use of protons which leads, with respect to the conventional techniques, to an improvement on the safe of sane tissues and on the destruction of tumour zone.

A short introduction to the principal medical centers in the world which are dedicated to the cancer research is presented as well.

All the definitions and information concerning this chapter can be found in [1, 2, 3].

1. Some definitions on Radiation for Cancer

In the world, cancer is one of the most dangerous diseases. Cancer is the uncontrolled growth and proliferation of cells in the body, the triggering of which is not yet fully understood.

Radiation therapy and surgery are the main forms of localized treatments that are used to eliminate the primary tumour. Secondary tumours, originating from the primary, are usually treated by chemotherapy.

By careful planning, choice and manipulation of the treatment beams, radiation preferentially destroys cancer cells and spares normal healthy tissue.

The total radiation dose² is often divided into small daily *fractions* as this results in better tumour control.

About half of all cancer sufferers need to undergo radiation therapy at some stage during their treatment. Even modest advances in the therapies will improve the quality of life of a large number of people.

Hospitals operate cobalt machines and linear accelerators which produce photon and electron beams. These are ineffective for some tumours, particularly advanced or slow-growing ones and proton therapy

¹Hadrons are subatomic particles. Radiotherapy hadrons include protons, neutrons, pi-mesons and a few heavy ions, i.e. electrically charged atoms, as Helium, Carbon, Oxygen, etc.

²The dose is radiation energy deposited per unit volume; it is measured in Gray (Gy): 1 Gray equals 1 Joule per kg. In conventional tumour radiotherapy typical doses are in the range of 40 to 70 Gy applied over a period of about 10 to 30 days.

may be the only effective treatment, sometimes in conjunction with surgery.

It may not be possible to irradiate some lesions with these conventional beams or to remove them surgically because of the proximity of critical tissues and proton therapy may be the only possible form of treatment.

If neutron or proton beams are not available the alternatives are very expensive chronic medical care or treatment at overseas centers.

Radiation therapy machines are expensive, high technology equipment, but the advantages are

- A sterile environment is not required.
- Few people are involved in patient treatment, which does not necessarily require the daily presence of a Radiation Oncologist or any other clinician.
- Most patients are treated as out-patients and therefore do not occupy scarce and expensive hospital beds.
- Irradiation is not traumatic for patients, who are not anaesthetized and usually do not get sick from the treatment.

Radiation therapy is therefore cost-effective and often cheaper than the alternatives of surgery, chemotherapy and chronic health care.

Neutrons and protons are both nuclear particles of approximately the same mass. However, the fact that neutrons are uncharged and protons are charged particles results in their having vastly different physical properties and biological effects. Using conventional photon radiation as the standard, the dose distributions of fast neutrons are very similar, but their biological effects offer advantages for the treatment of certain types of tumours, while the advantages of protons lie in their physical dose distributions.

Many large tumours have central cores, which lack oxygen because the blood supply has been reduced by the proliferating tumour cells. Other tumours are slow-growing and the cells spend a relatively short time in the dividing phase of the cell cycle, where they are most sensitive to radiation. These tumours are resistant to conventional photon radiation but are far less resistant to neutron irradiation, which therefore in principle has a better chance of effecting a cure. Examples of tumours that are effectively treated by neutrons include salivary gland tumours, large breast tumours and certain tumours of other soft tissues. However, because radiation causes damage to the normal tissue in front of a deep-seated tumour, a so-called isocentric beam delivery system (one which rotates about the patient) is essential so that the patient can be irradiated from several different angles. This concentrates the dose at the tumour and limits the dose to normal tissue.

High energy protons are particularly suitable for treating cancer or other (benign) abnormalities near sensitive structures such as the optic nerve, spinal cord, kidneys, etc., where other forms of radiation

would do too much damage to healthy tissue. This feature results from the fact that protons can be steered and focused very accurately and can also be given exactly the right energy to stop at any particular point within the body, thus completely protecting any organs beyond this range. They also allow better protection of normal tissue situated in front, and at the sides, of the target than other types of radiation. This allows the application of higher doses to a tumour which means a better chance of cure. The high precision required in proton therapy demands the ability to accurately set the patient up in the proton beam. Although not as important as in the case of neutron therapy, the ability to irradiate the patient from different angles is desirable.

2. Advantages of Hadrontherapy

In the history of radiation therapy there are many examples of how cure rates have been increased through improvements in physical dose distribution and the resulting increase in feasible tumor dose.

In deep-seated tumours, the change from x-ray based therapy to the use of electrons beams coming from high energy accelerators has yielded an appreciable improvement in therapeutic results; in many cases, however, an exact fit of the irradiated volume to the target volume is impossible due to the physical characteristic of the gamma rays used in therapy. For such a beams, after a short build-up, the dose decreases at greater depth, and, for deep-seated tumours, the integral dose is always lower than the one released to the healthy tissues. On the other side, beams of charged particles (protons and ions) produce a much more agreeable dose distribution. In fact, due to a phenomenon known as Bragg peak, for both protons and ions, the delivered dose increases at greater depth and then declines abruptly behind a sharply peak which is the maximum of dose, as in figure 1.1 where it is shown the curves dose-depth for 200 MeV protons, 20 MeV electrons and for gamma-rays.

From the figure 1.1 it is also clear that the peak is rather shorter, but the location of that maximum can be precisely fixed by the energy of the particles. In such a case is possible to *sum* the shorter peaks to cover wider region. This is the so called *Spread out Bragg peak* as it is shown in figure 1.2.

Finally, protons and ions exhibit a small lateral and range scattering, which is another prerequisite for achieving a tumor conform treatment.

These physical properties of charged-particle beams lead to a substantial improvement in the tumour dose with respect to the integral dose delivered to healthy tissues. This means that healthy tissues are much more spared and this could be a real advantage in radiotherapy for young patients, for example, whose long life expectancy mandates

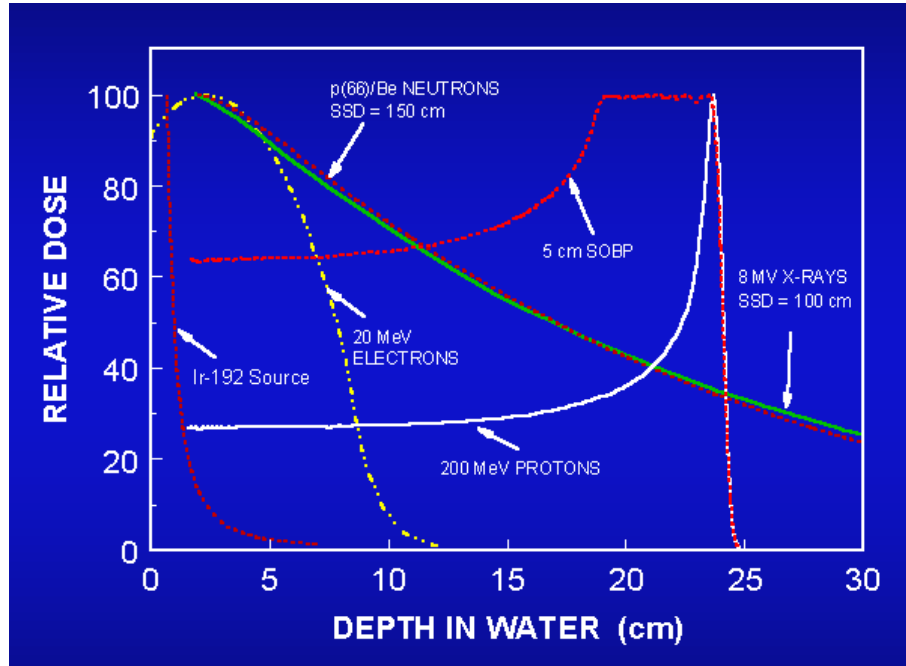


FIGURE 1.1. The Bragg peak phenomenon. Comparison between proton and electron penetration depth in water. Also shown is a proton depth dose curve with a spread-out Bragg (SOBP) of 5 cm.

that the risk of late effects, as radiation-induced tumors, should be minimized.

3. Hadrontherapy in the world

The first proposal to use protons for tumor therapy was put forward in 1947 by Robert Wilson and pioneer treatments started in 1954 at the Lawrence Berkeley Laboratory (USA). At present, protontherapy centers are located in the United States, in Russia, in Japan, in South Africa and in Europe. Most of the clinical experience has so far been obtained at physics research institutions which have devoted part of the accelerator time to medical uses.

Loma Linda is one of the first hospital-based proton radiotherapy facility for treatment of deep-seated tumors. In figure 1.3 a sketch of the radiotherapy center is shown.

The table 1.1 shows the main center in the world that use hadrontherapy, the source is from the site:

<http://neurosurgery.mgh.harvard.edu/hcl/ptles.htm>

and it is updated to July 2000.

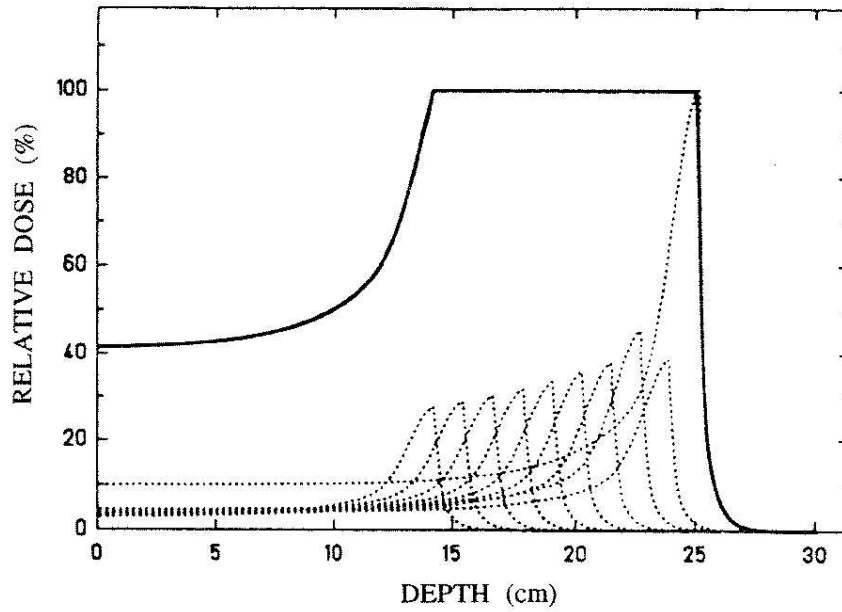


FIGURE 1.2. The Spread out Bragg peak. Combining beams with different energies it is possible to describe a longitudinal profile.



FIGURE 1.3. A sketch of Loma Linda radiotherapy center in California.

Who	Where	What particle	First RX	Last RX	Total patient	Date of total
Berkeley 184	CA. USA	p	1954	-1957	30	
Berkeley	CA. USA	He	1957	-1992	2054	6-91
Uppsala	Sweden	p	1957	-1976	73	
Harvard	MA. USA	p	1961		8558	7-00
Dubna	Russia	p	1967	-1974	84	
Moscow	Russia	p	1969		3268	6-00
Los Alamos	NM. USA	p	-1974	-1982	230	
St. Petersburg	Russia	p	1975		1029	6-98
Berkeley	CA. USA	heavy ion	1975	-1992	433	6-91
Chiba	Japan	p	1979		133	4-00
TRIUMF	Canada	p	-1979	-1994	367	12-93
PSI (SIN)	Switzerland	p	-1980	-1993	503	
PMRC, Tsukuba	Japan	p	1983		629	7-99
PSI (72 MeV)	Switzerland	p	1984		3014	12-99
Dubna	Russia	p	1987		58	6-00
Uppsala	Sweden	p	1989		236	6-00
Clatterbridge	England	p	1989		999	6-00
Loma Linda	CA. USA	p	1990		5262	7-00
Louvain-la-Neuve	Belgium	p	1991	-1993	21	
Nice	France	p	1991		1590	6-00
Orsay	France	p	1991		1527	12-99
N.A.C.	South Africa	p	1993		367	6-00
MPRI	IN USA	p	1993		34	12-99
UCSF - CNL	CA USA	p	1994		284	6-00
HIMAC, Chiba	Japan	heavy ion	1994		745	12-99
TRIUMF	Canada	p	1995		57	6-00
PSI (200 MeV)	Switzerland	p	1996		41	12-99
G.S.I. Darmstadt	Germany	heavy ion	1997		72	6-00
Berlin	Germany	p	1998		105	12-99
NCC, Kashiwa	Japan	p	1998		35	6-00
				pions	1100	
				ions	3304	
				protons	27434	
				Total	31838	

TABLE 1.1. World Wide charged particle patient totals. Source updated to July 2000: <http://neurosurgery.mgh.harvard.edu/hcl/ptles.htm>.

CHAPTER 2

Linac and SCL Accelerators

The physics and technology of particle accelerators have been highly developed over the past fifty years. After the second world war, particle accelerators have been mainly used for experimental nuclear and particle physics research. The development of accelerators has the merit to demand new technologies, which are necessary to have more powerful accelerators, and these new technologies can be used in other fields¹.

Linear accelerators, also called *linacs*, were often used in the past as the first step of acceleration before large circular machines. Nowadays the linacs are appointed to be used for the next generation of accelerators: the linear colliders, since their output beam can be of high quality² and high energy. But linacs can be applied also to other purposes and the medical applications of linacs are only one example, surely the most noble, of the several cases where these accelerators can be used out of the high energy physics field.

Furthermore, the capability to be realized in the range of few meters to kilometers sizes and in the costs range from a few millions to a billion euro renders this type of accelerators very promising for intensive industrial applications.

In the beginning of this chapter only a short review on linear accelerators is presented, since in the scientific literature lots of publications, both articles and book, are dedicated to the explaining of the various linear accelerators types. For this reason, in the following there is always the reference to publications where the argument presented is fully explained.

In the first paragraph the principal definitions and concepts involved in linear accelerators are reminded, while in the following two, after a short historical review, the principal structures are illustrated with a particular emphasis on the Side Coupled Linac structure.

In the last paragraph a first general presentation of the accelerator object of this thesis work, LIBO project, is shown with all the principal

¹Consider the www (world wide web) born in the early 80's at CERN for example.

²High beam quality means small beam diameter and small beam energy spread. Other advantages of linacs can be: strong focusing easily reachable, no power losses for synchrotron radiation, injection and extraction are simpler then for circular machines, linacs can operate at any duty factor.

parameters involved; also a short review on LIBO particles dynamic and on mechanical aspects is presented.

1. Fundamental definitions

To accelerate particles we use an electric field; this properties is represented through the Lorentz Force equation

$$\vec{F} = q(\vec{E} + \vec{v} \times \vec{B})$$

which gives the force acting on a point charge q in the presence of electromagnetic field.

The first idea to have particles accelerated by a longitudinal electric field is to use a circular waveguide operating in the mode TM_{01} , but in this case the phase velocity of the field is greater than the velocity of light and the particles would never have synchronism with the electromagnetic wave, and therefore no continuous acceleration.

Then, we need to lower the phase velocity. One way could be to charge the waveguide with equally spaced disks, let us call L the distance between disks. The study of such a structure is based on two fundamental points:

- *Floquet's Theorem*: In a lossless spatial periodic structure, the wave function is periodic too and it may differ from a period to the next only by a factor like e^{-jkL} .
- The boundary conditions cannot be satisfied by a single mode of the structure and there is a continuous spectrum of *space harmonics* (Fourier series).

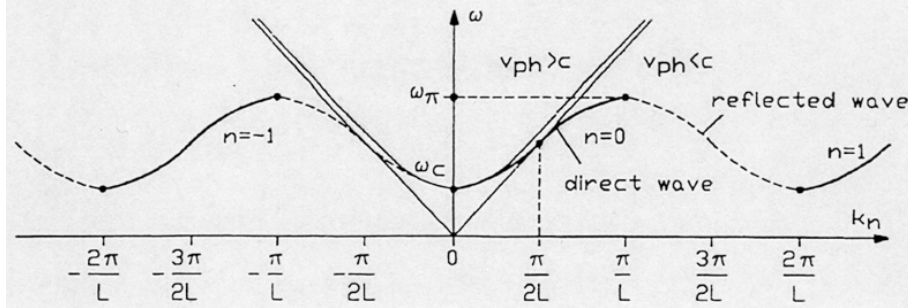


FIGURE 2.1. Dispersion diagram of a periodic structure (loaded waveguide); unloaded cavity case is shown for comparison.

Interesting features are observable in figure 2.1, which shows the dispersion diagram of an infinite periodic structure and, for comparison, the diagram of an infinite wide waveguide:

- There is a limited passband effect between ω_c and ω_π . The frequency range of passband is related to the coupling between cavities.

- For a given frequency, there is an infinite series of space harmonics, with the same group velocity, but with different phase velocity.
- When the electromagnetic energy flows only in one direction we deal with the solid part of the curve on the diagram and the structure is a *travelling wave* accelerator (TW); when the energy flows in both direction, we deal with solid and dotted part of the curve and the structure is said *standing wave* accelerator (SW).
- Travelling wave accelerators operate near the middle of the passband, where group velocity is maximum and the mode spacing is biggest.
- Standing wave accelerators operate on lower or upper end of the passband, because only there the *direct* and *reflected* wave have the same phase velocity, and therefore could accelerate particles.

The behavior changes for the case of a finite number of coupled cavities. Let us find the resonant modes of a chain of $N + 1$ coupled cavities as sketched in figure 2.2.

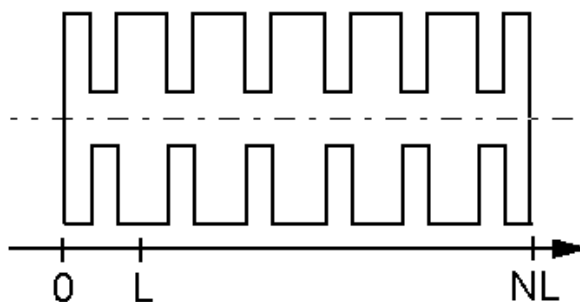


FIGURE 2.2. $N + 1$ coupled cavities. The first and last cells are half cavities which act as an *electric mirror* for the boundary conditions.

The structure is NL long, periodic of a period L and it is bounded on two half cells which act as *electric mirrors* for the boundary conditions. In a resonant condition, in the structure there are a backward wave E_z^- and a forward wave E_z^+ .

The imposition of boundary conditions gives the resonant modes of the whole structure.

$$\begin{cases} z = 0, & E_z^-(0) = E_z^+(0), \\ z = NL, & E_z^-(NL) = E_z^+(NL) \rightarrow E_z^-(0)e^{-jN\phi} = E_z^+(0)e^{jN\phi}, \end{cases} \quad (2.1)$$

where ϕ is the phase advance for one period L . From the previous (2.1), one obtains $N + 1$ solutions for ϕ

$$\phi^{(n)} = \frac{n\pi}{N}, \quad n = 0, 1, \dots, N \quad (2.2)$$

Therefore the phase advance assumes only a discrete set of values. There are $N + 1$ solutions, each of them is called *resonant mode* of the structure and it is characterized by its phase advance. The Brillouin diagram is sampled in these cases, as it is shown in figure 2.3. It is apparent that for $N \rightarrow \infty$ the curve becomes continuous again.

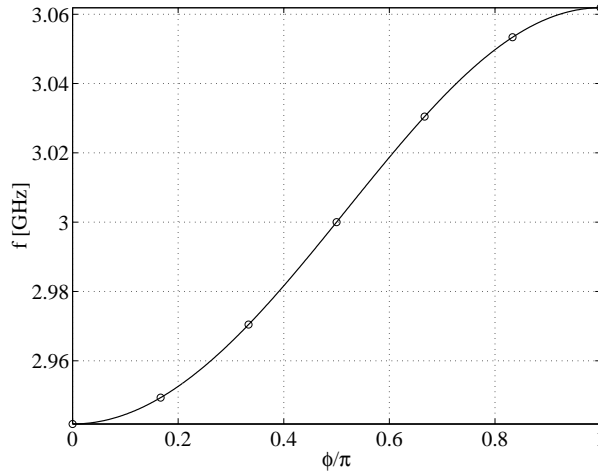


FIGURE 2.3. $N = 7$ coupled cavities. The Brillouin diagram is sampled in 7 frequencies. We can recognize modes 0 , $\pi/2$ and π .

Let us give some definitions on single cavities. There are several figure of merit that are used to characterize the single cavity. The first one, which is also used as a parameter in the equivalent lumped circuits, is the *quality factor*, defined as

$$Q = \omega \frac{W}{P}, \quad (2.3)$$

where ω is the resonant pulsation, W is the stored energy in the cavity and P is the average power loss in the cavity. Another important parameter is the *shunt impedance* defined as

$$R_{sh} = \frac{\left| \int_0^L \mathbf{E}_z(z) dz \right|^2}{2P}, \quad (2.4)$$

that is the ratio between the voltage on the axis of the cavity and the power loss³. Since the power dissipation is proportional to the square of the field, the R_{sh} is independent of the field level. This parameter does not take into account the velocity of the particles, where the *transit time factor* T does it:

$$T = \frac{\left| \int_0^L \mathbf{E}_z(z) e^{-j\omega z/v_p} dz \right|}{\int_0^L \mathbf{E}_z(z) dz}, \quad (2.5)$$

T is a measure of how efficiently a cavity, with an electric field \mathbf{E}_z along the axis, can accelerate particles of velocity $v_p = \beta c$; it is independent of the amplitude \mathbf{E}_z and it is always smaller than unity; L is the length of the acceleration gap.

If one makes the hypothesis that $\mathbf{E}_z(z) = \frac{V_0}{L} \sin(\omega_0 t + \phi)$ where $\omega_0 = \frac{2\pi c}{\lambda_0}$ and ϕ is an unknown phase, then the transit time factor is

$$T = \frac{\sin \frac{\pi L}{\lambda_0 \beta}}{\frac{\pi L}{\lambda_0 \beta}}, \quad (2.6)$$

and the smaller the argument is, the bigger is T ; for example, T approximates the unity when the acceleration gap L goes to zero.

The product of the shunt impedance to the squared transit time factor is called *effective shunt impedance* and is defined as

$$R_{\text{eff}} = R_{sh} \cdot T^2. \quad (2.7)$$

All these parameters can be defined per unit length of the cavity. Another relevant parameter, that it is important for RF measurement, is the ratio of shunt impedance to quality factor, often called *r over Q*: this parameter is independent of amplitude of the field and of power loss. It depends only on geometry of the cavity and can be easily measured on scaled prototype.

Adequate support on these definitions and more can be found in the references [12, 13, 14, 15, 16].

2. Linear accelerators

Starting from the first theoretical proposal for a linac made by Ising in 1924 [5] which inspired the work and realization of Wideröe in 1928 [6], the linear accelerators has known a big development aimed

³Note that this definition has a factor 2 in the denominator, this is made in analogy with circuit theory and it is typical of linacs theory.

at a differentiation of the structure with respect to the type and the velocity of the particles.

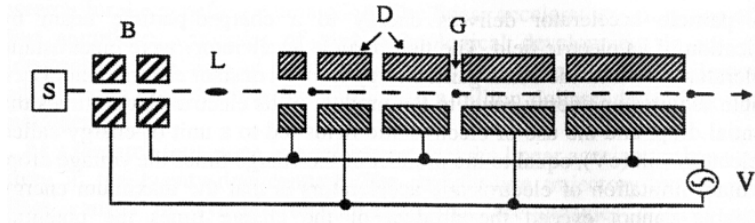


FIGURE 2.4. Schematic view of the Wideröe drift-tube linac. D are drift tubes, V is an alternating voltage source, G are the gaps between the drift tubes and S is the source of a continuous beam. B are used to group the particles in bunches.

The Wideröe linac concept was to apply a time-alternating voltage to a sequence of drift tubes whose lengths increased with the particles velocity, so the particles always arrive synchronously at each gap between tubes. In figure 2.4 a schematic view is presented, D are drift tubes connected to an alternating voltage source V that applies equal and opposite voltages to sequential drift tubes, G are the gaps between the drift tubes in which the electric force acts to accelerate the particles, and S is the source of a continuous ion beam. For efficient acceleration the particles must be grouped into bunches, shown by the black dots, which are injected into the linac at the time when the polarity of the drift tubes is correct for acceleration. The bunching can be accomplished by using an RF gap B between the DC source and the linac. The original Wideröe linac concept was applicable to heavy ions and not suitable for acceleration to high energy of lighter protons and electrons where the drift-tube lengths and the distances between accelerating gaps would be too large, resulting in a small accelerating rates, unless the frequency of accelerating field could be increased up to 1 GHz. But in this range of frequencies the wavelengths are comparable with the sizes of the drift tubes and propagation and radiation effects should be included in the design.

Linear accelerators are *quasi-periodic*⁴ structures where the single elements, which could be resonant cavities, are coupled together either electrically or magnetically.

2.1. Disc-loaded structure. It is often used for electrons. Starting from the idea that the electric field in a uniform circular waveguide cannot provide continuous acceleration of electrons, since the phase velocity always exceed the velocity of light, one can think to lower the

⁴The structure is quasi-periodic, since the longitudinal dimension of the single element has to be adequate to the increased particle velocity during the travel.

phase velocity of the uniform waveguide by loading it with a periodic array of conducting disks with axial holes.

From the electromagnetic point of view, it is a chain of cavities coupled, either electrically (through the beam holes) or magnetically (through coupling slots). Disc-loaded structures operate in the *traveling wave* and *standing wave* regime. In the first case phase advance bigger than $\pi/2$ are used, since the group velocity and the mode spacing are bigger too. In the standing wave case, the structure mode is π . The used frequency range is around 0.5 to 3 GHz.

2.2. Alvarez or drift tube linac (DTL). Alvarez and his group proposed in 1946 a linear array of drift tubes enclosed in a high quality factor cylindrical cavity [7, 8]. This structure is normally used to accelerate protons and other ions in the velocity range from 0.04 to 0.4 times the velocity of light.

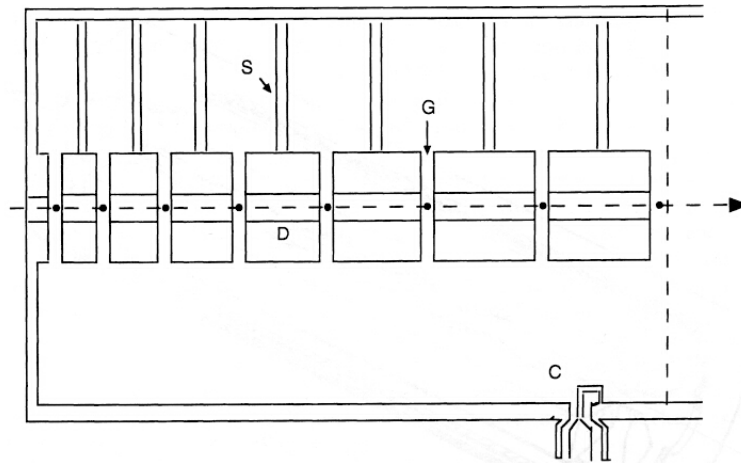


FIGURE 2.5. Schematic view of the Alvarez drift-tube linac. The beam particles are bunched before injection into the drift-tube linac. The beam bunches are shown being accelerated in gaps G. They are shielded from the wrong polarity field by the drift tubes. These ones are supported by the stems S. The whole cavity is excited by the RF current flowing on a coaxial line into the loop coupler C.

In figure 2.5 a schematic view of Alvarez drift-tube linac is shown.

The Alvarez drift-tube linac is a *Standing Wave* accelerator and operates in the 0 mode. The electric and magnetic fields are in phase in adjacent cells and the separating walls are not necessary and this fact increases the shunt impedance. In the drift tubes magnetic quadrupoles are housed for beam focusing.

2.3. Side-Coupled drift tube linac (SCDTL). The use of drift tubes in the GHz frequency range requires very small dimensions, where quadrupole cannot be placed. The *SCDTL* structure resolves the problem [9, 10] since quadrupoles are placed between cavities with only a few drift tubes. To propagate the electromagnetic field, the accelerating cavities are coupled via coupling cells placed out of axis and near the quadrupole magnets, see figure 2.6

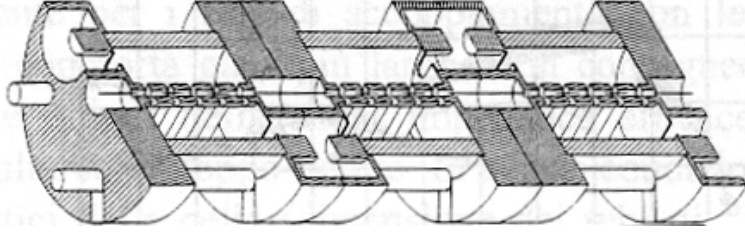


FIGURE 2.6. Schematic view of the Side Coupled Drift-Tube Linac.

3. SCL structures

The Side Coupled linac is a standing wave accelerator where a biperiodic chain of cavities, often called cells, operates in the $\pi/2$ mode; it was developed in the National Laboratory of Los Alamos for the first time [18]. This mode of operation has the disadvantage of cells without field which do not participate to the acceleration, but it has the great advantage of a rejection to the disturbs and errors of fabrication [14].

The Side Coupled Linac is only one of the possible realizations of biperiodic chain operating in the $\pi/2$ mode. All the solutions are shown in figure 2.7 and wide explications on the advantages and disadvantages can be found in [19]. From mechanical and radiofrequency point of view, the SCL seems to be the best compromise to realize it.

For protons, the structure operates in the range of gigahertz and it is used for energy of protons around and beyond 100 MeV. For these particle, the accelerating cavities have noses around the beam aperture in order to increase the transit time factor T and this implies that a low electric coupling through the apertures is available; then, a magnetic coupling is ensured through the coupling cells which are out of axis in order to augment the acceleration per meter efficiency, the coupling cells being without field inside in the normal condition of operation. By this way, the field-stability advantages of the $\pi/2$ mode can be combined with the shunt impedance advantage of the π mode, through the introduction of such a biperiodic coupled-cavities structure.

The coupling between accelerating and coupling cells is called *nearest neighbour coupling* and it is indicated with k or k_1 ; the coupling between accelerating cells is called *next nearest neighbour coupling* and it is indicated with k_2 and normally it is one unit factor below k_1 . There

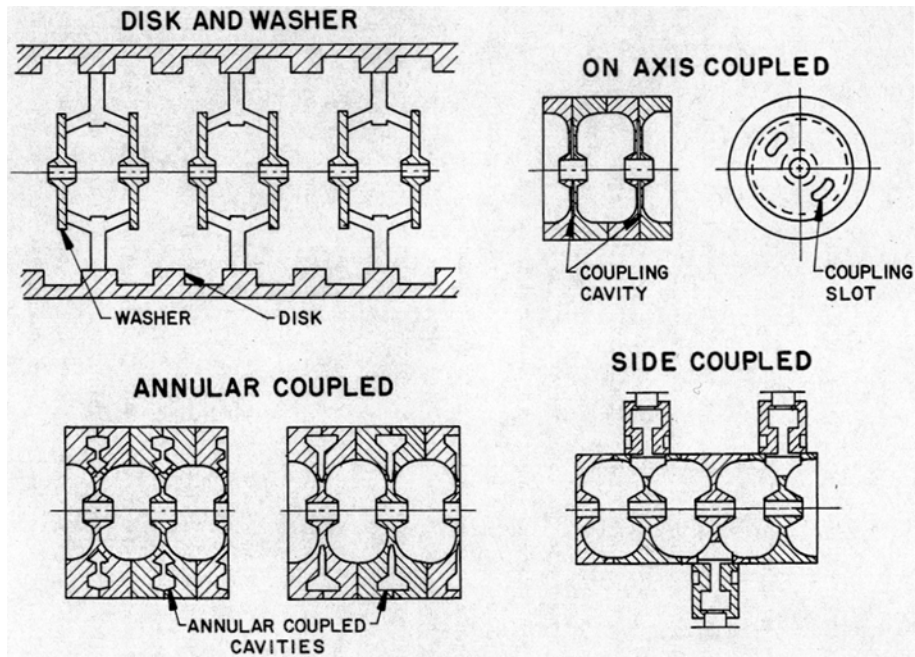


FIGURE 2.7. Different solutions for the realization of a biperiodic chain of cavities.

is also a next nearest neighbour coupling between coupling cells k_3 but this is really negligible since the coupling cells are normally placed in opposite sides, see figure 2.8.

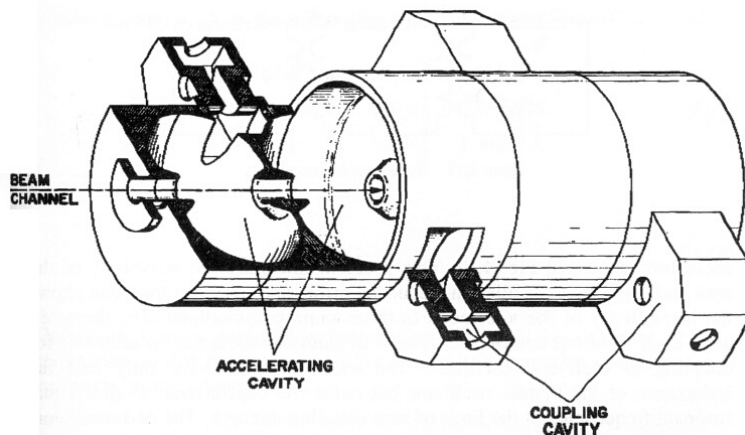


FIGURE 2.8. A Side Coupled Linac example. The cavities on the beam axis are accelerating cavities. The cavities on the sides couple the accelerating ones and are nominally unexcited.

When dealing with biperiodic structure, one has to pay attention to the *stop-band* concept. Consider a chain of $2N$ cavities with frequency f_c which alternate with $2N + 1$ accelerating cavities with frequency

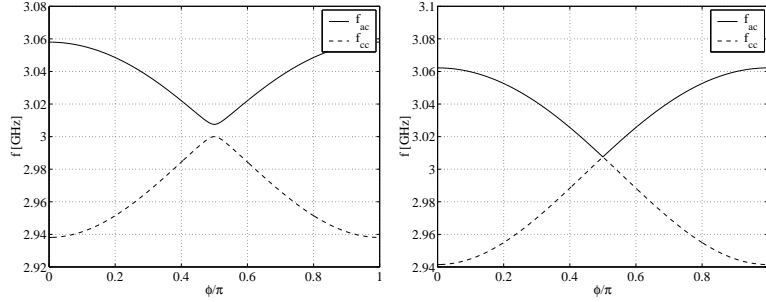


FIGURE 2.9. The dispersion diagrams in the case of a biperiodic structure with $f_a = 3$ GHz, $f_c = 3$ GHz, $k = 0.04$, $k_2 = 0.005$ and $k_3 = 0$ on the left and $f_c = f_a/\sqrt{1 - k_2}$ on the right.

f_a ; the total number of cavities is therefore $4N + 1$. The coupling between accelerating and coupling cavities is k , between non-adjacent accelerating cells is k_2 , and between coupling cells is k_3 . With the hypothesis of infinite quality factor, the dispersion formula is [14]

$$k^2 \cos^2 \phi = \left(1 - \frac{f_a^2}{f_q^2} + k_2 \cos 2\phi\right) \left(1 - \frac{f_c^2}{f_q^2} + k_3 \cos 2\phi\right), \quad (2.8)$$

where ϕ is the phase advance. In the previous section we saw that for a finite structure the phase advance can assume only a finite set of values, the number of which is equal to the number of resonators. The previous relation (2.8) shows that there are two solutions for the $\phi = \pi/2$ frequency:

$$f_{\pi/2}^{ac} = \frac{f_a}{\sqrt{1 - k_2}}, \quad f_{\pi/2}^{cc} = \frac{f_c}{\sqrt{1 - k_3}},$$

that deals to a forbidden range of frequency, which is the *stop-band*, as it is shown in figure 2.9 (left). If $k_2 = 0$, then it is sufficient to choose $f_a = f_c$, where if $k_2 \neq 0$ one has to choose $f_c = f_a/\sqrt{1 - k_2}$, the result of this second case is shown in the figure 2.9 (right).

4. LIBO Specifications

LIBO is a 3 GHz side coupled proton linac. It was conceived as a *LInac BOoster*⁵, intended to be mounted downstream of a cyclotron of about 60 MeV (of which many exist in hospitals and physics laboratories), with the aim to *boost* the energy of the proton beam up to 200 MeV, an energy needed for therapy of deep seated tumors. All the matters concerning this section are reported in [22, 23, 24, 25].

The beam intensity needed for protontherapy is relatively small, about $2 \cdot 10^{10}$ particles per second, i.e. a few nanoamperes, while the

⁵This is the origin of word *LIBO*.

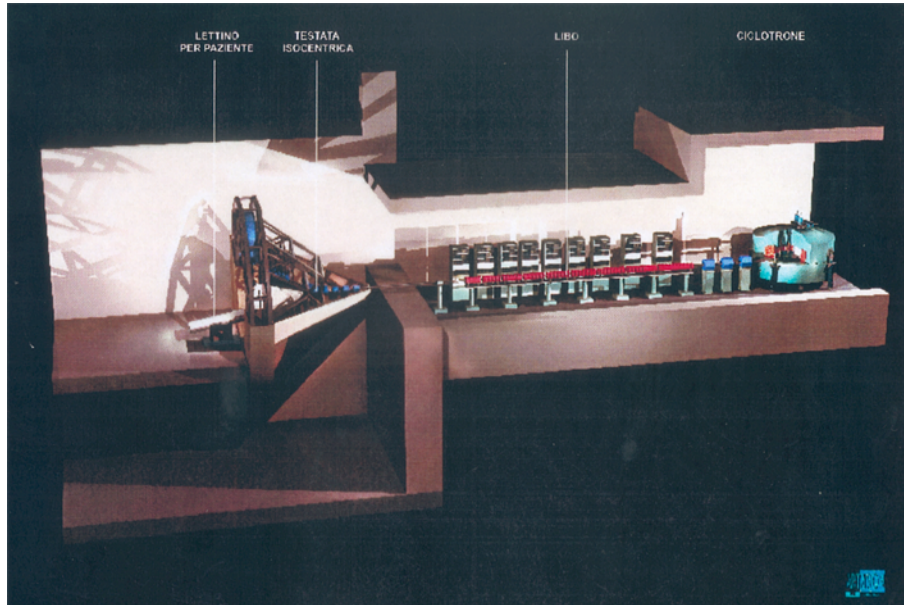


FIGURE 2.10. A perspective image of a LIBO installation.

cyclotron current is usually much bigger ($50 \div 100 \mu A$). This current can be pulsed at the LIBO repetition rate (400 Hz) and even with a small capture efficiency, enough beam passes through the 8 mm diameter of the cavities beam hole to result in an average output current as needed for deep therapy. In figure 2.10 a perspective image of a LIBO installation is presented.

LIBO as been laid out as a modular structure, composed of nine modules, each of which, fed by its own RF power supply, can be considered as an independent RF unit. All the modules are conceptually identical, except for the slight progressive change in length, in agreement with the increased velocity of protons, accelerated from 62 to 200 MeV (the relativistic β varies from 0.35 to 0.566). The simplified drawing of the first LIBO module is shown in figure 2.11.

A module is composed of 4 tanks, and each tank of 13 accelerating and 12 coupling cells. In order to simplify the mechanical construction, all the accelerating cells in a tank are of the same longitudinal length and all the coupling cells in a module are the same. The design of the cavities for LIBO is presented at page 33. In figure 2.12 a drawing of a LIBO tank is presented. In between the tanks are placed the focusing permanent magnet quadrupoles (PMQ), all of them identical.

The tanks in a module are connected, from an electromagnetic point of view, via Bridge Couplers; the RF power input is located in the central Bridge Coupler, while the other two contain pumping vacuum ports. The specific design of the LIBO Bridge Couplers is presented at page 35. In table 2.1 the main parameters of LIBO are presented.

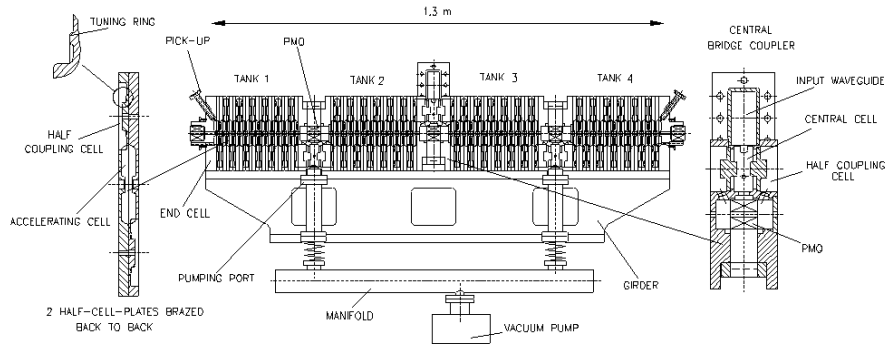


FIGURE 2.11. The layout of the first module of LIBO, with details of a half-cell-plate (left) and of a bridge coupler (right).

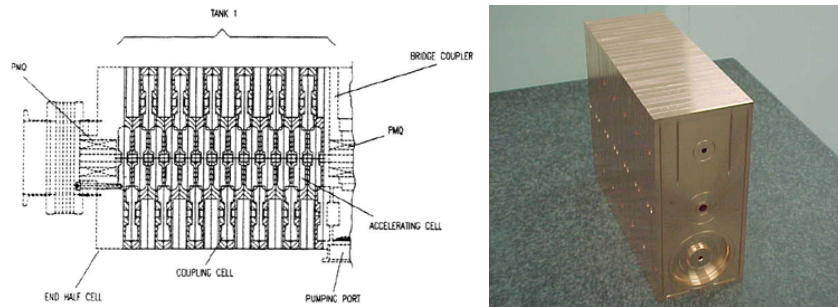


FIGURE 2.12. Drawing of the first tank of first LIBO module (left). The first tank after the brazing (right).



FIGURE 2.13. Half-cell-plates showing a coupling half cell (left) and an accelerating half cell (right). Note the coupling slot.

4.1. Short hints on LIBO beam dynamic. In LIBO structure a high average axial accelerating gradient E_0 (15.3 MV/m) has been selected to limit the accelerator length. The cyclotron beam will

Operating frequency [MHz]	2998
Input energy [MeV]	62
Maximum output energy [MeV]	200
Aperture radius [mm]	4
Number of accelerating cells per tank	13
Number of tanks per module	4
Number of modules	9
Total number of tanks	36
Number of power klystrons	9
Number of Permanent Quadrupole Magnets	36
Quadrupole gradient [T/m]	160
Total length [m]	13.32
Synchronous phase angle [degree]	19
Peak RF Power [MW]	32.8
RF duty cycle [%]	0.2
Beam duty cycle [%]	0.18
Repetition rate [Hz]	400
Transverse acceptance [mm mrad]	11.8π
Trapped cyclotron beam [%]	9.6

TABLE 2.1. Main electromagnetic and beam parameters of LIBO.

be matched transversely to LIBO by focusing element placed between the two accelerator and the aperture radius of 4 mm will make the transverse acceptance such as to contain the cyclotron beam emittance, which is 12π mm mrad.

The situation is different about the longitudinal dynamic [23]. Only part of the low frequency cyclotron beam falls into the short LIBO buckets and many particles remain outside. This effect has been analyzed by simulating the cyclotron beam, which appears continuous in phase when referred to the LIBO frequency of 2998 MHz, and dividing it into many thin phase slices which span 360 degrees. Each slice is followed through the linac with a beam dynamics program, and LIBO is optimized in a preliminary way, assuming no misalignments. It is then found that about the 50% of the continuous beam can be transmitted and that about 25% of the transmitted beam is fully accelerated.

Misalignments of Permanent Magnet Quadrupoles and linac tanks, and other errors such as quadrupole gradient errors, can reduce the intensity of the accelerated beam. One can estimate the effect of quadrupole misalignments on the transmission by making a Monte Carlo optics calculation. Four types of error have been analyzed: quadrupole displacement errors of ± 0.1 mm; tank displacement errors of ± 0.1 mm; quadrupole rotation errors of $\pm 1^\circ$; and quadrupole strength errors of $\pm 1\%$. The only error that produces any significant

reduction in the transmission is quadrupole displacement. For a displacement error tolerance of 0.1 mm there is a 90% probability that the transmission will be greater than 10%.

4.2. Mechanical Aspects. All LIBO modules are essentially identical, except for their progressive increase in length, corresponding to the increasing velocity of the protons. There are three basic elements that compose the accelerating structure in each module: the *half-cell-plate*, the bridge coupler and the end cell. Each module contains 102 half-cell-plates, 3 bridge couplers and 2 end cells. The half-cell-plate is the basic building block of a tank. It is a rectangular plate containing half of an accelerating and, at the reverse side, half of a coupling cell. Apart from the slight difference in length, the shape of the cells remains the same in all the modules. All accelerating cells in a tank have the same length; the length of the coupling cells as well as the shape of the coupling slots between the accelerating and coupling cells do not vary over the whole module.

The bridge couplers and end cells (see figure 2.11) have stainless steel flanges and cylindrical inserts brazed into them to fix the module on the girder, thus minimizing stress and deformation in the soft copper. Connections to the beam line at both ends of the module and the pumping ports to the vacuum manifold are also in stainless steel.

In each bridge coupler and in the end cells are housed PMQs for beam focussing, pick-up loops for RF field measurements, and movable tuners for frequency corrections after the whole module has been brazed. The finished and brazed copper structure is mounted on a rigid girder, onto which an external reference is fixed for alignment purposes.

All copper pieces for LIBO have been machined on numerically-controlled lathe and milling machines. The manufacturing precision of the structure must take into account RF, brazing and alignment specifications. Typical tolerance values are ± 10 to 20 mm with 0.4 mm roughness for RF surfaces and 0.8 mm for brazed surfaces. The half-cell-plates are made of laminated OFE copper. Pre-machining, followed by a 250° C stress relieving in air was used to obtain the 20 mm-planarity for vacuum brazing after the final machining. Bridge couplers and end cells are of forged OFE copper, while for flanges, manifolds and fixing points, forged 316 LN stainless steel is used. For the brazing of the end cells, bridges and half-cell-plates, where the surfaces to be brazed must be in horizontal position, several grooves are machined in the bottom surfaces of the pieces, while the upper surfaces are perfectly flat, see figure 2.13. The positions and dimensions of these grooves, determining the quantity of the brazing alloy, have been tested on sample pieces with an automatic total-immersion ultrasonic testing method. All of the half-cell-plates are machined with the external surfaces as reference, and then these surfaces are used for the alignment during

the brazing of a tank. These surfaces are machined with sharp angles in order to avoid any flow of the brazing alloy into the RF cavities. The complete module is obtained by the brazing of 17 sub-assemblies, already individually brazed at higher temperature. For the different brazing steps, commercially available silver-base alloys are used, with decreasing brazing temperatures ranging from 850° C to 750° C. All brazing operations are performed in all-metal vacuum furnaces.

The cooling of the LIBO module is provided by water flowing through channels inside specially designed copper plates. Two of these are brazed to either side of each tank, giving eight parallel circuits per module with a total water flux of 200 l/min. A transfer forced convection coefficient of 14000 W/(m² °C) for each circuit assures the cooling of the LIBO tank at full power of 2.3 kW (corresponding to a repetition rate of 400 Hz and an RF pulse length of 5 ms). The results of a 3-D finite elements code simulation with lateral cooling can be summarized as follows:

- The maximum temperature gradient between the nose of the accelerating cell and the lateral sides of the tank is just below 7 °C.
- Thermal expansion of the nose region is about 10 mm and the frequency change due to temperature (detuning sensitivity) is about 60 kHz/°C. Frequency tuning during operation will be done by regulating the water flow in each tank.

Frequency tuning during operation will be done by regulating the water flow in each tank.

CHAPTER 3

Design Techniques for a Side Coupled Linac

This chapter deals with the techniques used to design the resonant cavities and the other electromagnetic apparatus of a Side Coupled Linac, the emphasis being on the particular case of LIBO.

A linear accelerator is composed by several systems, as shown in figure 3.1, namely a particle source (or an injection system of the beam coming from another accelerator), the resonant accelerating cavities and the magnets for the focusing of the beam, the power klystron or the radiofrequency power system, the vacuum pumps and the cooling system.

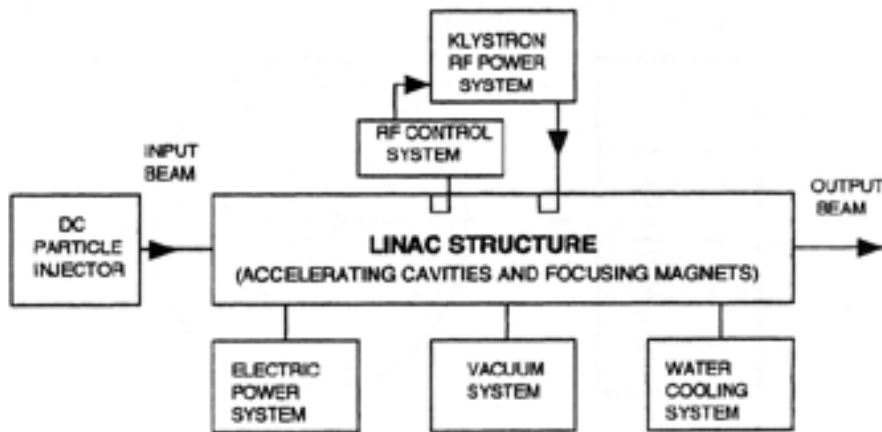


FIGURE 3.1. Schematic view of a Linac.

The design of the so-called *radiofrequency* apparatus and of the *electromagnetic* aspects of a Side Coupled Linac is not an automatic procedure yet; the most part of the design is still a *cut and paste* procedure where the experimental verification, namely the RF measurement, plays the fundamental role.

By using a *top-down* approach, the design of such a structure can be seen through different levels of detail, as shown in figure 3.2.

First, the accelerator is thought as a black box, where the particles beam goes through. For this case, the parameters of interest are numerical values, namely the entry and the output energy and velocity of particles, the desired maximum length of the chain of cavities, the transit time factor, the peak electric field and the feeding frequency.

All these numbers define the first characteristics of the chain, and one can say that this is a 0-dimensional design.

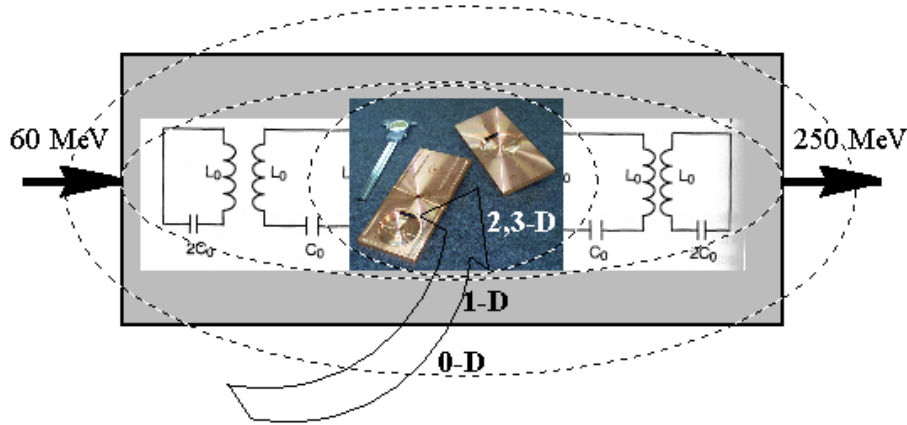


FIGURE 3.2. The design of a Linac with a top-down methodology. The arrow follows the logic steps from the first properties of the accelerator to the definitions of all the details on the single cavities.

Then, it is necessary that the subdivision in cavities be made, the number of which gives the electric field gradient for each cavity. The cavities are coupled together either electrically or magnetically and the coupling coefficients characterize this coupling. At this point, it is possible to build up an equivalent model where each single-mode resonant cavity is represented by a lumped equivalent circuit. With the help of this circuit, the behavior of the whole chain can be studied, including the effect of machining tolerances in the cavities parameters and their effects on the chain behavior. This second step is a 1-dimensional design because one can move through the chain along the longitudinal direction.

Last, one has to design the single cavity shape taking into account the properties requested by the whole chain, that are the designed shunt impedance, quality factor, resonant frequency and coupling factor among cavities. This step is not trivial because the translation of those properties in electromagnetic properties of the cavities needs attention, since they cannot be fixed one at a time. Also the possibility of slightly change in frequency by using movable tuners has to be included. This is the final step and it is a 2-dimensional design, when one designs the single cavity, and therefore moves along the orthogonal plane to the longitudinal direction, and it is 3-dimensional design when the slot is open and one considers two or more cavities, and therefore moves also along the longitudinal direction.

The following sections respect this view, and so first we calculate the main parameters, as the acceleration gradient, involved with the whole

structure; then we continue with the analysis of a cavities chain, coming to the properties of the single cavities and the last sections are devoted to their design. Particular emphasis is on the design of the coupling mechanism for the feeding of the structure through a waveguide in the last section. It is apparent that the various steps have a reciprocal feedback and are not completely close each other, but in any case they give a way to follow.

Finally, it is worth noting that we lead with a procedure that was not completely followed during the design of first LIBO module, because of problem of time and of feasibility of proposed solutions. This is normal because we remember that the first LIBO module was a *proof of principle* and then it was thought *golden plated*. In this sense, we hope that the procedure presented will be a first attempt to have a methodology easy to transfer to an industrial construction of these type of structure instead.

1. Global Parameters of the Accelerator

An accelerator for hadrontherapy needs low production costs and not large overall dimensions of the structure. Both points are necessary for a feasible installation in medical centers and hospitals. The second point can be satisfied if the cavity are small in dimensions and stacked as much as possible. Furthermore, if these cavities let easily flow the power, it is possible to use a single alimentation for a large amount of cavities. In reality, the type, the entry energy, and the velocity of particles suggest the type of the structure with a good efficiency to use. In our case, protons and 60 MeV beam entry energy suggest exactly a multi-cell coupled structure.

The choice of the frequency and of the total length of a normal-conducting structure comes applying the Kilpatrick criterion [16, 26, 27] which states the maximum value for the electric field in each cavity before breakdowns and sparking occur. The Kilpatrick results were expressed in a convenient formula given as

$$f = 1.64E_K^2 e^{-8.5/E_K}, \quad (3.1)$$

where f is the frequency in MHz and E_K is in MV/m and it is said the *Kilpatrick limit*. The behaviour of formula (3.1) is shown in figure 3.3. The Kilpatrick criterion is based on experimental results, and nowadays it is considered conservative; the formula is still used, except that the actual peak surface field is expressed as $E_S = bE_K$, where b is known as the *bravery factor* and it is chosen in a range from 1.0 to 2.0.

Let us enter now in the details of the first LIBO module; the large availability of low cost power klystrons at 3 GHz could be a good reason to choose that frequency. The correspondent Kilpatrick limit is around 47 MV/m. After that, one has to consider:

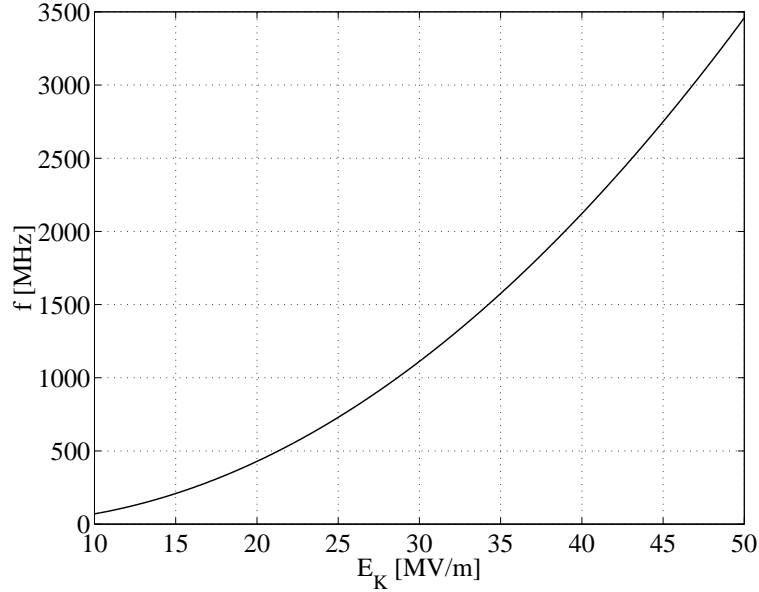


FIGURE 3.3. The behavior of Kilpatrick formula 3.1.

- For the first LIBO module the bravery factor is $b = 1.1$, which is a conservative value.
- The maximum electric field is not the accelerating one, the shunt impedance concept gives the effective accelerating field, which is lower.
- The input and output energy for the first LIBO module are 60 MeV and 70 MeV respectively. Then, a boost of 10 MeV is necessary.
- Of course, not all the path is accelerating for the particles: a coefficient expresses the ratio accelerating gaps to total length. It is a mean value and takes into account the variation of dimensions along the structure for the synchronism with the accelerated particles.
- The transit time factor has to be considered, using formula (2.6). Note that for this parameter it should be better to have short accelerating gaps, but in this case the length of the structure is not well used, because the ratio gaps to cell period becomes smaller. Therefore, there is a *trade-off* that should be considered.
- The first module should be as short as possible (1.3m long).

Finally, in this step of design the global parameters for each cavities are fixed, as the feeding frequency, the necessary shunt impedance in order to obtain the desired acceleration gradient, and the subdivision of the accelerator in modules, and then, in cavities.

2. Analysis of Coupled Cavities

In this section we deal with the study of the properties of a resonant cavities chain. From the previous step one obtains the frequency of feeding¹, that has to be the resonant frequency of the whole chain and the shunt impedance for the accelerating cavities. The quality factor of the cavities can be assigned from the used material and the foreseen roughness of surfaces; of course after the design of cavities, a feedback is necessary to control the results with the real values.

In this step, the value of the coupling coefficient between cavities could be chosen. This parameter has a fundamental role since it determines the separation between resonant modes of the chain and the power flow through the chain. The undesirable coupling coefficient between non-adjacent accelerating cavities and between non-adjacent coupling cavities has to be considered too. Its value could be supposed known and stated to percent fractions and obtained later during the single cavities design.

The aim of the analysis is to verify the correct behavior of the axial electric field, which is the accelerating field, taking into account the machining tolerance. The latter is represented through errors in the cavities parameters.

It is apparent that for this analysis it is sufficient a lumped single mode resonant circuit to describe each cavity, rather than a detailed 3-D description of each cavity. Different approaches are thinkable: one can simulate the chain of equivalent circuits with an electric network simulator, and we follow this way in the next section, by using Spice, or one can use a semi-analytical approach, by means of matrices representations, and study the effects of tolerances using the perturbations theory, and we follow this second way in the next chapter.

2.1. Equivalent circuit for resonant coupled cavities. Let us start from the bricks of which are made the equivalent model we want to present. A microwave cavity resonating at a certain frequency can be represented using an equivalent lumped circuit [12] with a resistance, an inductance and a capacitance. Each of them represent an effect: the inductance represents the magnetic energy stored in the cavity volume, the capacitance represents the strong electric field effect around the typical noses for non-relativistic particles and the resistance represents the ohmic losses on the cavity walls.

The R, L and C parameters are also related with the resonant frequency, the quality factor expressed by the formula (2.3) and with the shunt impedance expressed by the formula (2.4). The relations are the

¹Thanks to the power generator, namely the klystron, it is usually a narrow band of frequencies, rather than a single tone.

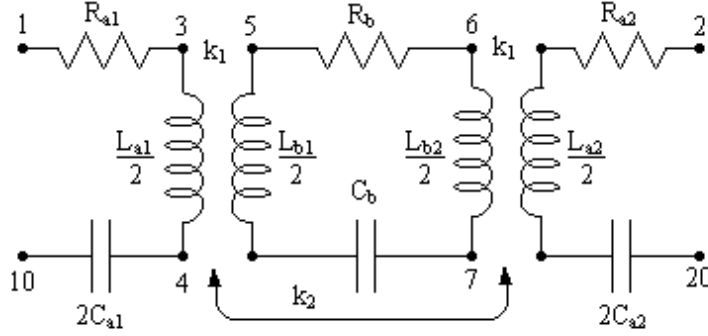


FIGURE 3.4. The equivalent circuit for two half cavities coupled through a cavity with different parameters (coupling cell).

following

$$\omega_0 = \frac{1}{\sqrt{LC}}, \quad Q = \frac{\omega_0 L}{R}, \quad R_{sh} = \omega_0 L Q = \frac{(\omega_0 L)^2}{R} \quad (3.2)$$

In the case of magnetically coupled cavities, one can introduce a coupling coefficient between the inductances.

2.2. Spice analysis. In this section we explain the behavior of a chain of lumped circuits using the electric circuits simulator Spice².

The accent is placed on the behavior of the chain of RLC circuits. In the following we consider, as basic unit, the circuit shown in figure 3.4 which represents three coupled resonant cavities: two half cells and one whole cavity of a different type. We can recognize in the half cells the accelerating ones and in the whole cavity, the coupling cavity of a biperiodic structure. Moreover, we consider only the coupling between adjacent cavities, which is the strongest, and the coupling between non-adjacent accelerating cavities. Finally, we neglect the coupling between non-adjacent coupling cavities because, due to the geometry of the side coupled linacs, those cells are placed on opposite sides and the coupling vanishes. It is worth noting that the non-adjacent couplings are considered as a disturb, since they change and complicate the behavior of the chain.

²Spice was born in the University of California in the early '70, the name is the acronym of *Simulation Program with an Integrated Circuits Emphasis*, and of course, it was thought to be used with integrated circuit with thousands of components. Apart from the others merits, it had a broadly diffusion because it was completely freeware. Nowadays several private software companies distribute commercial versions of Spice, and almost all are used to distribute also an evaluation version with some limitations on the number of components that the simulation allows. This fact has implied a broad diffusion of Spice language, which is nowadays considered a *standard*. Other information on the use of this program can be found in [28].

Spice has the relevant possibility to include the scheme of figure 3.4 in a sub-circuit that can be reproduced as a *black-box* connected only through external nodes. Let us start from the study of a chain composed by 13 coupled cells. In this case we deal with 7 accelerating cavities and 6 coupling cavities. Each cavity resonates at 3 GHz and there is a coupling between adjacent cavities equal to 0.04, the chain is terminated on short-circuited half cells, which are accelerating ones. The Q value for all the cavities is 8000. On the left side there is also the alimentation which is a simply voltage generator. Note that it is important the position of the alimentation along the chain. In fact, one could think to put the alimentation in the middle of the chain, but in that case, due to the behavior of the modes, not all the modes are excited and should be recognizable. For example, thinking to the $\pi/2$ mode, the coupling cells are nominally uncharged for that mode. The alimentation in the first or in the last cell of the chain assures that all the modes are excited, instead.

In figure 3.5 it is shown the frequency spectrum of a periodic structure without second neighbour coupling. The $\pi/2$ mode is at 3 GHz. Due to the finite Q value, note that near 0 and π modes there is a mode mixing: if the structure is excited at those frequencies, two or more modes could be excited. In this sense, we could appreciate the $\pi/2$ mode behavior that have the longest distance to the adjacent resonant modes. In figure 3.6, the current in a coupling cell in a logarithmic scale is also shown: in the $\pi/2$ mode the coupling cells are nominally uncharged.

In figure 3.7 the case with finite second neighbour coupling is shown. The chain is periodic again and this leads to a distortion in the distribution of modes. The $\pi/2$ mode is no more located at 3 GHz. We know from resonant circuit theory [17, 18] that it is necessary that a biperiodic chain be considered, the frequency of coupling cells being

$$f_b = \frac{f_0}{\sqrt{1 - k_2}},$$

where f_0 is the frequency of the accelerating cavities and also the desired $\pi/2$ mode frequency and k_2 is the second neighbour coupling between accelerating cavities. In figure 3.8 the result is shown.

Finally, the powerful of a spice analysis is that one could deal with an almost real model of the structure and simulate in a short time the whole chain, up to all the 102 cells of a module. The disadvantage is that it is not an approach that gives general properties but only empirical rules.

3. Single cavity design

As already explained in the previous introduction, the design of the single cavities of a Linac aims to the definitions of all the geometrical

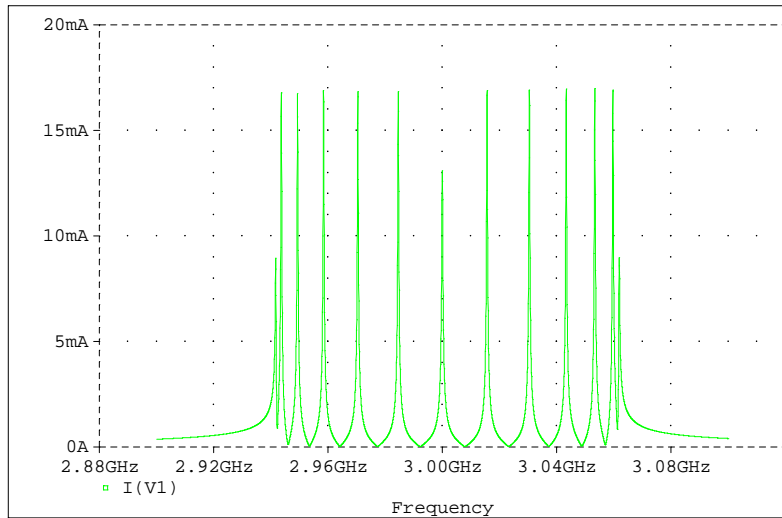


FIGURE 3.5. Spice simulation for a periodic chain without next nearest neighbor coupling.

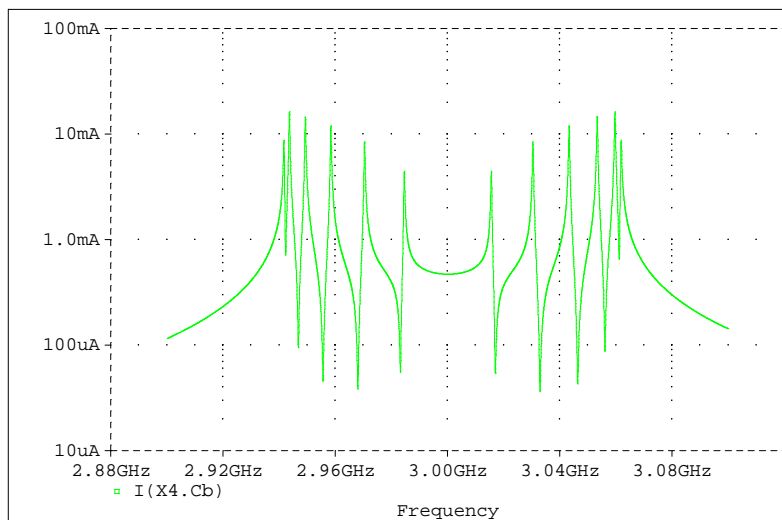


FIGURE 3.6. Spice simulation for a periodic chain without next nearest neighbor coupling. The coupling cavities are nominally uncharged.

dimensions and mechanical details and uses the parameters, as resonant frequency and coupling factor, defined in the previous steps of design.

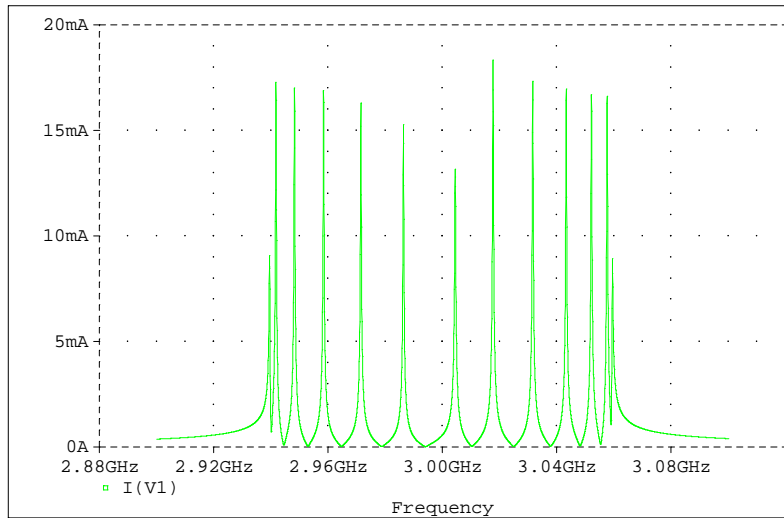


FIGURE 3.7. Spice simulation for a periodic chain with next nearest neighbor coupling.

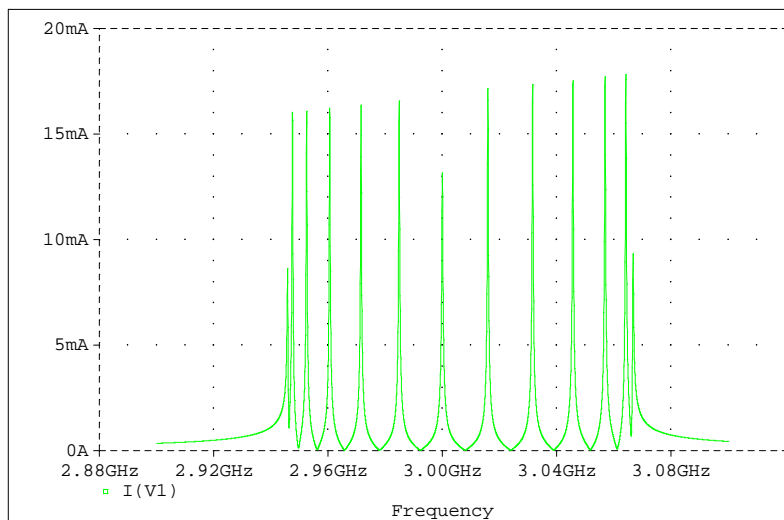


FIGURE 3.8. Spice simulation for a biperiodic chain with next nearest neighbor coupling.

It is worth noting that the passage from the previous step to this one is not trivial, since the relation between the lumped parameters and the electromagnetic properties of the cavity is not expressed through

a closed formula, while the viceversa is. In other words, given a resistance, inductance and capacitance of a lumped resonant circuit, the geometry of the related cavity is not uniquely determined.

The shape of cavities of multi-cell coupled structure is almost fixed: the longitudinal dimensions are related to the particles velocity in order to have synchronism, and one tries to have them as small as possible in order to stack as much cavities as possible. Moreover, the shapes are rounded to reduce the wall currents path and then to maximize the quality factor. Useful advises and procedure to design cavities shape can be found in [12, 16]. An hard point in the design could be the definition of the tuners shape and position, because one wants then with a large range of intervention, but with a linear behavior and these two requirements are normally in contrast.

In this section, after a short introduction to numerical computer codes that are necessary for the design of a general-shape cavity, we deal with the specific example of the single cavities design for LIBO project.

3.1. Numeric codes. The numeric computer codes are used in the design of cavities for linear accelerators because the analytical calculations can be used only with simple geometries, as the so called pill-box, which are not useful for real applications.

These numerical programs are used to optimize the shape of the cavity, given overall dimensions, in order to get the best values for the requested resonant frequency, field pattern and quality factor. Most known and used computer programs for such a calculations are:

- *Superfish*³ is a frequency domain 2-dimensional (2D) simulator which uses a finite elements algorithm. From the practical point of view, after the preparation of a file with the geometry of the structure, one can obtain the resonant frequency for every resonant mode of the cavity, the quality factor and the shunt impedance and other useful parameters. The program has lots of internal macro dedicated to the calculations of parameters useful in the accelerator cavities design as the power dissipated on each *wall* of the cavity. Other useful results given are the resonant frequency variations for a unit displacement of all the walls of which the cavity is composed.
- *MAFIA*⁴ (MAxwell's equations using a Finite Integration Algorithm) is a 3-dimensional code either in the time and the frequency domain. It has a CAD-like interface and it is a powerful general purpose simulator. The later versions have also the relevant possibility of calculation with small losses in the walls.

³See also the site www.lanl.gov for more information.

⁴See also the site www.cst.de for more information.

- *HFSS*⁵ (High Frequency Structure Simulator) is a recent product from ANSOFT and is a 3D structure electromagnetic field simulator. Thanks to the CAD-like approach, it offers an intuitive interface to simplify design entry, a field solving engine with accuracy-driven adaptive solutions based on a finite element method (FEM), and a post-processor for post-elaborations of the calculated fields. The software has also an optimization tool.

With the help of Superfish it is possible to design the shape of a single cavity, supposed to have a rotational symmetry. The goal could be the optimization of the shunt impedance and quality factor, once the correct resonant frequency is obtained. Also it is important that one controls the sensitivity of the resonant frequency with respect to machining errors for all the cavity dimensions. This study helps to understand where the machining tolerance has to be more stringent.

On the other hand, with the help of MAFIA or HFSS, one can design the coupling slots between cavities which usually break the rotational symmetry. The goal is to reach the correct coupling factor, keeping the resonant frequency unchanged. This last point is reached after slightly changes of one or more geometrical dimensions of the cavity.

3.2. The design of accelerating and coupling cavities of LIBO. In this subsection we explain the specific design of LIBO cavities. As explained in the previous subsection 13 accelerating cavities and 12 coupling cavities compose a LIBO tank. The 25 cavities are distributed on 26 tiles. Each tile contains one half accelerating cavity and one coupling cavity, the geometries of which are rotationally symmetric. The two half cavities are coupled through a slot which is, first, generated by the intersection of geometries and then machined to enlarge the aperture. The slot breaks the 2-D symmetry of the half cavities.

First, the dimensions and shape of the accelerating cells (ACs) and coupling cells (CCs) have been evaluated using Superfish to fix the shunt impedance, the quality factor and, in a preliminary way, the resonant frequency. Then, MAFIA code was used to start the design of the coupling slot and to bring back the resonant frequency to the design value⁶. The coupling value of the foreseen slot was obtained from MAFIA in a preliminary way, but radiofrequency measurement on a cell prototype was preferred to control the result because it was judged more reliably in this case.

⁵See also the site www.ansoft.com for more information.

⁶It is worth noting that the presence of the slot changes both the frequencies of the cavities involved.

The design of these cells has been conceived to minimize the number of changing of the geometrical parameters in order to simplify their mechanical construction. The CCs and the slots do not present changes in dimensions along a module. The ACs have little changes in dimensions in order to be adapted to the increasing velocity of the particle along the modules. These changes are made tank by tank: all the ACs, and then all the tiles, are perfectly equal in a tank.

With this design the accelerating structure presents the same average electric field on axis in all the ACs and a decreasing coupling coefficient between adjacent cavities. These characteristics fully satisfy the beam dynamic requirements.

In the conceiving of the cavities, it was preferred having as more tuning instruments as possible, and in this sense the cavities had machinable rings placed in the inductive zone that were used before the brazing of each tank to bring the frequencies to an opportune mean value. This procedure is explained in the radiofrequency measurement chapter. After the brazing of a tank, it was possible to use two inductive tuners that are copper rods of few millimeters diameter for each cavity. The frequency ranges of these tuners were about 2.5 MHz for the ACs and 3.5 MHz for the CCs. In figure 3.9 the two sides of a tile with the cavities and both systems of tuning are shown.

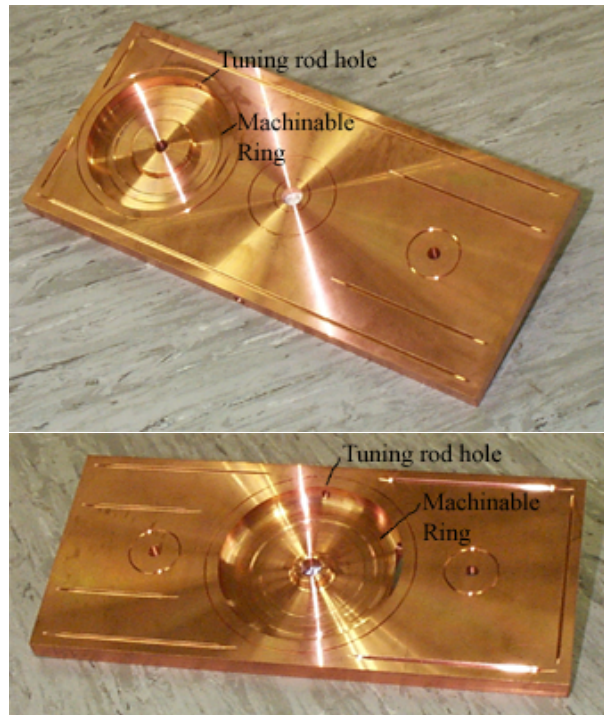


FIGURE 3.9. Particulars of the machinable ring and of the tuning rod hole for the coupling cavities (top) and for the accelerating cavities (down).

4. Bridge Couplers design

The bridge coupler has a fundamental role in a Side Coupled Linac. It allows to have tanks which are separated by magnetic quadrupoles and fed by the same RF waveguide. In the figure 3.10 a sketch of this functionality is shown.

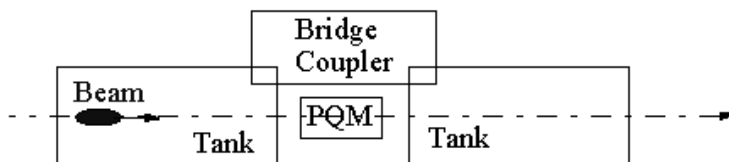


FIGURE 3.10. Schematic view of the Bridge Coupler functionality. The Bridge Coupler cavity couple two tanks and leaves the space for a Permanent Quadrupole Magnet by which the particles beam is focused.

Of course, the Bridge Couplers are particular cells, the design of which should be conceived paying attention to different claims with respect to the accelerating and coupling cavities.

Not so many Bridge Couplers have been realized in the accelerators community. The few examples are the ones for the 800 MHz Side Coupled Linac in the Los Alamos National Laboratory [19], and the 800 MHz Side Coupled Linac in the FermiLab in Chicago. For these linacs, the bridge couplers was connected to coupling cells, therefore, from the electromagnetic point of view they were analogous to accelerating cells.

In this case, one could think to a single cavity bridge coupler which directly connects two accelerating cells but mode mixing could arise⁷. The resonant mode we choose has to be far away from the others to avoid mode mixing.

In a LIBO module there are three Bridge Couplers. One is connected with the feeding waveguide through an iris (see figure 3.11), and the other two have pumping ports for the vacuum. In order to reduce the overall dimensions, it has been chosen a bridge coupler including also two coupling cells, which, of course, are specially designed.

The principal quality of such a structure is the transit time of energy which is equal to the length of the bridge coupler divided by the group velocity of the cavity mode. As the bridge coupler length is determined by other considerations, the principal figure of merit for a particular bridge coupler candidate is its group velocity, the higher the better [29].

⁷Due to a finite quality factor of the resonant cavities, more than one mode could be excited from a frequency tone and this phenomenon is called *Mode mixing*.

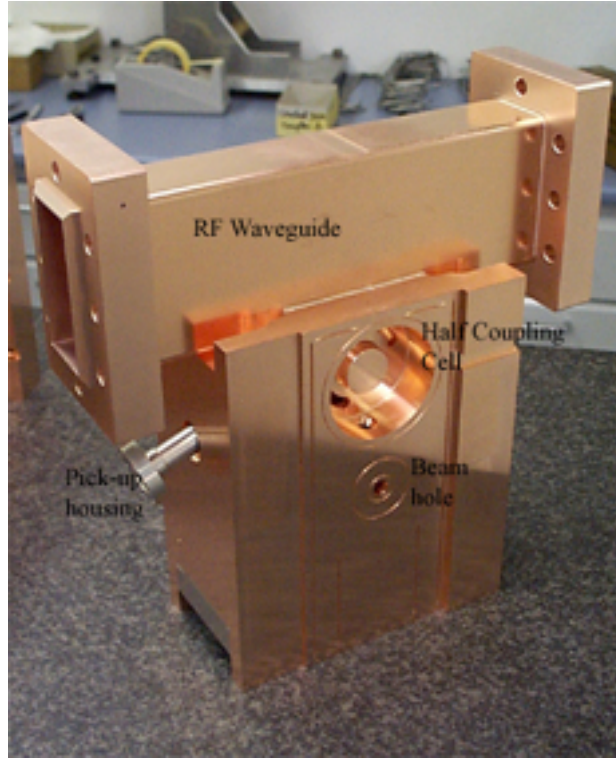


FIGURE 3.11. The LIBO Bridge Coupler with the feeding waveguide. It is also shown the half part of the coupling cell in the bridge coupler with the *banana* slots, Finally note the steel body for pick-up housing.

The longitudinal lengths are fixed by the beam dynamics in order to get the correct accelerating field when the particles enter in the next tank. The length of each BC is normally constrained to be odd multiples of the average cell length $\beta\lambda/2$ where β is the particle velocity and λ is the wavelength of RF Power. Therefore, in non relativistic linacs, where the particles velocities increase with energy, every bridge coupler has a different length. Strict application of this constraint would imply that every bridge coupler would also have different dimensions. These differences would imply also increased costs of fabrication.

Another constrain is about the level of the field in the central cavity of the bridge coupler: it should be as low as possible to decrease the dissipated power on the cavity walls.

4.1. Computer code design hints. The definition of a three cells bridge coupler with cavities coupled through magnetic *banana* slots was made through the following steps

- Definition of the geometry of the cavities with Superfish.
- Opening of slots using MAFIA. Correction of the frequency changing the noses lengths.

- Since the coupling factor does not strictly depend on the resonant frequency of cavities, one can start studying the definition of the correct coupling factor changing the dimensions (radii, length and position) of slots.
- After this operation, one can operate again on the nose lengths to readjust the resonant frequency to the correct value.

We chose also movable inductive tuners in the bridge couplers cells with a big range of correction in order to prevent the error of simulation of MAFIA code which is about 10 MHz for our structure⁸. For the simulations, the tuners was considered in their middle position in order to have positive and negative change of frequency. The range of these tuners was established by calculation of the beginning of a capacitive effect (decrease of frequency).

5. Coupling between Waveguide and Bridge Coupler

In this section, we show a method which uses MAFIA and some other tools to determine the correct coupling between the waveguide and the bridge coupler in the LIBO module.

Correct coupling means that the feeding waveguide is matched to its characteristic impedance Z_0 , and therefore there is no power reflected back to the klystron.

The figure of merit to quantify this concept is the *coupling factor* β , which is the cavity impedance, normalized to Z_0 that the waveguide sees through the coupling mechanism, namely the iris.

Then, $\beta = 1$ means *perfect matching*, $\beta > 1$ means that the module is *overcoupled*, and finally, $\beta < 1$ means that the module is *undercoupled*.

The goal is to translate the condition of perfect matching in the better dimensions of the iris, and of course the perfect matching is unfeasible; in this case it would be better to be slightly overcoupled.

The idea of this method is to use MAFIA to measure the electric reactance of the cavity seen by the waveguide through the iris in the fundamental mode TE_{10} in a similar way as *bridges* are used for measurement: the unknown is given from a balance of reactances.

The parameters to choose are the iris dimensions (width, length and depth) and the length of a short-circuited waveguide (see figure 3.11).

Note that the cavity is magnetically coupled to the waveguide, since the iris is located on the *short* side of the waveguide section. The fundamental mode TE_{10} has the maximum of the longitudinal component of the magnetic field there. Therefore, it is better to put a short-circuited

⁸This error in the computation was estimated comparing the RF measurement made in the microwave laboratory of INFN Sez. di Napoli with the results of the same structure simulated with MAFIA.

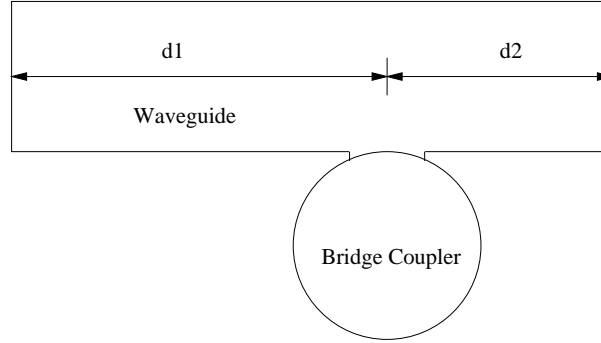


FIGURE 3.12. Coupling between the waveguide and Bridge Coupler. The structure simulated with MAFIA having two waveguides and one cavity.

waveguide whose length is about $\lambda/4$, in order to make the reflected wave having a constructive interference with the incoming wave.

With the help of MAFIA one can simulate the structure shown in figure 3.12: a single cavity coupled, through the iris, to a short-circuited waveguide, whose lengths are d_1 and d_2 from the iris center (*standing wave* structure). Such a structure gives a resonant frequency which has no relation with the one of the bridge coupler connected with an open, or extremely long waveguide, because that situation has a *travelling wave* character, namely there is no standing field in the waveguide. In our case we are simulating a closed structure, the resonant frequency of which depends on the waveguide lengths d_1 and d_2 .

But, using reasonable dimensions⁹, the waveguides work in the fundamental mode TE_{10} and they see the cavity through the iris as a purely reactance, and then it is possible to represent the structure by using the equivalent circuit shown in figure 3.13, that is composed by two transmission lines whose characteristic impedance is the one of the mode TE_{10} and, of course, the lengths are equal to the ones of the waveguides, and finally, the reactance is unknown.

The resonant condition of the circuit in figure 3.13 implies the following relation

$$X_i = -\frac{X_1 X_2}{X_1 + X_2}$$

where $X_{1,2} = Z_o \tan(\beta d_{1,2})$ (here β is the TE_{10} waveguide propagation constant). If one varies the electric length of one waveguide, using opportune steps, one obtains the behaviour of the reactance X_i . For example, the figure 3.14 shows the reactance of a copper Bridge Coupler model made in Naples in the mechanical workshop of INFN. It is worth noting that this reactance has a behaviour that is a characteristic of the iris dimensions and of the bridge coupler cavity and does not depend

⁹The waveguide lengths d_1 and d_2 have to be longer than two wavelengths, at least.

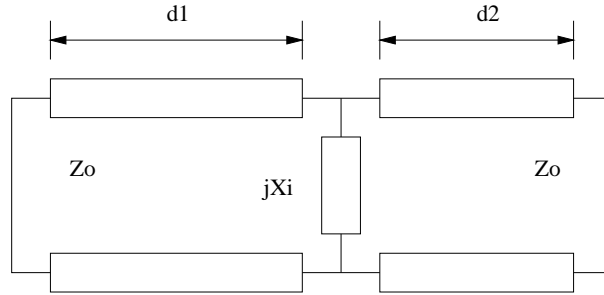


FIGURE 3.13. The equivalent circuit of the structure simulated with MAFIA. Two transmission lines and a purely reactance.

on the waveguides lengths. These waveguide lengths are only a tool we use to *explore* the behaviour.

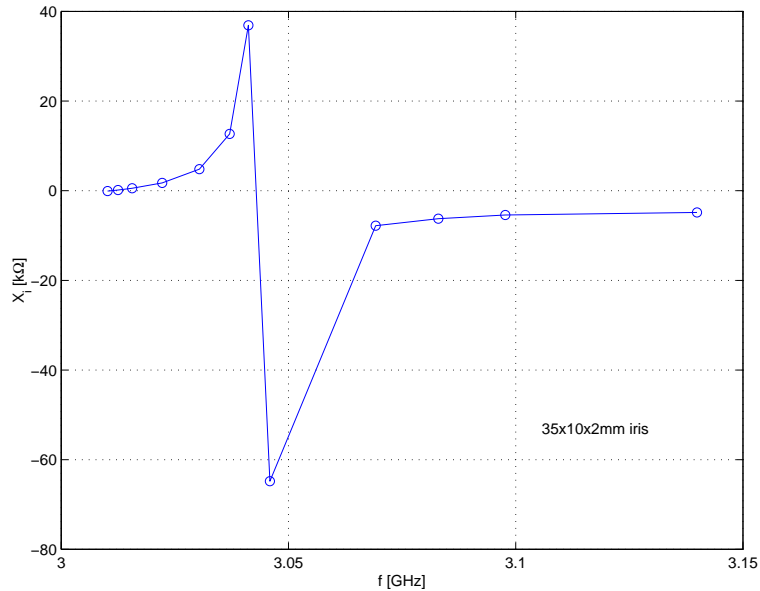


FIGURE 3.14. An example of reactance coming from MAFIA. The iris has dimensions $35 \times 10 \times 2$ mm (model made in Naples).

In figure 3.14 the reactance crosses the frequency axes, i.e. has zero value, after it has a resonant behaviour and asymptotically goes to zero for frequencies approaching infinity. The behaviour is always of this type, in spite of different irises and bridge coupler cavity dimensions.

Such a behaviour is well fitted by the equivalent circuit shown in figure 3.15 on the left: the parallel elements give the resonant behaviour and at high frequency the reactance is mainly due to the capacitance C_1 . The correct values for these elements can be found by a least square fitting. But, more important is the interpretation of the lumped

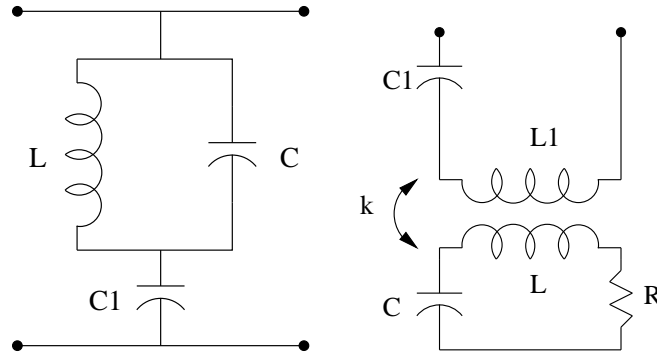


FIGURE 3.15. The equivalent circuit of the reactance X_i of the coupling mechanism (left) and a possible equivalent circuit from the cavity point of view (right).

elements of this circuit: indeed, it is clear that the resonant behaviour is due to the cavity (the resonant frequency of the Bridge Coupler), whereas the capacitance $C1$ represents the effect of the iris seen by the waveguide. It could seem uncorrect that a magnetic coupling is represented through a capacitance, but one has to think that the iris is about a quarter of wavelength long and this is sufficient to change the behaviour seen through a parallel element.

In order to find sufficient elements to fit the equivalent circuit, one has to compute points about the zero crossing (for the reactance), about the resonance (it is a zero crossing for the susceptance) and a point at a very high frequency (which means very short waveguides). In practical cases, not more than twelve points are needed.

The next point is how to go from the equivalent circuit of a cavity to the circuit we have just introduced. Figure 3.15 on the right shows a guess. The lower part of the circuit represents the bridge coupler, the transformer represents the magnetic coupling existing between cavity and waveguide (we know that, due to the position of the iris, only the magnetic fields are involved in the coupling process). Finally, the capacitance $C1$ plays the same role as in figure 3.15 left. Note that we introduced another inductance $L1$ and the mutual coupling k . If one tries to fit this circuit to the previous one, as shown in figure 3.16, one finds that

- $L1$ must be equal to L
- k is equal to 1
- R is connected in series with C

Finally, with the help of a computer code (Matlab, Mathcad, etc.), one has to find the frequency at which the real part of this equivalent circuit is equal to the characteristic impedance of the waveguide¹⁰.

¹⁰Remember that also the characteristic impedance of the waveguide weakly depends on the frequency.

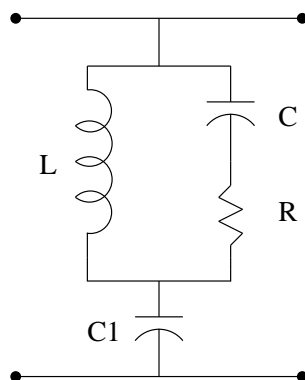


FIGURE 3.16. The final equivalent circuit for a cavity seen from the waveguide through the iris.

Here is a first disadvantage: if the resonant frequency of the simulated structure is different from the working frequency, the procedure with MAFIA should be repeated until the correct frequency and matching are reached. Once one has the correct frequency and, of course, the right dimension for the iris, one can calculate the right dimension d_2 for the short-circuited waveguide that makes the reactance null.

The latter point can be satisfied if one defines $Z_i = R_i + jX_i$ as the impedance of the circuit in figure 3.16, then

$$Y_i = \frac{R_i}{R_i^2 + X_i^2} - j \frac{X_i}{R_i^2 + X_i^2};$$

next, one finds the frequency satisfying

$$\frac{R_i^2 + X_i^2}{R_i} = Z_0$$

and last, gets the value for d_2

$$d_2 = \frac{1}{\beta} \arctan \left(-\frac{R_i^2 + X_i^2}{X_i Z_0} \right) \quad (3.3)$$

It is worth noting that from this procedure a perfect matching frequency is always given, but it could happen that the correspondent frequency is not the designed $\pi/2$ mode frequency. Note that the value of d_2 given from the formula (3.3) is always negative, but it is sufficient to sum to it one half of waveguide wavelength.

5.1. The procedure for the whole module. With a 3D numerical code as MAFIA it is impossible to simulate the whole module with more than one hundred cavities. It is necessary to introduce some equivalences in order to use the simulation with a single cavity. We substitute the equivalent lumped circuit for one cavity with a circuit which represents the whole module considering only the cavities charged with electromagnetic energy ($N = 52$ accelerating cells plus $N = 3$ bridge

coupler central cells). We have to consider that the $\pi/2$ mode operation for the module implies that

- of course, the frequency operation for the whole structure is the same for every cell;
- the quality factor of the whole structure can be assumed equal to the one of a single cavity;
- the total stored energy is about N times the energy stored in one cell.

In order to respect these conditions, the lumped elements of the equivalent circuit become:

- $R_N = R/N$
- $L_N = L/N$
- $C_N = NC$

Of course, in the LIBO structure there are two different types of charged cells (accelerating cavities and bridge coupler central cells): it would be possible to make a weighted mean of the parameters.

In the following we report possible steps for the procedure

- *Calculation with MAFIA.* Twelve points around the zero crossing, the resonance and the asymptotic value are necessary to fully individuate the reactance curve, then evaluate initial guess for the least square fitting giving the values for L,C and C1.
- *Calculation with Superfish* and/or RF measurement in order to characterize a cavity with an equivalent lumped circuit, one needs at least three global parameters that can be: the resonant frequency f_0 , the quality factor Q and the ratio of shunt impedance and quality factor r over Q . You can use a combination of Superfish calculation and RF measurement to get the correct values.
- *Calculation with Matlab.* In the equivalent circuit of figure 3.16, we can use the R, L and C parameter coming from the previous step and use C1 coming from MAFIA analysis. In this case the behaviour of the cavity plus the iris is well reproduced. In order to study the correct coupling for the whole module, we apply the rule we have established in the previous subsection.

Finally, for example, we show in more details the results obtained with an iris with dimensions $41 \times 10 \times 2$ mm. Figure 3.17 shows the reactance obtained with MAFIA and Superfish simulations. The fitting values are $L_{MAFIA} = 3.941nH$, $C_{MAFIA} = 0.7230pF$, $C1_{MAFIA} = 0.02366pF$. Using $f_0 = 2998MHz$, $Q = 8000$ and $RsQ = 90$ as cavity parameters, we get $L_{SF} = 4.778nH$, $C_{SF} = 0.5899pF$, $R_{SF} = 11.25m\Omega$. The research of the correct frequency gives

$$f_{\beta=1} = 2997MHz, \quad d2 + \lambda_g/2 = 42.45mm (0.3\lambda_g)$$

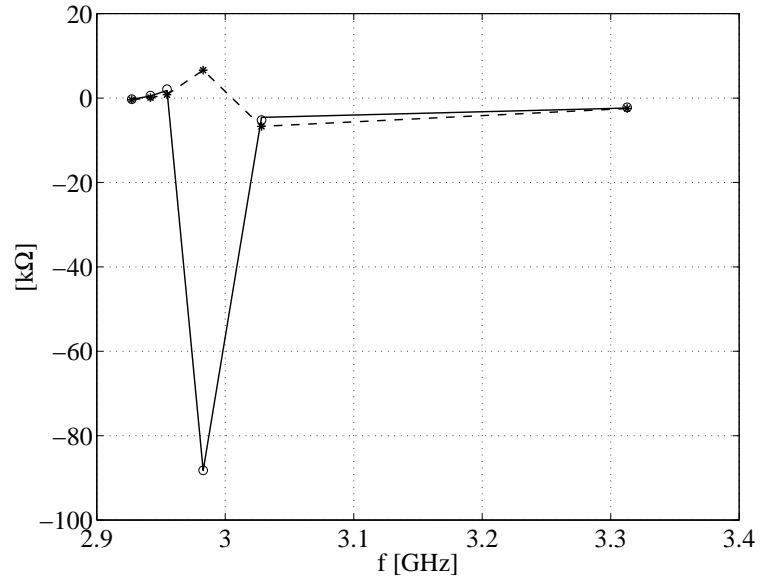


FIGURE 3.17. The Reactance of a $41 \times 10 \times 2$ mm iris. The dashed line interpolates the circles that are Superfish points. The continuous line interpolates points from Mafia.

In figure 3.18 are shown the dependencies of reflection coefficient on the short-circuit length and on the capacitance C_1 that is related with the iris dimensions. These plots are important to understand the sensitivity of the iris design, and it is apparent that the matching is very sensitive.

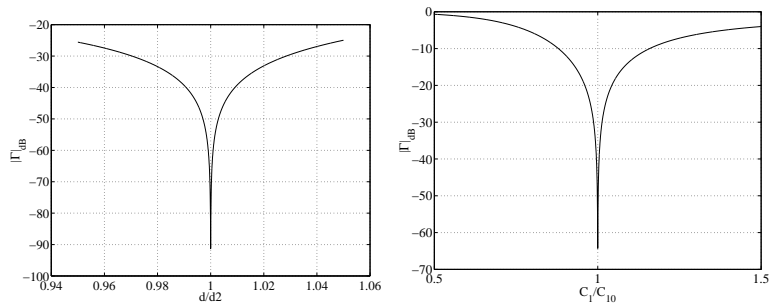


FIGURE 3.18. Dependence of Γ on d_2 (left). Dependence of Γ on C_1 (right).

CHAPTER 4

Circuit Model

In this chapter we analyze the equivalent circuit model of a chain of cavities magnetically coupled by using a transmission matrix approach. This latter allows an easy representation of the whole chain and easily introduces to the perturbation technique, as well. As explained in the previous chapter, the aim is to study the effect of the single cavities errors on the resonant frequency and on the flatness of the axial electric field of the whole structure, paying particular attention to the $\pi/2$ mode, which is the one of the Side Coupled structures. This situation well represents the effect of the machining tolerances on the single cavities resonant frequencies. We believe that a semi-analytical approach is useful to better understand the behaviour of such a structure. At a first moment, it could seem more useful a full numerical analysis by means of a circuit simulator, as Spice; but in this case, only empirical rules should be obtainable, where our approach could give general properties.

We have to say that, for the sake of simplicity, we consider only the coupling between adjacent cavities and we neglect the secondary coupling between non-adjacent cavities. Nevertheless, the approach seems to be promising even in this simplifying hypothesis.

1. Transmission matrix representation

Let us remember the definition of the transmission matrix [33] for the generic two-ports shown in figure 4.1.

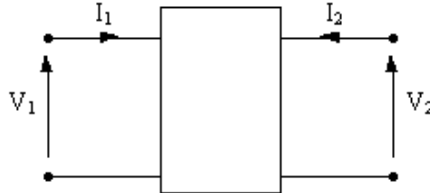


FIGURE 4.1. A generic two-ports network.

The input and the output can be connected via the transmission matrix representation

$$\begin{pmatrix} V_1 \\ I_1 \end{pmatrix} = \begin{pmatrix} t_{11} & t_{12} \\ t_{21} & t_{22} \end{pmatrix} \cdot \begin{pmatrix} V_2 \\ I_2 \end{pmatrix}$$

where the matrix elements are defined as follows

$$t_{11} = \left. \frac{V_1}{V_2} \right|_{I_2=0}, \quad t_{12} = \left. \frac{V_1}{I_2} \right|_{V_2=0},$$

$$t_{21} = \left. \frac{I_1}{V_2} \right|_{I_2=0}, \quad t_{22} = \left. \frac{I_1}{I_2} \right|_{V_2=0}.$$

The great advantage of such a representation is that a chain of dispositives is simply represented by the product of the respective transmission matrices, while others representation, such as resistances and conductances matrices, do not allow this operation.

1.1. Transmission Matrix for a single cavity. As stated in the previous chapter, a resonant cavity mode can be represented by the behavior of an equivalent lumped circuit. In this paragraph we deduce the transmission matrix of such a circuit. It should be better that the transmission matrix represent two half cavities magnetically coupled; this fact simplifies very much the building of the model, because it well represents the tiles composing a LIBO tank, and therefore, in the following, we call this circuit *cell*. In other words, a cell represents a tile with two half cavities magnetically coupled.

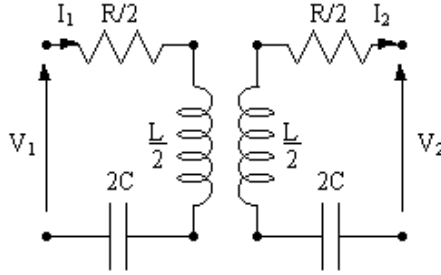


FIGURE 4.2. The equivalent circuit for a single cell representing two magnetically coupled half cavities.

Let us start from the calculation of the parameter t_{11} ; from the figure 4.2 it is easy to write

$$V_1' = j\omega \frac{L}{2} I_1 - j\omega M I_2, \quad V_2' = j\omega M I_1 - j\omega \frac{L}{2} I_2$$

$$V_1 = \left(\frac{R}{2} + \frac{1}{j\omega 2C} + j\omega \frac{L}{2} \right) I_1 - j\omega M I_2,$$

where V_1' and V_2' are the voltages on the inductances. When $I_2 = 0$ it is valid that

$$V_2 = V_2' = j\omega M I_1 \rightarrow I_1 = \frac{V_2}{j\omega M},$$

and then

$$V_1 = \left(\frac{R}{2} + j\omega \frac{L}{2} + \frac{1}{j\omega 2C} \right) \frac{1}{j\omega M} V_2$$

and, finally, the term t_{11} is

$$\begin{aligned} t_{11} &= \left[\frac{R}{2} + j\omega \frac{L}{2} \left(1 - \frac{1}{\omega^2 LC} \right) \right] \frac{1}{j\omega M} \\ &= \frac{1}{K} \left(\frac{\omega_0}{j\omega Q} + 1 - \frac{\omega_0^2}{\omega^2} \right). \end{aligned} \quad (4.1)$$

Note that $\omega_0 = \frac{1}{\sqrt{LC}}$ is the resonant frequency of an half cavity, and of a cell as well, Q is the quality factor, $Q = \frac{\omega_0 L}{R}$ and we use the relation $K = 2M/L$, leading to

$$t_{11} = \frac{1}{k} \left(\frac{\omega_0}{j\omega Q} + 1 - \frac{\omega_0^2}{\omega^2} \right), \quad (4.2)$$

Then, let us approach to the term t_{12} :

$$V_2' = j\omega M I_1 - j\omega \frac{L}{2} I_2 = \left(\frac{R}{2} + \frac{1}{j\omega 2C} \right) I_2$$

and

$$I_1 = \frac{I_2}{j\omega M} \left[\frac{R}{2} + \frac{1}{j\omega 2C} + j\omega \frac{L}{2} \right]$$

and so

$$\begin{aligned} V_1 &= \left(\frac{R}{2} + \frac{1}{j\omega 2C} + j\omega \frac{L}{2} \right) I_1 - j\omega M I_2 \\ &= \left[\left(\frac{R}{2} + \frac{1}{j\omega 2C} + j\omega \frac{L}{2} \right)^2 \frac{1}{j\omega M} - j\omega M \right] I_2 \\ &= \left[\left(\frac{R}{2} + \frac{1}{j\omega 2C} + j\omega \frac{L}{2} \right)^2 \frac{1}{(j\omega M)^2} - 1 \right] j\omega M I_2 \end{aligned} \quad (4.3)$$

and by using the equation (4.2), one obtains

$$t_{12} = j\omega M (t_{11}^2 - 1). \quad (4.4)$$

Next, we approach to the term t_{21}

$$V_1 = \left(\frac{R}{2} + \frac{1}{j\omega 2C} + j\omega \frac{L}{2} \right) I_1,$$

and imposing again $I_2 = 0$, one obtains

$$V_2 = V_2' = j\omega M I_1 \rightarrow \frac{I_1}{V_2} = \frac{1}{j\omega M},$$

and finally

$$t_{21} = \frac{1}{j\omega M} \quad (4.5)$$

For the latest term of the matrix, it is valid that

$$V_2' = j\omega M I_1 - j\omega \frac{L}{2} I_2 = \left(\frac{R}{2} + \frac{1}{j\omega 2C} \right) I_2$$

$$I_1 = \left(\frac{R}{2} + \frac{1}{j\omega 2C} + j\omega \frac{L}{2} \right) \frac{I_2}{j\omega M} \rightarrow t_{22} = \left(\frac{R}{2} + \frac{1}{j\omega 2C} + j\omega \frac{L}{2} \right) \frac{1}{j\omega M}$$

and again

$$t_{22} = t_{11}. \quad (4.6)$$

Then we can write the whole transmission matrix

$$T = \begin{pmatrix} t_{11} & (t_{11}^2 - 1)j\omega M \\ \frac{1}{j\omega M} & t_{11} \end{pmatrix} \quad (4.7)$$

and it is apparent that the matrix determinant is unitary, as expected for a reciprocal system.

In order to represent a chain of cavities, in the following sections we use powers of the matrix T . In this sense a spectral decomposition of matrix T would be useful, being

$$T = U\Lambda U^{-1} \rightarrow T^N = U\Lambda^N U^{-1}, \quad (4.8)$$

where U is the eigenvectors matrix and Λ is the eigenvalues diagonal matrix, namely

$$\Lambda = \begin{pmatrix} \lambda_1 & 0 \\ 0 & \lambda_2 \end{pmatrix} \quad (4.9)$$

where λ_1 and λ_2 are solutions of the characteristic polynomial

$$\det(T - \Lambda I) = 0 \rightarrow \lambda_{1,2} = t_{11} \pm \sqrt{t_{11}^2 - 1} \quad (4.10)$$

and by introducing a new variable x , such that

$$t_{11} = \cosh x, \quad (4.11)$$

we obtain a rationalization of the expressions

$$\Lambda = \begin{pmatrix} \cosh x + \sinh x & 0 \\ 0 & \cosh x - \sinh x \end{pmatrix} \quad (4.12)$$

$$,U = \begin{pmatrix} j\omega M \sinh x & 1 \\ 1 & \frac{j}{\omega M \sinh x} \end{pmatrix} \quad (4.13)$$

$$,U^{-1} = \frac{1}{2} \begin{pmatrix} -\frac{j}{\omega M \sinh x} & 1 \\ 1 & -j\omega M \sinh x \end{pmatrix}. \quad (4.14)$$

1.2. Transmission Matrix for a chain of N cells. By using the expressions (4.12) to (4.14), it is possible to write

$$T^N = \begin{pmatrix} \frac{\lambda_1^N + \lambda_2^N}{2} & j\omega M \sinh x \left(\frac{\lambda_1^N - \lambda_2^N}{2} \right) \\ \frac{-j}{\omega M \sinh x} \frac{\lambda_1^N - \lambda_2^N}{2} & \frac{\lambda_1^N + \lambda_2^N}{2} \end{pmatrix} \quad (4.15)$$

but noting that $\lambda_1 = e^x$ and $\lambda_2 = e^{-x}$, it is easy to show that

$$\begin{aligned} \frac{\lambda_1^N + \lambda_2^N}{2} &= \cosh Nx \\ \frac{\lambda_1^N - \lambda_2^N}{2} &= \sinh Nx \end{aligned} \quad (4.16)$$

and, finally

$$T^N = \begin{pmatrix} \cosh Nx & j\omega M \sinh x \sinh Nx \\ \frac{-j \sinh Nx}{\omega M \sinh x} & \cosh Nx \end{pmatrix} \quad (4.17)$$

which is the transmission matrix of a chain of N cells (tiles) containing $N - 1$ full cavities and 2 half cavities at the ends.

1.3. Resonant frequencies. Let us start now using the transmission matrix representation, to calculate the relevant parameters of the whole chain. Of course, the resonant frequencies of such a structure depend on the particular way we terminate the two half cells. Usually, there are two possibilities: either to terminate the half cell with another special half cell in order to have a whole cavity, or to terminate the half cell with a conducting plane, which is an electric mirror.

In our model there are three possibilities instead: the third one consists in terminating the two half cells with open-circuits, which should be unfeasible magnetic mirrors.

In the following, we always consider the structure terminated on the electric mirrors, i.e. the short-circuits in our equivalent model. The implementation of such a condition can be to right-multiply the matrix T^N by the column vector $(0 \ 1)^T$. This operation implies that the voltage is zero and the current is unitary on the last half cell. The second one is an arbitrary position and enforces the amplitude of the signals travelling on the chain to obey to that unitary value. In other words, this position fixes the amplitude of voltages and currents along the chain (remember that in a resonant condition these should be fixed from the initial energy of the system).

The resonant conditions of the structure are represented by those values of the frequency making zero the impedance Z_{ing} seen from the

left side of the chain. This impedance is expressed by

$$Z_{ing} = \frac{(T^N)_{12}}{(T^N)_{22}} = \frac{j\omega M \sinh x \sinh Nx}{\cosh(Nx)}, \quad (4.18)$$

where with the notation $(A)_{ij}$ we indicate the element of place (i, j) in the matrix A . The denominator of the previous impedance (4.18) cannot be infinite, unless the frequency is infinite, while the numerator has $N + 1$ zeros.

Furthermore, in the following we make the hypothesis of infinite quality factor of the cavities, namely the resistances in the equivalent circuit are zero; the zeros of the function $\sinh x$ are enclosed in those of the function $\sinh Nx$. By imposing that $x = jx'$, we can write $\sinh Nx = j \sin Nx'$ and therefore the zeros are

$$x' = \frac{s\pi}{N} \quad \text{with } s = 0, 1, \dots, N \quad (4.19)$$

and the equation (4.2) and noting that $t_{11} = \cos x'$, it is easy to deduce the resonant frequencies

$$\omega = \frac{\omega_0}{\sqrt{1 - k \cos \frac{s\pi}{N}}}. \quad (4.20)$$

The quantity $\phi = \frac{s\pi}{N}$ can be seen as the phase advance of the fields along the chain at a certain frequency [12]. It is worth noting that all the resonant frequencies are enclosed within the interval

$$\omega \in \left[\frac{\omega_0}{\sqrt{1+k}}, \frac{\omega_0}{\sqrt{1-k}} \right] \quad (4.21)$$

where the extremes are the so called 0-mode and the π -mode and are characterized by a phase advance of 0 and π . Finally, it is apparent that the $\pi/2$ mode resonant frequency is present only if the number of cavities is odd, that is when N is even; and since we want to deal with a structure operating in the $\pi/2$ -mode, then in the following we always consider N as an even number¹.

1.4. The axial field. In this section we calculate the expression of the voltage on the capacitance of the generic cavity. This parameter is related to the accelerating voltage of the real cavity.

The voltage on the i -th capacitance is proportional to the current of the same index through the impedance $\frac{1}{j\omega C}$ for the generic cavity and through $\frac{1}{j2\omega C}$ for the half cavities terminating the chain. If we consider the last half cavity, we have

$$\begin{pmatrix} V_N \\ I_N \end{pmatrix} = T_N \begin{pmatrix} V_{N+1} \\ I_{N+1} \end{pmatrix}$$

¹It is worth noting that if one assumes an infinite quality factor, then the $\pi/2$ mode corresponds to $x = j\pi/2$, which means $\omega = \omega_0$ and $t_{11} = 0$.

and if it is short-circuited, then

$$\begin{pmatrix} V_N \\ I_N \end{pmatrix} = T_N \begin{pmatrix} 0 \\ 1 \end{pmatrix} = \begin{pmatrix} (T_N)_{12} \\ (T_N)_{22} \end{pmatrix}$$

and in an analogous way, for the other cavities, it is

$$\begin{aligned} \begin{pmatrix} V_{N-1} \\ I_{N-1} \end{pmatrix} &= T_{N-1} \begin{pmatrix} V_N \\ I_N \end{pmatrix} = T_{N-1} \cdot T_N \begin{pmatrix} 0 \\ 1 \end{pmatrix} = \begin{pmatrix} (T_{N-1} \cdot T_N)_{12} \\ (T_{N-1} \cdot T_N)_{22} \end{pmatrix} \\ \begin{pmatrix} V_{N-2} \\ I_{N-2} \end{pmatrix} &= T_{N-2} \cdot T_{N-1} \cdot T_N \begin{pmatrix} 0 \\ 1 \end{pmatrix} = \begin{pmatrix} (T_{N-2} \cdot T_{N-1} \cdot T_N)_{12} \\ (T_{N-2} \cdot T_{N-1} \cdot T_N)_{22} \end{pmatrix} \end{aligned} \quad (4.22)$$

Last, we can deduce the rule for the generic capacitance

$$V_{ci} \propto I_i = \left(\prod_{l=i}^N T_l \right)_{22} \quad \text{for } i = 1, 2, \dots, N \quad (4.23)$$

and, of course, $V_{cN+1} \propto 1$.

In the expression (4.23) we need the product of $N-i+1$ transmission matrix, but remembering the matrix (4.17), we can obtain in a similar way

$$\prod_{l=i}^N T_l = \begin{pmatrix} \cosh(N-i+1)x & j\omega M \sinh x \sinh(N-i+1)x \\ \frac{-j \sinh(N-i+1)x}{\omega M \sinh x} & \cosh(N-i+1)x \end{pmatrix} \quad (4.24)$$

and therefore

$$\begin{aligned} V_{ci} &\propto \cosh(N-i+1)x \quad \text{for } i = 1, 2, \dots, N \\ V_{cN+1} &\propto 1 \end{aligned} \quad (4.25)$$

1.5. Asymptotic expression of the ratio between the voltages on the capacitances of two adjacent cavities in an infinite structure. In this short subsection we consider an interesting property of an infinite chain of cavities, that is given from the ratio of the voltages of two adjacent cavities. Let us start from the ratio

$$\frac{V_{ci}}{V_{ci+1}} = \frac{\cosh(N-i+1)x}{\cosh(N-i)x} \quad (4.26)$$

and imposing that $N-i+1 = i'$, one obtains

$$\begin{aligned} \frac{V_{ci}}{V_{ci+1}} &= \frac{\cosh i'x}{\cosh(i'-1)x} = \frac{\cosh i'x}{\cosh i'x \cosh x + \sinh i'x \sinh x} \\ &= \frac{1}{\cosh x + \sinh x \tanh i'x} \end{aligned} \quad (4.27)$$

and if $N \rightarrow \infty$, namely the chain is infinite, i' also goes to the infinity, $\tanh i'x = 1$ and therefore

$$\frac{V_{ci}}{V_{ci+1}} = \frac{1}{\cosh x + \sinh x} = \frac{1}{\lambda_1} = \lambda_2 \quad (4.28)$$

Therefore, we obtain that the ratio is equal to the eigenvalue λ_2 of the transmission matrix T . It is worth noting that this could be a way to obtain the dispersion diagram for an infinite chain and it is interesting that this concept is related to the eigenvalues of the transmission matrix.

2. The perturbed transmission matrix

This section deals with the case of a chain of equivalent circuits with different lumped parameters, i.e. the inductances and capacitances depend from the cavities.

This situation represents the realistic case of finite machining tolerance and errors for the copper tiles containing two coupled half cells. Such errors lead to a different resonant frequency and a different shunt impedance for each half cell and could be interesting to find a connection between the machining tolerances and the reachable relevant parameters of the whole chain that are the $\pi/2$ -mode resonant frequency and the axial field.

In the equivalent model these errors are schematized by a shift in the resonant frequency ω_0 becoming $\omega_0 + \delta\omega_{0i}$ for each cavity.

2.1. The perturbed transmission matrix for one cell. Let us consider the single two-ports shown in figure 4.3, which is composed by two half cavities and where i is the two-ports index.

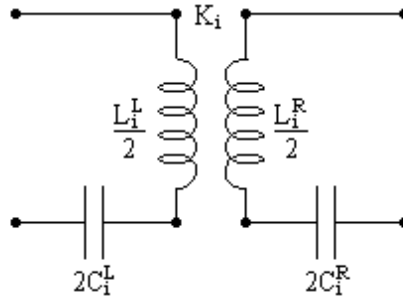


FIGURE 4.3. The two-ports representing two coupled half cavities with different parameters.

The machining tolerances are represented by errors in the cavity inductance and capacitance which are different for the left and right

sides of the two-ports. In this case, the transmission matrix becomes

$$T_i = \begin{pmatrix} t_{11i}^L & (t_{11i}^L t_{11i}^R - 1)j\omega M \\ \frac{1}{j\omega M} & t_{11i}^R \end{pmatrix} \quad (4.29)$$

where we have defined

$$\begin{aligned} t_{11i}^L &= \frac{1}{K_i} \left[1 - \left(\frac{\omega_{0i}^L}{\omega} \right)^2 \right] \sqrt{\frac{L_i^L}{L_i^R}} \cong \frac{1}{K_i} \left[1 - \left(\frac{\omega_{0i}^L}{\omega} \right)^2 \right] \\ t_{11i}^R &= \frac{1}{K_i} \left[1 - \left(\frac{\omega_{0i}^R}{\omega} \right)^2 \right] \sqrt{\frac{L_i^R}{L_i^L}} \cong \frac{1}{K_i} \left[1 - \left(\frac{\omega_{0i}^R}{\omega} \right)^2 \right] \end{aligned} \quad (4.30)$$

Therefore, starting from the scheme of figure 4.3 we introduce the following notation

$$\begin{aligned} C_i^L &= 2C + \delta C_i^L \\ L_i^L &= \frac{L}{2} + \delta L_i^L \\ C_i^R &= 2C + \delta C_i^R \\ L_i^R &= \frac{L}{2} + \delta L_i^R \end{aligned} \quad (4.31)$$

where the apexes L and R indicate respectively the left and the right side half cell parameters. If ω_{0i}^L and ω_{0i}^R are the resonant frequencies then

$$\begin{aligned} \omega_{0i}^L &= \omega_0 + \delta\omega_{0i}^L = \frac{1}{\sqrt{L_i^L C_i^L}} \\ \omega_{0i}^R &= \omega_0 + \delta\omega_{0i}^R = \frac{1}{\sqrt{L_i^R C_i^R}} \end{aligned} \quad (4.32)$$

Let us find now the frequencies perturbations $\delta\omega_{0i}^L$ e $\delta\omega_{0i}^R$. The perturbation on the resonant frequency can be related to the inductance and capacitance in the following way

$$\omega_0 = \frac{1}{\sqrt{LC}} \rightarrow \frac{\delta\omega_0}{\omega_0} = -\frac{1}{2} \left(\frac{\delta L}{L} + \frac{\delta C}{C} \right), \quad (4.33)$$

then the perturbations for both sides are

$$\begin{aligned} \frac{\delta\omega_{0i}^L}{\omega_0} &= -\frac{1}{2} \left(\frac{\delta L_i^L}{L_i^L} + \frac{\delta C_i^L}{C_i^L} \right) \\ \frac{\delta\omega_{0i}^R}{\omega_0} &= -\frac{1}{2} \left(\frac{\delta L_i^R}{L_i^R} + \frac{\delta C_i^R}{C_i^R} \right) \end{aligned} \quad (4.34)$$

The terms in parenthesis can be assumed of the same order of magnitude, because they are consequence of the same machining tolerances.

Under this hypothesis, we can write

$$\begin{aligned}\frac{\delta\omega_{0i}^L}{\omega_0} &= -\frac{\delta C_i^L}{C_i^L} \\ \frac{\delta\omega_{0i}^R}{\omega_0} &= -\frac{\delta C_i^R}{C_i^R}.\end{aligned}\quad (4.35)$$

And considering that

$$\begin{aligned}\omega_{0i}^L &= \omega_{0i}^R - \delta\omega_{0i}^R + \delta\omega_{0i}^L \\ \omega_{0i}^R &= \omega_{0i}^L - \delta\omega_{0i}^L + \delta\omega_{0i}^R\end{aligned}\quad (4.36)$$

and after a substitution in the t_{11} expression (4.2), one obtains

$$\begin{aligned}t_{11i}^L &= \frac{1}{K_i} \left[1 - \frac{\omega_{0i}^L \omega_{0i}^R + \omega_{0i}^L (\delta\omega_{0i}^L - \delta\omega_{0i}^R)}{\omega^2} \right] \cong \\ &\cong \frac{1}{K_i} \left[1 - \frac{\omega_0^2}{\omega^2} - 2 \frac{\delta\omega_{0i}^L}{\omega_0} \right] = \dot{t}_{11i} + \varepsilon_i^L \\ t_{11i}^R &= \frac{1}{K_i} \left[1 - \frac{\omega_{0i}^R \omega_{0i}^L + \omega_{0i}^R (\delta\omega_{0i}^R - \delta\omega_{0i}^L)}{\omega^2} \right] \cong \\ &\cong \frac{1}{K_i} \left[1 - \frac{\omega_0^2}{\omega^2} - 2 \frac{\delta\omega_{0i}^R}{\omega_0} \right] = \dot{t}_{11i} + \varepsilon_i^R\end{aligned}\quad (4.37)$$

where we introduce the new error parameters

$$\begin{aligned}\varepsilon_i^L &= -\frac{2}{K_i} \frac{\delta\omega_{0i}^L}{\omega_0} \\ \varepsilon_i^R &= -\frac{2}{K_i} \frac{\delta\omega_{0i}^R}{\omega_0}\end{aligned}\quad (4.38)$$

By neglecting the higher order terms, the matrix T becomes then

$$T_i = \dot{T}_i + \varepsilon_i^L \begin{pmatrix} 1 & j\omega M \dot{t}_{11} \\ 0 & 0 \end{pmatrix} + \varepsilon_i^R \begin{pmatrix} 0 & j\omega M \dot{t}_{11} \\ 0 & 1 \end{pmatrix}\quad (4.39)$$

where the variables with a dot on top indicate imperturbed quantities. The expression (4.39) can be rearranged as

$$T_i = \dot{T}_i + \frac{\varepsilon_i^L + \varepsilon_i^R}{2} \begin{pmatrix} 1 & j2\omega M \dot{t}_{11} \\ 0 & 1 \end{pmatrix} + \frac{\varepsilon_i^L - \varepsilon_i^R}{2} \begin{pmatrix} 1 & 0 \\ 0 & -1 \end{pmatrix}\quad (4.40)$$

and in a short way

$$T_i = \dot{T}_i + \varepsilon_i^+ P_i + \varepsilon_i^- Q_i\quad (4.41)$$

where we introduced

$$\varepsilon_i^+ = \frac{\varepsilon_i^L + \varepsilon_i^R}{2} \quad \varepsilon_i^- = \frac{\varepsilon_i^L - \varepsilon_i^R}{2}$$

and $P_i = I + B$, I being the identity matrix and if one defines $b = 2j\omega M$ then

$$B = \begin{pmatrix} 0 & b \\ 0 & 0 \end{pmatrix}, \quad Q_i = \begin{pmatrix} 1 & 0 \\ 0 & -1 \end{pmatrix} \quad (4.42)$$

2.2. The perturbed transmission matrix of the whole chain.

The behavior of the whole chain is represented by the product of the transmission matrix for each cell; in the case of errors, this product is not given from T^N because the T is different for each cell. It is given by the product of terms like $T + P_p + Q_p$ instead.

$$\begin{aligned} T_{tot} &= (\dot{T} + P_1 + Q_1)(\dot{T} + P_2 + Q_2) \dots (\dot{T} + P_N + Q_N) \\ &= \dot{T}^N + P_1 \underbrace{\dot{T} \dots \dot{T}}_{(N-1)\text{times}} + \dot{T} P_2 \underbrace{\dot{T} \dots \dot{T}}_{(N-2)\text{times}} + \dots + \underbrace{\dot{T} \dots \dot{T}}_{(N-2)\text{times}} P_{N-1} \dot{T} \\ &+ \underbrace{\dot{T} \dots \dot{T}}_{(N-1)\text{times}} P_N + Q_1 \underbrace{\dot{T} \dots \dot{T}}_{(N-1)\text{times}} + \dot{T} Q_2 \underbrace{\dot{T} \dots \dot{T}}_{(N-2)\text{times}} \\ &+ \dots + \underbrace{\dot{T} \dots \dot{T}}_{(N-2)\text{times}} Q_{N-1} \dot{T} + \underbrace{\dot{T} \dots \dot{T}}_{(N-1)\text{times}} Q_N + \text{high order terms} \end{aligned} \quad (4.43)$$

where we neglected the product of two or more perturbed matrices. Then, in a short form we can write

$$T_{tot} \cong \dot{T}^N + \sum_{p=1}^N \dot{T}^{p-1} P_p \dot{T}^{N-p} + \sum_{p=1}^N \dot{T}^{p-1} Q_p \dot{T}^{N-p}$$

The first term of the previous sum is

$$\begin{aligned} \dot{T}^{p-1} P_p \dot{T}^{N-p} &= U \Lambda^{p-1} U^{-1} P_p U \Lambda^{N-p} U^{-1} \\ &= \varepsilon_p^+ U \Lambda^{p-1} U^{-1} (I + B) U \Lambda^{N-p} U^{-1} = \\ &= \varepsilon_p^+ \dot{T}^{N-1} + \varepsilon_p^+ U \Lambda^{p-1} U^{-1} B U \Lambda^{N-p} U^{-1} \end{aligned} \quad (4.44)$$

and since T can be expressed as the product of a diagonal matrix by the eigenfunctions matrices, one obtains

$$\begin{aligned} T_{tot} &= \dot{T}^N + \dot{T}^{N-1} \sum_{p=1}^N \varepsilon_p^+ + \sum_{p=1}^N \varepsilon_p^+ U \Lambda^{p-1} U^{-1} B U \Lambda^{N-p} U^{-1} + \\ &+ \sum_{p=1}^N \varepsilon_p^- U \Lambda^{p-1} U^{-1} Q_p U \Lambda^{N-p} U^{-1} \end{aligned} \quad (4.45)$$

The expressions for the third and fourth terms of previous formula are obtained in a similar way. Then, the expression for the transmission

matrix of the whole chain is

$$T_{tot} = \dot{T}^N + \dot{T}^{N-1} \sum_{p=1}^N \varepsilon_p^+ + \frac{\cosh x}{\sinh x} \sum_{p=1}^N \varepsilon_p^+ [\heartsuit + \diamondsuit] + \sum_{p=1}^N \varepsilon_p^- \clubsuit \quad (4.46)$$

where the symbols represent the following matrices

$$\begin{aligned} \heartsuit &= \begin{pmatrix} \sinh(N-1)x & j\omega M \sinh x \cosh(N-1)x \\ \frac{\cosh(N-1)x}{j\omega M \sinh x} & \sinh(N-1)x \end{pmatrix} \\ \diamondsuit &= \begin{pmatrix} -\sinh(2p-N-1)x & j\omega M \sinh x \cosh(2p-N-1)x \\ \frac{-\cosh(2p-N-1)x}{j\omega M \sinh x} & \sinh(2p-N-1)x \end{pmatrix} \\ \clubsuit &= \begin{pmatrix} \cosh(N-2p+1)x & j\omega M \sinh x \sinh(N-2p+1)x \\ -\frac{\sinh(N-2p+1)x}{j\omega M \sinh x} & -\cosh(N-2p+1)x \end{pmatrix} \end{aligned}$$

It is apparent that the matrix (4.46) has an imperturbed term, a perturbed one not depending on the errors positions along the chain and two terms that depend instead.

3. The perturbed resonant frequency

The resonant frequencies of the whole chain can be obtained from the zeros of the element of place (1,2) in the transmission matrix, representing the chain impedance seen from one side when the opposite side is short-circuited.

We mainly refer to the $\pi/2$ mode and want to analyze the effect of the errors on the resonant frequency that goes from ω_0 to $\omega = \omega_0 + \Delta\omega$. We can represent this situation by a function: $\Delta\omega = F(\delta\omega_{01}, \delta\omega_{02}, \dots, \delta\omega_{0N})$. We obtain the expression for the element (1,2) from the formula (4.46) which is

$$\left(\prod_{i=1}^N T_i \right)_{12} = h(\omega, \delta\omega_{01}, \dots, \delta\omega_{0N}) = g(\omega_0 + \Delta\omega, \varepsilon_p^L, \varepsilon_p^R)$$

and then the resonant frequency can be seen as an implicit function $g(\omega_0 + \Delta\omega, \varepsilon_p^L, \varepsilon_p^R) = 0$, the solution of which is the perturbed frequency we are looking for. In that case we deal with

$$g(\omega_0 + \Delta\omega, \varepsilon_p^L, \varepsilon_p^R) = f(j\frac{\pi}{2} + \Delta x, \varepsilon_p^L, \varepsilon_p^R) = 0$$

It could be convenient to calculate Δx which is the error of x , rather than directly calculate $\Delta\omega$. Let us expand, up to the first order, the function f around the imperturbed value $\Delta x = 0$, namely $x = x_0 = j\frac{\pi}{2}$

and $\varepsilon_p^{L,R} = 0 \forall p$.

$$f \Big|_{\Delta x, \varepsilon_p=0} + \sum_{p=1}^N \varepsilon_p^L \frac{\partial f}{\partial \varepsilon_p^L} \Big|_{\Delta x, \varepsilon_p^L=0} + \sum_{p=1}^N \varepsilon_p^R \frac{\partial f}{\partial \varepsilon_p^R} \Big|_{\Delta x, \varepsilon_p^R=0} + \Delta x \frac{\partial f}{\partial x} \Big|_{\Delta x, \varepsilon_p=0} = 0 \quad (4.47)$$

The first term represents the unperturbed part that is zero. Let us remember the expression of the element (1, 2) of T^N in the perturbed case

$$\begin{aligned} \left(\prod_{i=1}^N T_i \right)_{12} &= j\omega M \{ \sinh x \sinh Nx \\ &+ \sum_{p=1}^N \varepsilon_p^+ [\sinh x \sinh (N-1)x + \cosh x \cosh (N-1)x] \\ &+ \cosh x \sum_{p=1}^N \varepsilon_p^+ \cosh (2p - N - 1)x \\ &+ \sinh x \sum_{p=1}^N \varepsilon_p^- \sinh (N - 2p + 1)x \} \end{aligned} \quad (4.48)$$

If one deals with the derivative with respect to x of the previous expression, it is useless to consider more than the first term, because the others become zero when one substitutes $\varepsilon_p = 0 \forall p$. In the following, using $x = j\frac{\pi}{2} + \Delta x$, we can simplify

$$\begin{aligned} \sinh x &= j \cosh \Delta x \\ \sinh Nx &= \cos N\frac{\pi}{2} \sinh N\Delta x \end{aligned}$$

where we consider N as an even number, because we want to excite the $\pi/2$ mode. Then, it is valid that

$$f(\Delta x) = -\omega M \cos N\frac{\pi}{2} \cosh \Delta x \sinh N\Delta x,$$

and therefore

$$\frac{\partial f}{\partial x} \Big|_{x=j\pi/2} = -\omega MN \cos N\pi/2. \quad (4.49)$$

For the derivative with respect to $\varepsilon_p^{L,R}$, we have to consider all the terms, and by considering the following trigonometric identities

$$\begin{aligned}
\sinh(N-2p+1)x &= j(-1)^p \cos N \frac{\pi}{2} \cosh(N-2p+1)\Delta x \\
\cosh x &= j \sinh \Delta x \\
\sinh(N-1)x &= j \sin(N-1) \frac{\pi}{2} \cosh(N-1)\Delta x \\
\cosh Nx &= \cos N \frac{\pi}{2} \cosh N\Delta x \\
\cosh(N-1)x &= j \sin(N-1) \frac{\pi}{2} \sinh(N-1)\Delta x
\end{aligned} \tag{4.50}$$

the expression (4.48) becomes

$$\begin{aligned}
\left(\prod_{i=1}^N T_i \right)_{12} &= -\omega M \left\{ \cos N \frac{\pi}{2} \cosh \Delta x \sinh N\Delta x + j \sin(N-1) \frac{\pi}{2} \sum_{p=1}^N \varepsilon_p^+ \right. \\
&\quad \cdot [-\cosh \Delta x \cosh(N-1)\Delta x - \sinh \Delta x \sinh(N-1)\Delta x] \\
&\quad - \sum_{p=1}^N \varepsilon_p^+ \sinh \Delta x \cosh \left[(2p-N-1)(j \frac{\pi}{2} + \Delta x) \right] \\
&\quad \left. - j \sum_{p=1}^N \varepsilon_p^- \cosh \Delta x (-1)^p \cos N \frac{\pi}{2} \cosh(N-2p+1)\Delta x \right\} \\
&= f(\Delta x, \varepsilon_p^L, \varepsilon_p^R)
\end{aligned} \tag{4.51}$$

In the derivative with respect to $\varepsilon_p^{L,R}$, the only term different from zero comes from $i = p$. For example, the term in ε_p^L is

$$\begin{aligned}
\frac{\partial f}{\partial \varepsilon_p^L} &= -j \frac{\omega M}{2} \cdot \\
&\quad \left\{ \sin(N-1) \frac{\pi}{2} [\cosh \Delta x \cosh(N-1)\Delta x + \sinh \Delta x \sinh(N-1)\Delta x] \right. \\
&\quad - 2j \sinh \Delta x \cosh \left[(2p-N-1)(j \frac{\pi}{2} + \Delta x) \right] \\
&\quad \left. \cosh \Delta x (-1)^p \cos N \frac{\pi}{2} \cosh(N-2p+1)\Delta x \right\}
\end{aligned}$$

And finally, the resonance equation is

$$j\omega M \cos N \frac{\pi}{2} \left[\sum_{p=1}^N \varepsilon_p^+ + jN\Delta x + (-1)^p \sum_{p=1}^N \varepsilon_p^- \right] = 0$$

and therefore the unknown is

$$\Delta x = j \frac{1}{N} \sum_{p=1}^N \left[\frac{\varepsilon_p^L + \varepsilon_p^R}{2} + (-1)^p \frac{\varepsilon_p^R - \varepsilon_p^L}{2} \right] = j \frac{\sum_{p=1}^N \varepsilon_p^*}{N} \tag{4.52}$$

where we introduced the new error parameter

$$\varepsilon_p^* = \sum_{p=1}^N \left[\frac{\varepsilon_p^L + \varepsilon_p^R}{2} + (-1)^p \frac{\varepsilon_p^R - \varepsilon_p^L}{2} \right] \quad (4.53)$$

In order to evaluate the frequency error and remembering the equation (4.11), one obtains

$$\Delta\omega = \omega_0 \left(\frac{1}{\sqrt{1 - jK \sinh \Delta x}} - 1 \right) \cong -j\omega_0 \frac{K}{2} \sinh \Delta x \quad (4.54)$$

Since Δx is of the same order of magnitude of all the $\varepsilon_p^{L,R}$, it is acceptable the following approximation

$$\Delta\omega = -j\omega_0 \frac{K}{2} \sinh \left(j \frac{1}{N} \sum_{p=1}^N \varepsilon_p^* \right) \cong \frac{\omega_0 K}{2N} \sum_{p=1}^N \varepsilon_p^* \quad (4.55)$$

Note that the quantity ε_p^* is equal to ε_p^R for even p , and for odd p it is equal to ε_p^L . Then, $\Delta\omega$ is proportional to the following sum

$$\varepsilon_1^L + \varepsilon_2^R + \varepsilon_3^L + \varepsilon_4^R + \varepsilon_5^L + \dots \quad (4.56)$$

which is a sum over the odd cavities.

This is a general result since it states that the frequency error of the whole chain depends only on the errors in the accelerating cavities, which are the charged ones for the mode $\pi/2$ mode. It is worth noting that this result is obtained under the hypothesis of negligible non-adjacent cavities coupling, since in the other case the stop-band concept is involved and the errors in the coupling cavities become important. Furthermore, the expression (4.55) does not contain product of different cavity errors, as we arrested the expansion to the first order, namely we neglect the correlation among the errors. Finally, under the previous hypothesis, it is also clear that the frequency error is independent of the relative positions of the cavities and that the variance of the frequency error is N times the one of the variables $\varepsilon_p^{L,R}$.

4. The perturbed axial field

In the circuit model, the voltage on the capacitance of a generic cell is equal to the accelerating voltage. Then, except for the term $1/(j\omega 2C_i)$ ($1/(j\omega C_i)$ for the lateral half cells), we look for the current I_i which is

$$I_i = \left(\prod_{l=i}^N T_l \right)_{22}, \quad \text{for } i = 1, 2, \dots, N \quad (4.57)$$

Note that such an expression comes from the hypothesis $I_{N+1} = 1$ which means that the last half cell is short-circuited and we arbitrarily fixed the current to one. In the following, we always use this hypothesis, and $i = 1, 2, \dots, N$.

Remembering the expression of T^N with errors, in the calculations of the expression (4.57), we obtain a formula similar to the formula (4.43), but in this case the product is limited to the last $N - i + 1$ terms. And therefore, we have dealings with

$$\begin{aligned} \left(\prod_{l=i}^N T_l \right) &= (\dot{T} + P_i + Q_i)(\dot{T} + P_{i+1} + Q_{i+1}) \dots (\dot{T} + P_N + Q_N) \\ &\cong \dot{T}^{N-i+1} + \sum_{q=i}^N \dot{T}^{q-i} P_q \dot{T}^{N-q} + \sum_{q=i}^N \dot{T}^{q-i} Q_q \dot{T}^{N-q} \end{aligned} \quad (4.58)$$

and in a similar way, we obtain

$$\left(\prod_{l=i}^N T_l \right) = \dot{T}^{N-i+1} + \dot{T}^{N-i} \sum_{q=i}^N \varepsilon_q^+ + \frac{\cosh x}{\sinh x} \sum_{q=i}^N \varepsilon_q^+ [\heartsuit + \diamondsuit] + \sum_{q=i}^N \varepsilon_q^- \clubsuit \quad (4.59)$$

where the cards symbols represents the following matrices

$$\begin{aligned} \heartsuit &= \begin{pmatrix} \sinh(N-i)x & j\omega M \sinh x \cosh(N-i)x \\ \frac{\cosh(N-i)x}{j\omega M \sinh x} & \sinh(N-i)x \end{pmatrix} \\ \diamondsuit &= \begin{pmatrix} -\sinh(2q-N-i)x & j\omega M \sinh x \cosh(2q-N-i)x \\ \frac{-1}{j\omega M} \frac{\cosh(2q-N-i)x}{\sinh x} & \sinh(2q-N-i)x \end{pmatrix} \\ \clubsuit &= \begin{pmatrix} \cosh(N-2q+i)x & j\omega M \sinh x \sinh(N-2q+i)x \\ -\frac{\sinh(N-2q+i)x}{j\omega M \sinh x} & -\cosh(N-2q+i)x \end{pmatrix} \end{aligned}$$

and therefore it is

$$\begin{aligned} I_i(\varepsilon_p^L, \varepsilon_p^R) &= \\ &= \cosh(N-i+1)x + \left[\cosh(N-i)x + \frac{\sinh(N-i)x}{\tanh x} \right] \sum_{q=i}^N \varepsilon_q^+ \\ &\quad - \sum_{q=i}^N \left[\varepsilon_q^+ \frac{\sinh(N-2q+i)x}{\tanh x} + \varepsilon_q^- \cosh(N-2q+i)x \right] \end{aligned} \quad (4.60)$$

As stated in the previous section, the machining tolerances are represented by a displacement of the variable $x \rightarrow j\pi/2 + \Delta x$, where Δx is the one of the expression (4.52), namely $\sum_{p=1}^N \varepsilon_p^*/N$. After a substitution of the perturbed x in the previous expression and noting that we are interested in the odd cavities, which are the accelerating ones, one

obtains

$$\begin{aligned}
I_i(\varepsilon_p^L, \varepsilon_p^R) &= (-1)^{\frac{N-i+1}{2}} \left\{ \cos [(N-i+1)\Delta x] \right. \\
&+ [\sin [(N-i)\Delta x] - \tan(\Delta x) \cos [(N-i)\Delta x]] \sum_{q=i}^N \varepsilon_q^+ \\
&- \tan(\Delta x) \sum_{q=i}^N \varepsilon_q^+ (-1)^{(i-q)} \cos [(2q-N-i)\Delta x] \\
&\left. - \sum_{q=i}^N \varepsilon_q^- (-1)^{(i-q)} \sin [(2q-N-i)\Delta x] \right\}
\end{aligned} \tag{4.61}$$

By noting that ε_p is a small quantity, we can expand the trigonometric functions around zero, leading to the following expression of I_i

$$\begin{aligned}
I_i(\varepsilon_1, \dots, \varepsilon_N) &= (-1)^{\frac{N-i+1}{2}} \left\{ 1 - \frac{(N-i+1)^2}{N^2} \left(\sum_{p=1}^N \varepsilon_p^* \right)^2 + \right. \\
&+ \sum_{p=1}^N \varepsilon_p^* \sum_{q=i}^N \varepsilon_q^+ \left[\frac{N-i+1 - (-1)^{(i-q)}}{N} \right] \\
&\left. - \sum_{p=1}^N \varepsilon_p^* \sum_{q=i}^N \varepsilon_q^- \left(\frac{2q-N-i}{N} \right) \right\} \\
&\text{for } i = 2s + 1 \text{ with } s = 0, \dots, \frac{N}{2} - 1
\end{aligned} \tag{4.62}$$

and we note that the first is the unperturbed term, the second term is independent of the errors positions and the last two are dependent, like for the perturbed resonant frequency.

It is worth noting that the cells current is stationary respect to the perturbations, because it depends on the square of $\varepsilon_p^{L,R}$.

In the following the term $(-1)^{\frac{N-i+1}{2}}$ is considered equal to 1, because it represents the phase relation between accelerating cavities. In fact, at a certain time, the electric field $E(t)$ in two adjacent accelerating cavities has a phase difference equal to π , but we are interested to the field experienced from the particles and they see always a positive field, and therefore we consider $(-1)^{\frac{N-i+1}{2}} = 1$.

In order to obtain V_{ci} , it is sufficient to multiply the previous currents by the capacitive impedance of the cavities.

If we come back to the case without errors, the structure we consider is symmetric and terminated on two half cavities, and therefore in the equivalent model, the circuits $i = 1$ and $i = N + 1$ have a double capacitance and an half inductance. The field in the cavities can be represented through a bar-plot as in figure 4.4, where the height of

the bars is proportional to the amplitude of the field and all the bars are normalized to one. The graph is in a percent scale. Note that the coupling cavities, which are represented by the even bars, are nominally uncharged.

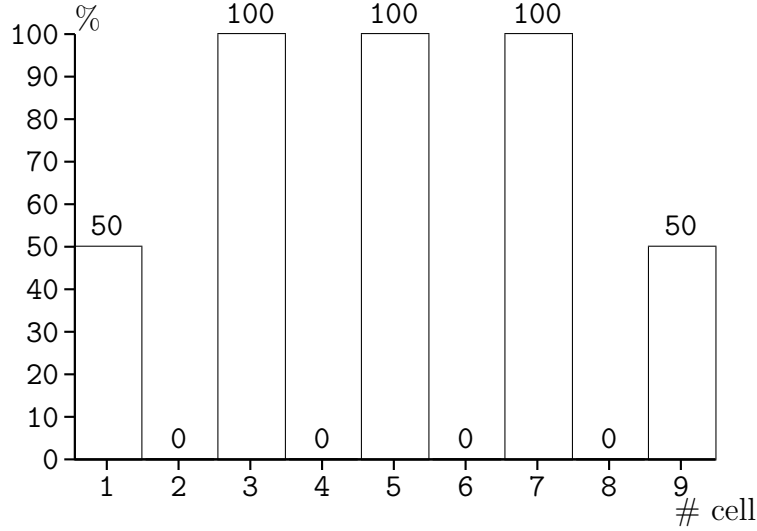


FIGURE 4.4. The relative level of field in the cavities in the unperturbed case.

Therefore, the lateral cavities produce an half voltage and we can drop this dissymmetry by considering only a contribution $i = 1$ which is the sum of the two half voltages. In such a way we do not directly consider the cavity $i = N + 1$ and we deal with $N/2$ accelerating cavities and index i goes from 1 to N . Then, the value of V_{ci} for the generic cavity is

$$\begin{aligned}
 V_{ci}(\varepsilon_1, \dots, \varepsilon_N) = & \frac{1}{j\omega C_{eqi}} \left\{ 1 - \frac{(N-i+1)^2}{N^2} \left(\sum_{p=1}^N \varepsilon_p^* \right)^2 + \right. \\
 & + \sum_{p=1}^N \varepsilon_p^* \sum_{q=i}^N \varepsilon_q^+ \left[\frac{N-i+1 - (-1)^{(i-q)}}{N} \right] \\
 & \left. - \sum_{p=1}^N \varepsilon_p^* \sum_{q=i}^N \varepsilon_q^- \left[\frac{2q-N-i}{N} \right] \right\}
 \end{aligned} \tag{4.63}$$

for $i = 2s + 1$ with $s = 1, 2, \dots, N/2 - 1$

where C_{eqi} is the capacitance of the cavity with number i and it is the series of the capacitances of the two half cavities with indexes $i - 1$ and

i.

$$\begin{aligned} \frac{1}{C_{eqi}} &= \frac{1}{C_{i-1}^R} + \frac{1}{C_i^L} \cong \frac{1}{C} \left[1 - \frac{1}{2} \left(\frac{\delta C_{i-1}^R}{2C} + \frac{\delta C_i^L}{2C} \right) \right] \\ &= \frac{1}{C} \left[1 - \frac{K}{2} \left(\frac{\varepsilon_{i-1}^R + \varepsilon_i^L}{2} \right) \right] \end{aligned} \quad (4.64)$$

After a substitution of expression (4.64) in the expression for V_{ci} , one obtains

$$\begin{aligned} V_{ci} &= \frac{1}{j\omega C} \left[1 - \frac{K}{2} \left(\frac{\varepsilon_{i-1}^R + \varepsilon_i^L}{2} \right) \right] \left\{ 1 - \frac{(N-i+1)^2}{N^2} \left(\sum_{p=1}^N \varepsilon_p^* \right)^2 \right. \\ &\quad \left. + \sum_{p=1}^N \varepsilon_p^* \sum_{q=i}^N \left[\varepsilon_q^+ \left(\frac{N-i+1 - (-1)^{(i-q)}}{N} \right) - \varepsilon_q^- \left(\frac{2q-N-i}{N} \right) \right] \right\} \end{aligned} \quad (4.65)$$

This formula needs further explication, it contains both square and linear terms in ε_p . A superficial analysis could drop the square terms, where a depth one should show that the coefficients of these terms are different in magnitude and their ratio is of the order of magnitude of σ_ε . Therefore, it is not allowed to drop the quadratic term.

For example, if the machining tolerances lead to a typical $\frac{\delta\omega_{0p}^{L,R}}{\omega_0} = \frac{K}{2}\varepsilon_p^{L,R}$ in the range $[10^{-3}, 10^{-4}]$ then, if $K = 0.04$, we have $\varepsilon_p^{L,R} \in [5 \cdot 10^{-2}, 5 \cdot 10^{-3}]$. The term ε_p^2 is in the range $[2.5 \cdot 10^{-3}, 2.5 \cdot 10^{-5}]$, and then it exists a range where the values of $\frac{K}{2}\varepsilon_p^{L,R}$ (namely the errors of the capacitances) and of ε_p^2 are similar. With these considerations the expression of V_{ci} becomes

$$\begin{aligned} V_{ci} &\cong \frac{1}{j\omega C} \left\{ 1 - \frac{(N-i+1)^2}{N^2} \cdot \left(\sum_{p=1}^N \varepsilon_p^* \right)^2 - \frac{K}{2} \left(\frac{\varepsilon_{i-1}^R + \varepsilon_i^L}{2} \right) \right. \\ &\quad \left. + \sum_{p=1}^N \varepsilon_p^* \sum_{q=i}^N \left[\varepsilon_q^+ \left(\frac{N-i+1 - (-1)^{(i-q)}}{N} \right) - \varepsilon_q^- \left(\frac{2q-N-i}{N} \right) \right] \right\} \end{aligned} \quad (4.66)$$

Concerning the expression of V_{c1} , we states that it is the sum of the first and last cells contribution, and remembering that the last cell current

is unitary, one obtains

$$\begin{aligned}
V_{c1} &= \frac{1}{j\omega C_1^L} \left\{ 1 - \left(\sum_{p=1}^N \varepsilon_p^* \right)^2 + \sum_{p=1}^N \varepsilon_p^* \sum_{q=1}^N \varepsilon_q^+ \left[\frac{N - (-1)^{(1-q)}}{N} \right] - \right. \\
&\quad \left. - \sum_{p=1}^N \varepsilon_p^* \sum_{q=1}^N \varepsilon_q^- \left[\frac{2q - N - 1}{N} \right] \right\} + \frac{1}{j\omega C_N^R} \\
&\cong \frac{1}{j\omega C} \left\{ 1 - \frac{1}{2} \left(\sum_{p=1}^N \varepsilon_p^* \right)^2 + \frac{1}{2} \sum_{p=1}^N \varepsilon_p^* \sum_{q=1}^N \varepsilon_q^+ \left[\frac{N - (-1)^{(1-q)}}{N} \right] \right. \\
&\quad \left. - \frac{1}{2} \sum_{p=1}^N \varepsilon_p^* \sum_{q=1}^N \varepsilon_q^- \left[\frac{2q - N - 1}{N} \right] - \frac{K}{4} \left(\frac{\varepsilon_1^L + \varepsilon_N^R}{2} \right) \right\}
\end{aligned} \tag{4.67}$$

Each voltage is characterized by an unperturbed term, a perturbed term that depends on the errors of all the cells and a local term that depends on the capacitances of the cavity we are considering.

It is apparent that the field is flat, if the voltages are near the mean value V_{cm} , evaluated on the odd cavities. Therefore, the expression of the mean square error σ_{rms} is defined as

$$\sigma_{rms} = \sum_{oddi} (V_{cm} - V_{ci})^2 \tag{4.68}$$

and this value is an index for the flatness of the voltages in the equivalent model, and therefore of the field in the cavities.

One can use the value (4.68) in the research of the best disposition of the cavities after all the possible permutation. For example in figure 4.5 is shown the voltages on the capacitance of a generic disposition, where the figure 4.6 shows the best disposition with the same errors. The numeric values were obtained with the help of a MATLAB program.

5. Conclusion

In this short section we resume the results obtained with the perturbation approach. Let us start from the resonant frequency of the whole structure.

- The $\pi/2$ mode frequency error depends only on the accelerating cavities errors and does not depend on the position of cavities.
- Moreover, the frequency is the arithmetic mean of the accelerating cavities frequencies.
- The variance of $\Delta\omega$ is N times smaller than the one of the random variable $\delta_{\omega 0p}^a$.

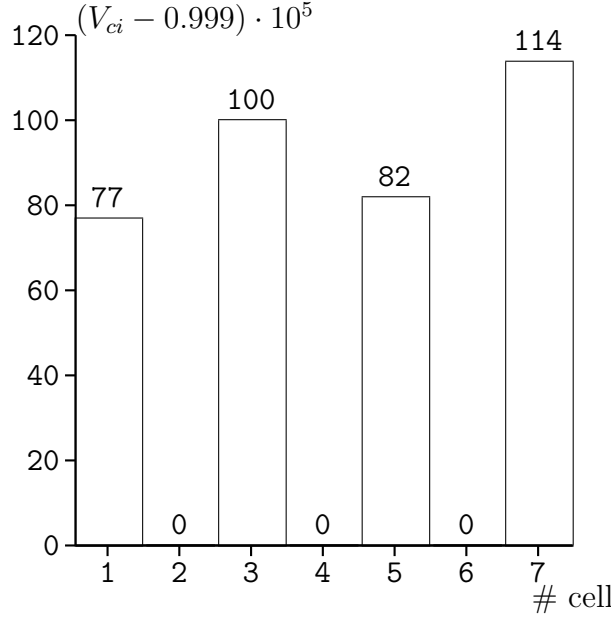


FIGURE 4.5. The relative level of field in the cavities for a generic disposition of the cavities, $N = 8$, $\delta\omega_0/\omega_0 = 0.001$ and $K = 0.04$ and $\sigma_{rms} = 8.81 \cdot 10^{-8}$. The computed values are normalized to the unity, but are shown using the formula $(V_{ci} - 0.999) \cdot 10^5$ for a better visualization.

Even though, it is worth remember that these results were obtained under the hypothesis of negligible non-adjacent cavities coupling and of infinite quality factors for all the cavities.

The second point, which should be true also without the previous hypothesis, leads to very interesting tuning procedure of such a structure. One could think to act on all the accelerating cavities frequencies of the same quantity, in order to change only the mean value. This point simplifies the tuning procedure and is discussed in the next chapter.

Finally, let us give some comments on the third point: the $\delta\omega_{0p}$ is due to the machining tolerances and one can assume that quantity as a random gaussian variable with a mean equal to zero and a variance equal to σ^2 . It follows that the error $\Delta\omega$ is still a gaussian variable whose variance is $\sigma_{\Delta\omega}^2 = \sigma^2/N$.

About the flatness of the axial field, starting from the expressions (4.66) and (4.67), we have already identified the parameter (4.68) as a good figure of merit. One could use a numerical program making all the permutation and using σ_{rms} as optimization parameter. For example, in the best disposition of figure 4.6, it is $\sigma_{rms} = 4.54 \cdot 10^{-10}$, where in the generic disposition of figure 4.5, it is $\sigma_{rms} = 8.81 \cdot 10^{-8}$. Concerning this last point, it is worth noting that the errors in the cavities are experimentally measured and, as we state in the next chapter,

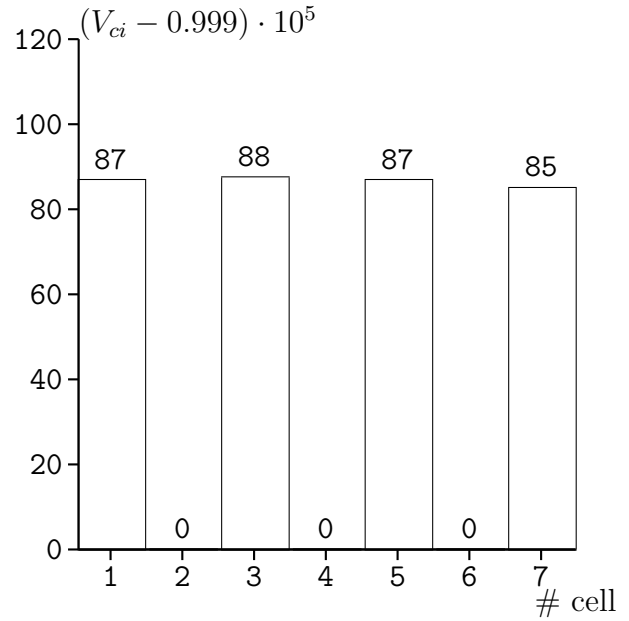


FIGURE 4.6. The relative level of field in the cavities for the best disposition of the cavities, $N = 8$, $\delta\omega_0/\omega_0 = 0.001$, $K = 0.04$ and $\sigma_{rms} = 4.54 \cdot 10^{-10}$. The computed values are normalized to the unity, but are shown using the formula $(V_{ci} - 0.999) \cdot 10^5$ for a better visualization.

they are affect by a measurement error. Therefore, the procedure of optimization is effective when the measurement error is proportionally smaller than the measured values.

Radiofrequency Measurement

In this chapter a detailed description of the radiofrequency (RF) measurement performed on LIBO prototypes is presented. RF measurement are very important on this type of structures, since they are the only way to correct the unavoidable errors that are mirrors of the mechanical machining tolerances. Note that the errors we have dealings with can be big enough to need a correction to get the desired design value for the main electromagnetic parameters, even if they are very small (for example, the frequency error of each cavity is typically included within the 0.1%).

In the following, each section begins with an overview on the technique, the instruments and the tools used for the specific measurement explained: single cavity and coupled cavities measurement are presented, and for each type of measurement, specific tasks for LIBO are illustrated. The tuning procedure to obtain a *flat* longitudinal electric field for the whole LIBO module is also presented.

1. Introduction

In the analysis of structures where the geometrical dimensions are comparable with the wavelength of the electromagnetic signals, it is correct to use the concept of reflected and transmitted waves rather than currents and voltages, since propagation effects become very important.

In this frame, the parameters of interest are the scattering parameters, namely the reflection and the transmission coefficients [33].

The sequence of RF measurement to perform is quite the opposite of the one used for the design. Indeed, the tiles with two half cavities are normally the first pieces built and then the first measurement is on the single cavities. In figure 5.1 it is shown a flux diagram of the procedures adopted with LIBO to build up the module, involving both measurement and machining on the copper pieces.

First, as we said, one starts from the measurement on the tiles, as they come out from the mechanical workshop. On these pieces three types of measurement are performed: coupled cells measurement giving coupling coefficients and resonant frequencies, single frequency measurement and stacked cell measurement that gives the $\pi/2$ mode frequency and the stop-band amplitude. If the values are not correct and/or present a large dispersion around the design values, one can

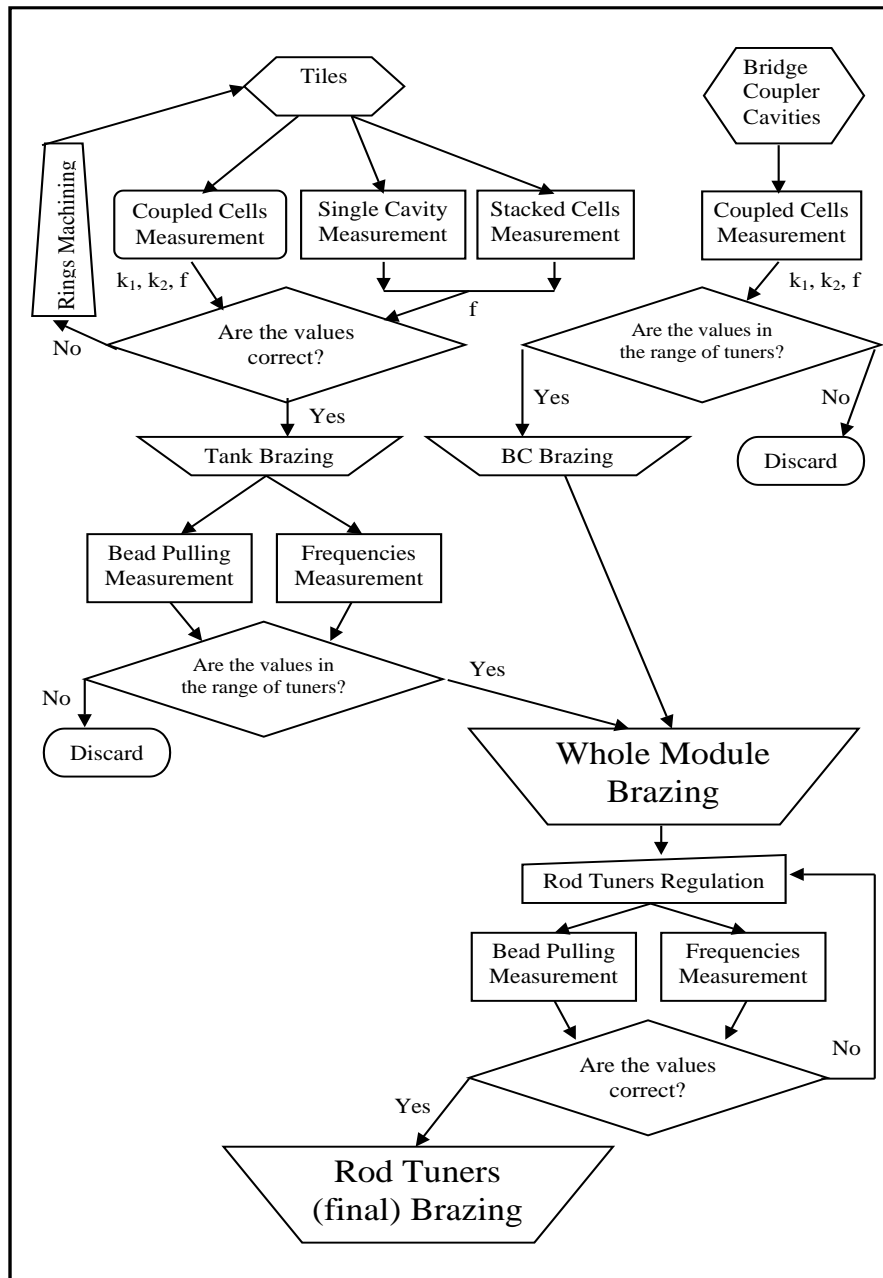


FIGURE 5.1. The flux diagram of the measurement and machining procedure.

work on the rings in the half cavities to change the frequency and on the slot dimensions to change the coupling. Then, the tiles are brazed together to make a tank. On this structure frequency and bead pulling measurement are done; first measurement changing the lateral rod tuners positions can be made as well, in order to control that the

design parameters are reachable. This step is repeated for all the tanks in the same way.

On the other hand, the bridge coupler pieces are stacked to make coupled cells measurement and to control that the design values are in the movable tuner range.

Once these steps are finished, the whole module brazing is made, and after, one deals with a structure where it is still possible to move the rod tuners in the cavities and the tuners in the three bridge couplers. Last, the hard point has to be fixed: after regulations on all those tuners, one control the $\pi/2$ mode, by means of a frequency measurement, and the axial electric field by means of a bead pulling measurement. The procedure go ahead with the help of the empirical criteria found with the equivalent model and with lots of patience and skill operators. At the same time, one has to control the coupling between the waveguide and the whole module and has to choose the length of the short-circuited waveguide (see figure 3.11).

Finally, after the parameters are fixed within the design ranges, the rod tuners are also brazed and the module is ready for the power tests.

2. RF Measurement on a single cavity

As it is shown in the previous chapters, a resonant mode of an electromagnetic cavity can be fully represented by only three parameters: resonant frequency, quality factor and shunt impedance.

By using a network analyzer and some mechanical and electrical tools, it is possible to measure all these three parameters. In principle, these measurements are very easy, but a big effort has to be made in order to get correct results and to avoid systematic errors when one measures the cavities of a structure such a LIBO.

2.1. Measurement of the resonant frequency. The measurement of resonant frequency on a closed cavity (excepted for the beam holes) is performed using probes which penetrate until the inner surface of the cavity. One probe allows the measurement of reflection coefficient, whereas two probes allow measurement of transmission coefficient. It is apparent that the cavity should has one or two holes for the probes, unless the beam holes are used. The probes are realized in the following two ways:

- *electric pick-up* which is a rigid coaxial cable, whose internal conductor juts out of about 4 mm over the external one. This type of antenna should be used where the electric field is strong¹. In figure 5.2 an example of realization is shown.
- *magnetic loop* which is a rigid coaxial cable, whose internal conductor juts out over the external one and realizes a loop

¹It could be put along the axis of the cavity through the beam hole where the longitudinal electric field should be strong.

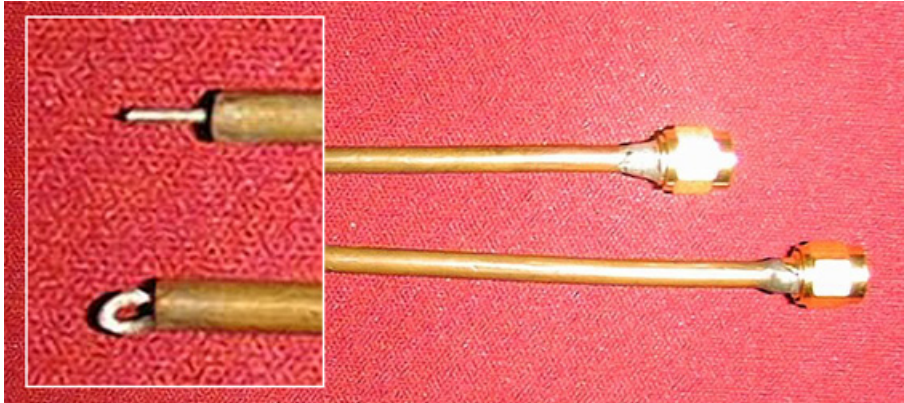


FIGURE 5.2. Electric pick-up (up) and Magnetic loop (down) for radiofrequency measurement in cavities.

soldered on the external conductor. The solder assures the electric contact. This type of antenna should be used where the magnetic field is strong and the loop can concatenate magnetic flux. In figure 5.2 an example of realization is shown.

The probe must be introduced in the cavity at a depth which assures a certain coupling. To avoid perturbation to the cavity field and hence to the resonant frequency, this coupling should not be too large. As a rule of thumb, we can consider a good coupling for each pick-up when the minimum of the reflection coefficient is around 0.5 dB below the reference level outside of resonance.

Once the frequency range for the network analyzer is restricted around the resonant behaviour, the resonant frequency is that which corresponds to the maximum of the transmission coefficient, or to the minimum of the reflection coefficient. The error of the measurement is mainly due to the resolution of the used instrument².

The measurement of the resonant frequency for an half cavity is more difficult. In this case the measurement is performed closing the half cell on an *electric mirror* which is a good conductor plane³. In this situation, a good electric contact between the conductor plane and the limit surface of the half cavity must be assured, in order to have a high quality factor and a good frequency measurement. But on the other hand, one has to be sure that both the half cavity and the plane are not deformed after the measurement. In conclusion, this type of measurement has the high risk to produce systematic errors and then a statistical approach is preferred, as it is shown in the next section.

²For example, a measurement with 100 points over a frequency range of 100 MHz gives an error of ± 1 MHz.

³From electromagnetic theory it is known that the equivalent circuit of this configuration has half inductance and double capacitance and the resonant frequency does not change.

In figure 5.3 the necessary mechanical tools and a particular solution of electric mirror are shown: the half cavity rests on a plane and is closed on a circular surface whose diameter is bigger, of a few millimeters, than the cavity diameter. The pressure on the contact reference surface can be controlled by using a dynamometric key and should be kept below the mechanical limit of plastic deformations for the material used for the cavities.

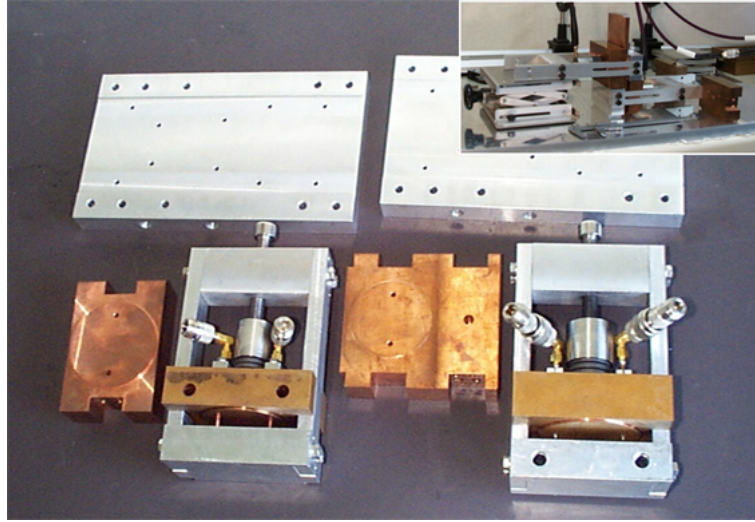


FIGURE 5.3. Mechanical tools for RF measurement on the LIBO tiles. On the top right the use of these tools is shown.

2.2. The statistical approach to the measurement of the frequencies of LIBO cells. Frequency measurement of half cavities on electric mirror can be source of systematic errors. In fact, it is very difficult to realize a good contact between the cavity and the conductor plane, even if a reference contact surface is realized. The measurement is not reliable for each cavity, but a statistical approach can be used.

As it is explained in section 4, in LIBO project the single tiles which form a tank contain two half cavities with a ring. The height of this ring can be machined in order to change the volume of magnetic field, and then the resonant frequency. This operation implies only a decrease of resonant frequency. For this reason, the half cavities are designed with a resonant frequency which is higher than the desired value and, in this sense, there are no cells which do not need interventions, since all the cells have to be corrected to the required resonant frequencies using the machinable ring.

In figure 5.4 is shown the dispersion of frequencies value for the half cells in the tiles around the mean value. The frequencies are measured with an unknown systematic error which, due to the mechanical tools,

result to be the same for all the cells. Each cell has a Δf_i with respect to the calculated mean value.

After the measurement of the single frequencies, all the cells are staked together and the resulting $f_{\pi/2}$ and the stop-band value are measured. This value is very reliable since it comes from a measurement over 30 cells⁴ and the systematic error due to the pressure on the first and the last cells does not play a recognizable role. The modification to be done on the ring of the single accelerating half cavity is calculated to correct the following frequency error

$$\Delta f_i^{AC} + (f_{\pi/2meas} - f_{\pi/2goal}),$$

where the $f_{\pi/2goal}$ is the design frequency which takes into account all the difference with respect to the effective operating conditions. In this sense, the steps of correction make the dispersion around mean value smaller and also make the mean value approaching the goal frequency.

For the coupling cavities, the correction takes into account also the measured value of the stop-band

$$\Delta f_i^{CC} + (f_{\pi/2meas} - f_{\pi/2goal}) + \Delta f_{SB},$$

where Δf_{SB} is considered with its sign.

In figure 5.4 the results after each intervention are shown. The dispersion is reduced to a part over ten thousand for a frequency error which is largely in the margin of intervention of the movable tuners available after the brazing.

2.3. Quality factor measurement. From the electromagnetic theory it is known that the quality factor can be defined as

$$Q = \frac{f_0}{\Delta f}$$

where f_0 is the resonant frequency and Δf is the positive difference between the two frequency at which the transmission coefficient is 3 dB lower than the resonant peak. Often, the network analyzer has already this function inside. It is worth noting that for this measurement the probes must perturb the cavity as little as possible, in order to get the correct value for the quality factor. Otherwise the probes drain power and the measurement is not correct⁵.

In this sense, the measurement of the quality factor for the half cavity rested on the conductor plane is not so significant, since incorrect values could arise from imperfect contacts at the joints. At least, the measurement could not be repeatable and reliable. In this case, the measurement of quality factor is necessary only to be sure that the

⁴Note that 30 is greater than the requested number of tiles (25) for a tank. But, of course, more than the needed tiles are produced in order to discard the worst ones.

⁵In this case the quality factor is said *loaded*. This concepts is explained in the last paragraph.

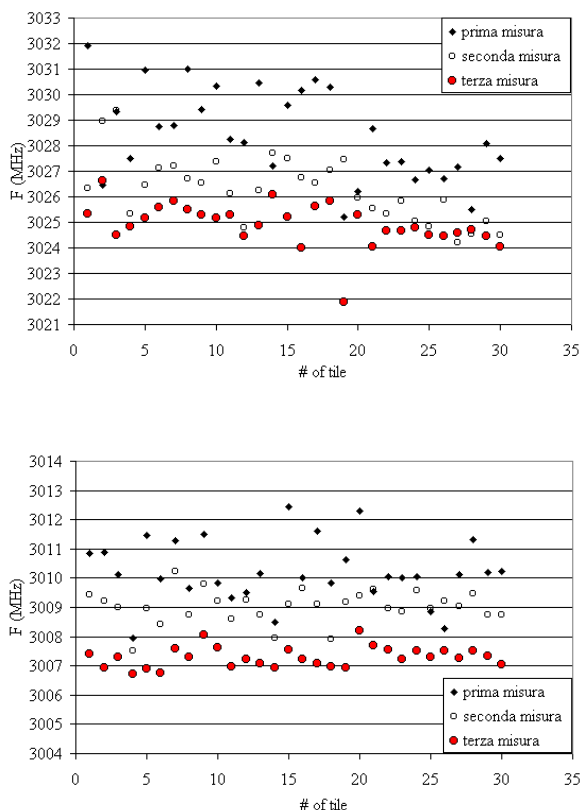


FIGURE 5.4. The dispersion of frequencies before and after two steps of machining on the rings for the accelerating and coupling half cavities in the tank #1. For the accelerating cavities the dispersion around mean value is reduced to roughly 1.5 MHz (left), whereas for the coupling cavities is less than 1 MHz (right).

quality factor is sufficiently high to give the requested precision on frequency measurement.

2.4. Shunt impedance measurement. Although several techniques can be conceived to permit the direct measurement of the shunt impedance, indirect methods are preferred. In fact, the ratio between shunt impedance and quality factor R_{sh}/Q do not depend on frequency and losses but only on geometrical factors. This fact implies that the measurement of R_{sh}/Q is more reliable than the direct measurement of the shunt impedance. In fact, the cavity under test can be built with two half parts or with an half part rested on a conductor plane because the losses in the joints do not affect appreciably the distribution of the fields and therefore, the measurement of R_{sh}/Q .

Then, if the measurement of a single prototype with a low quality factor is performed, one can use an electromagnetic simulator to

deduce the value of the quality factor; for brazed cavities, Q can be measured with accurate methods, or can be extrapolated from numerical calculations. Therefore, this procedure provides an indirect method to determine the shunt impedance R_{sh} .

In the following a perturbation technique is shown [34] which involve the measurement of the resonant frequency of the cavity as a function of a certain perturbation objects.

Remembering the definition of quality factor and shunt impedance

$$Q = \omega \frac{\text{energy stored}}{\text{energy lost per second}} = \frac{\omega U}{W}, \quad R_{sh} = \frac{\left(\int \mathbf{E} dl \right)^2}{2W}$$

where W is the power loss and the integral is usually calculated along the axis where the particles pass through the cavity. If the electric field \mathbf{E} is constant along the path of integration, it is valid that

$$R_{sh} = \frac{d^2 \mathbf{E}^2}{2W},$$

where d is the length of the path, which should be the acceleration gap. Combining the two definitions

$$R_{sh}/Q = \frac{d^2 \mathbf{E}^2}{2\omega U}.$$

The quantity \mathbf{E}^2/U can be determined experimentally by placing a perturbing object of volume $\Delta\tau$ into the cavity where the electric field is quite constant and measuring the resultant change in frequency. From Slater Perturbation theorem [34, 36]

$$\frac{\Delta f}{f} = -\frac{\alpha \varepsilon \Delta\tau \mathbf{E}^2}{4U},$$

where α is a constant which depends on the shape and on the material of the perturbing object. It should be determined from the measurement on a cavity with a known electric field distribution. Combining the previous relations one obtains

$$R_{sh}/Q = \frac{-2d^2 \Delta f}{\alpha \omega \varepsilon f \Delta\tau}, \quad (5.1)$$

which links R_{sh}/Q and the change in frequency due to the perturbing object.

It is worth noting that, in principle, it is not necessary to know the constant α for the perturbing object. In fact, the equation (5.1) depends on the derivative of the change in frequency and therefore, it could be evaluated also for the unperturbed point (zero displacement for the perturbing object), leading automatically to $\alpha = 1$.

In order to have a more accurate measurement, it is possible to measure also points when the plunger is displaced inside the conductor plane, in order to have *negative* displacements. Finally, note that in

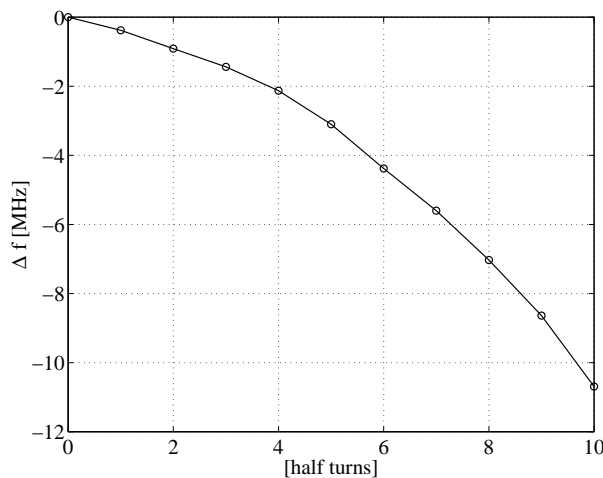


FIGURE 5.5. The change in frequency due to a metallic plunger for the measurement of r over Q .

the calculation it is only necessary to use known relative steps advancement for the plunger, rather than exact measurement of how much the plunger penetrates into the cavity.

Consider, for example, the figure 5.5. It shows the typical change in frequency due to a 2.3 mm diameter cylindrical plunger which penetrates, through a conductor plane, an half pill-box like cavity with a resonant frequency of 3.0359 GHz. The plunger is moved through a series of positions at which the changes of resonant frequency are measured. The slope is determined from a numerical interpolation of the curve.

3. RF Measurement on coupled cavities

From the electromagnetic theory it is known that two or more resonators coupled together lose their single resonant frequencies and meet in a number of modes equal to the number of resonators [17]; those frequencies mainly depend from the single resonant frequencies and from the coupling between the resonators. In few words, the resonant modes of the coupled cavities correspond to all the possible *ways* to satisfy the *new* boundary condition.

From the single cavity point of view, also the own resonant frequency is modified from the coupling mechanism. For example, an aperture between two cavities in a zone where the magnetic field is strong changes the stored magnetic energy of the cavities and, as a consequence, the single resonant frequencies.

In principle, it is possible to measure the single resonant frequencies also when the cavities are coupled together, it is sufficient to short-circuit the cavities near the one under measurement⁶.

Aim of this paragraph is to show a method which allows the measurement of the own resonant frequencies and the true coupling coefficient between two or three coupled cavities. The method is characterized by an high degree of reliability.

3.1. Coupling measurements on two cells. In the case of two coupled cavities, the system can be represented by an equivalent lumped circuit, as it is explained in chapter 3, and by using the Kirchhoff equations one can obtain [17]:

$$\left(1 - \frac{f_1^2}{f^2}\right) \left(1 - \frac{f_2^2}{f^2}\right) = k^2, \quad (5.2)$$

where f_1 and f_2 are the single cell frequencies (without any coupling), k is the coupling coefficient and the equations are written for an infinite quality factor. The two resonant frequencies of the coupled system are the solutions of the above equation with respect to f :

$$f_{\pm}^2 = \frac{1}{1 - k^2} \left[\frac{f_1^2 - f_2^2}{2} \pm \sqrt{\frac{f_1^2 + f_2^2}{4} - f_1^2 f_2^2 (1 - k^2)} \right] \quad (5.3)$$

In these relations f_1 , f_2 and k are unknown quantities. From an experimental point of view, one measures the two frequencies of the coupled system f_{\pm} (looking at the transmission coefficient of the system) keeping one cavity unperturbed and varying the other one by introducing a perturbation in the cell.

In this way, varying the perturbation we measure the corresponding resonance frequencies f_{\pm} , both modified, for each couple of unknown values, f_1 and f_2 - the first one fix and the second variable.

Starting from equation (5.3) and looking for invariant expressions we can find useful relations between the unknown quantities and the measured ones. We used two methods, one more general and the second

⁶The measurement on a single cavity stacked in a tank is possible if one short-circuit the cavities near the one under measurement. This technique takes into account the coupling slots effect and the relative frequency change, but they do not allow the measurement of coupling coefficient k . Furthermore this procedure, still having a high degree of sensibility (depending on the instrument), it is not sufficiently precise for our purpose, since it introduces a systematic error on the frequency. This error depends on the particular realization of short-circuit and cannot be always determined.

From the practical point of view, the short-circuited cavity becomes a coaxial cavity, which resonates at a higher frequency respect to the unperturbed cavity (for LIBO cavities the frequency goes from 3 GHz to around 5 GHz) but this frequency displacement depends on the type of short-circuit.

one [38] useful when the single cell frequency values are very close each other.

3.1.1. *Line method (more convenient if f_1 is not so close to f_2)*. Let f_2 vary and keep f_1 constant. We find a *linear* relation between $f_+^2 \cdot f_-^2$ and $f_+^2 + f_-^2$ as it follows

$$f_+^2 \cdot f_-^2 = (f_+^2 + f_-^2)f_1^2 - \frac{f_1^4}{1 - k^2}, \quad (5.4)$$

and by interpolating the data, we could get k and f_1 with their errors. The analysis gives a reliable value for f_1 with a great accuracy (relative error 10^{-5}), meanwhile k is obtained with less accuracy. The frequency f_2 can be obtained from the measured data when no perturbation is introduced through the relation:

$$f_2^2 = (f_+^2 + f_-^2)(1 - k^2) - f_1^2, \quad (5.5)$$

and in figure 5.6 a typical case is shown.

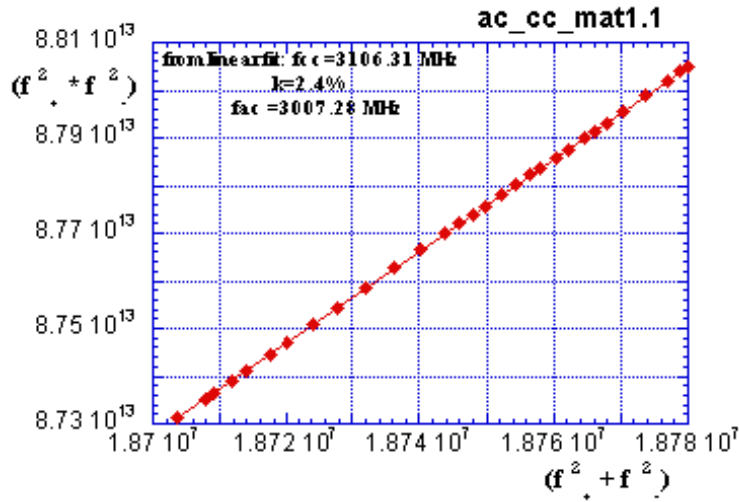


FIGURE 5.6. The result of the line method applied to two coupled cavities. The own frequencies f_{cc} and f_{ac} , and the coupling coefficient k are reported.

3.1.2. *Parabola method (convenient if f_1 is very close to f_2)*. Let f_2 vary and keep f_1 constant. If we introduce now the following variables:

$$k' = \frac{f_+^2 - f_-^2}{f_+^2 + f_-^2} \quad \text{and} \quad f' = \sqrt{\left(\frac{f_+^2 + f_-^2}{2}\right)} \quad (5.6)$$

and plotting k' as function of f' , we obtain a *parabola*, whose minimum is reached when $f_2 = f_1$. The minimum gives us the value of the true coupling coefficient k and of f_1 , the other unknown frequency can be extracted as before from a unperturbed measurement by using the equation (5.5). The f_1 value corresponds to the $\pi/2$ mode. This

method gives a reliable k value with a small error. In figure 5.7 a typical case is reported.

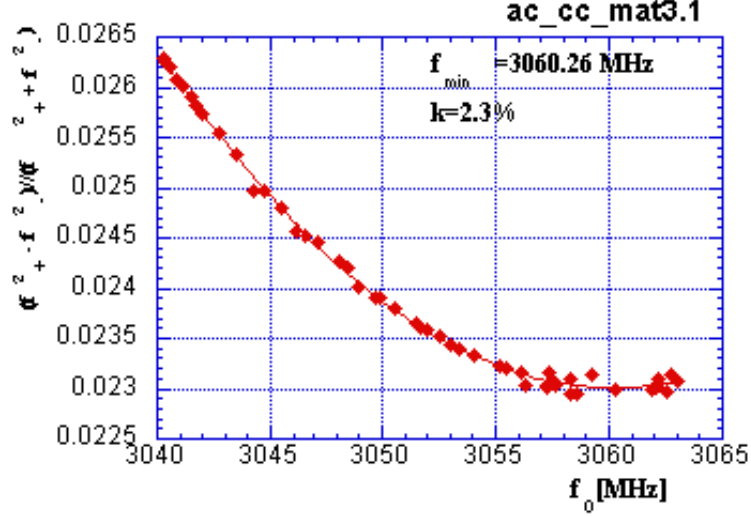


FIGURE 5.7. The result of parabola method applied to two coupled cavities. The coupling coefficient and the minimum frequency, which is the one of the $\pi/2$ mode, are reported.

The method gives an high degree of reliability since it is based on a set of measurement. This means that it is possible, using standard techniques, to evaluate the correctness of the results and the reliability of the procedure. The method can not be applied to cavities whose frequencies are very different since too large perturbations could be necessary to reach the minimum; in this case the behaviour of fields in the perturbed cavity could be too much modified.

3.2. Measurements on three coupled cells. In the case of three coupled cells with f_0 , f_1 and f_2 resonant frequencies respectively, the theory of the coupled resonators gives for the resonant frequencies of the coupled structure the following solutions (valid in the particular case of $f_0 = f_2$, for the bridge coupler case, these are the coupling cavities frequencies):

$$\tilde{f} = \frac{f_0}{1 + k_2/2} \quad (5.7)$$

$$f_{\pm}^2 = \frac{[f_0^2 + f_1^2(1 - k_2/2)] \pm \sqrt{[f_0^2 - f_1^2(1 - k_2/2)]^2 + 2f_0^2 f_1^2 k_1^2}}{1 - k_2/2 - k_1^2/2} \quad (5.8)$$

where f_{\pm} and \tilde{f} are the measured frequencies, k_1 and k_2 are the coupling of first and second order and f_1 is the resonant frequency of the bridge coupler central cavity.

By manipulating these solutions we obtain a linear relation between two functions of the measured frequencies:

$$\frac{\tilde{f}^2}{f_+^2} + \frac{\tilde{f}^2}{f_-^2} = \frac{1 - \frac{k_2}{2}}{1 + \frac{k_2}{2}} + \frac{1 + \frac{k_2}{2}}{1 - \frac{k_2}{2} - \frac{k_1^2}{2}} \frac{\tilde{f}^4}{f_+^2 f_-^2} \quad (5.9)$$

which relates k_1 and k_2 to the measured frequencies f_- , f_+ and \tilde{f} . From the interpolation of the data we can obtain k_1 and k_2 with their errors. If the bridge coupler central cavity is the perturbed cavity, its frequency can be obtained from the first unperturbed data:

$$f_1^2 = \frac{f_+^2 f_-^2}{\tilde{f}^2} \frac{1 - \frac{k_2}{2} - \frac{k_1^2}{2}}{1 + \frac{k_2}{2}}, \quad (5.10)$$

and f_0 can be determined from the expression for the resonant frequency:

$$f_0^2 = (1 + k_2/2)^2 \tilde{f}^2 \quad (5.11)$$

3.3. An RF measurement procedure on a brazed LIBO tank. With the help of metallic rods and long pick-ups, the previous method can be applied also to a brazed prototype of a LIBO tank. We should make the following RF measurements:

- Resonant frequency (and quality factor) of Coupling Cells (CC)
- Resonant frequency (and quality factor) of Accelerating Cells (AC)
- First Coupling coefficient between AC and CC
- Secondary Coupling coefficient among ACs and CCs

We propose the use of metallic rods to short-circuit the cells not involved in the measurement. This solution makes the resonant frequencies of the short-circuited cells very high, and therefore the coupling with the cavities produces a small displacement (around 100 kHz) and comparable with the measurement error.

This method needs passing through holes in ACs and CCs. The ACs holes are fixed from the beam and have a 8 mm diameter. The holes for the CCs have to be made right for this measurement but can be chosen in a range which do not change drastically the mechanical construction⁷. Let us give a comment about the mechanical pieces needed for this measurement.

- AC and CC Pick-up rods are simple electric pick-ups (3.65mm diameter) of the right length. They do not have to touch the uninvolved cells. They simply arrive on the nose in the cell under measurements. With reflection coefficient measurements we control the perturbation (less than 0.5dB). Finally, we can

⁷A 5 mm diameter hole change the CC resonant frequency of roughly 8MHz, it does not introduce an appreciable coupling between adjacent CCs. Compare to the AC case: now the diameter of the hole is smaller than the beam hole and the space between cells is bigger too (very little coupling).

perform transmission measurements to easily get resonant frequency and quality factor⁸.

- AC Short-Circuit (SC) rod is able to short-circuit one AC cell.
- CC SC rod is able to short-circuit one CC cell.

In figure 5.8 the measurement on a stacked CC is shown. Four metallic rods short-circuit the adjacent cavities to the one under measurement and two pick-up rods makes the transmission coefficient measurement. In figure 5.9 the same scheme is proposed for the accelerating cavity. In figure 5.10 and 5.11 the measurement for the couplings are shown. Note that we can use the rods as perturbing object in the cavities.

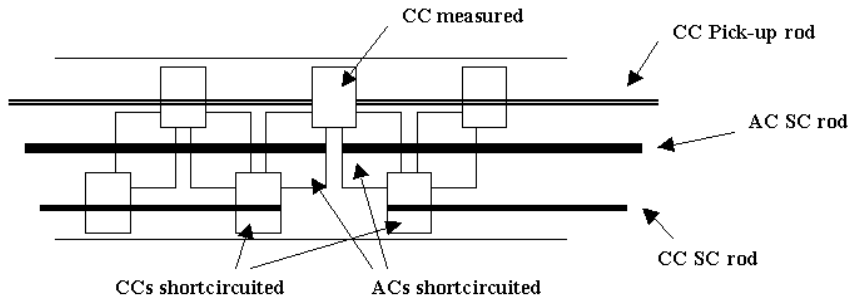


FIGURE 5.8. Measurement on a stacked CC using the rods.

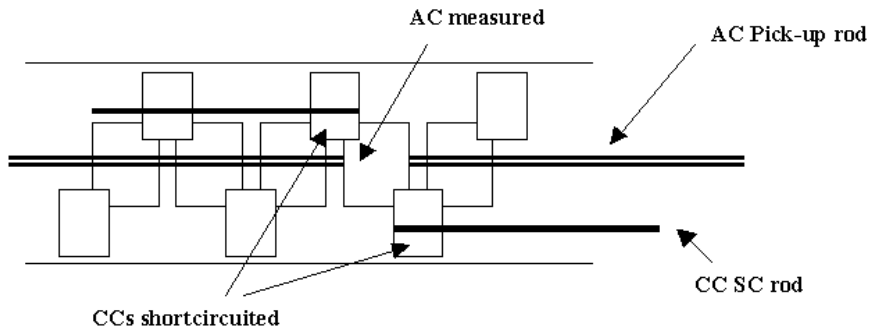


FIGURE 5.9. Measurement on a stacked AC using the rods.

4. Bead pulling measurement

In the construction of a linear accelerator the tolerance on the dimension of mechanical pieces and some unavoidable construction errors limit the ideal performances reachable in theory. This important fact implies several errors in the relevant parameters of the single cavities,

⁸Note that the quality factor in a brazed tank should be the design value and its measurement has a low error.

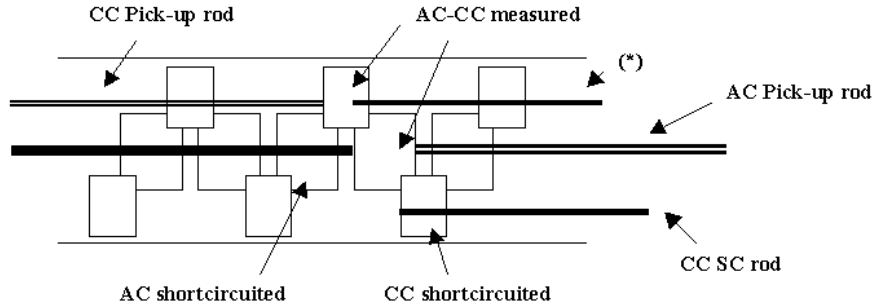


FIGURE 5.10. Measurement for the coupling for stacked cavities. In order to apply line and parabola methods, in addition to the AC and CC screws, one can move also (*) rod to change the CC frequency.

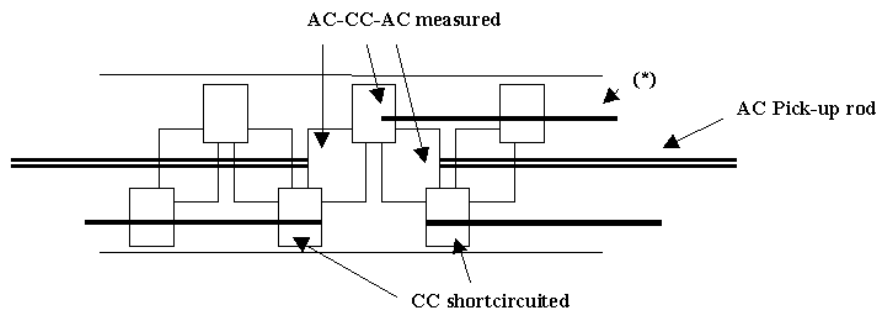


FIGURE 5.11. Measurement for the second order coupling for stacked cavities. In order to apply line and parabola methods, in addition to the AC and CC screws, you can move also (*) rod to change the CC frequency.

as the resonant frequency, or of the coupled cavities, as the coupling factor, or of the whole multi-cell structure.

For the whole structure, the parameter of interest is the electric field distribution along the axis, which is the field that the particles experience during their travel through the accelerator. It is very important that the electric field level in the accelerating cavities is *flat* within a certain tolerance.

In fact, a distribution field which present big relative differences between cavities could imply different results with respect to the longitudinal dynamic of the particles [21, 20].

Furthermore, as explained in chapter 2 the Kilpatrick criterion [26] will limit the maximum level of field reachable, since this one will be set for the cavity which presents the highest level, whereas in case of flat field this condition is the same for all the cavities.

All this means that it is required a RF measurement able to acquire the relative electric field distribution inside the cavities and this is possible using the bead pulling technique.

Bead pulling is a perturbation technique based on Slater's theorem [36, 37]. With the help of a perturbing object (the bead) which travels along the axis of the multi-cell structure, the electric field distribution is determined in terms of phase variation introduced by the bead. The multi-cell structure is driven at a fixed frequency that is the accelerating mode frequency.

The Slater perturbation theorem can be written as follows:

$$f^2 = f_0^2 \left[1 + \alpha \frac{\int_{\Delta\tau} (\mu \mathbf{H}^2 - \varepsilon \mathbf{E}^2) d\tau}{\int_V (\mu \mathbf{H}^2 + \varepsilon \mathbf{E}^2) dv} \right] \quad (5.12)$$

where α is a constant related to the particular perturbing object, the numerator represents the integration over the volume of the perturbing object and the denominator is equal to twice the average energy stored in the cavity U . If perturbation is small the (5.12) can be simplified to

$$\frac{\Delta f}{f_0} = \frac{\alpha}{4U} \int_{\Delta\tau} (\mu \mathbf{H}^2 - \varepsilon \mathbf{E}^2) d\tau. \quad (5.13)$$

This important relation states that the change in frequency depends upon the integral $\int_{\Delta\tau} (\mu \mathbf{H}^2 - \varepsilon \mathbf{E}^2) d\tau$. And, if the perturbing object acts in a zone where only the electric field is present in a significant way, the previous relation simplifies again.

Then, a procedure to measure the relative level of electric field in a multi-cell structure can be set up as follows:

- (1) A nylon wire is stretched along the longitudinal axis of the structure and some mechanical tools and a motor allow the movement of the wire. Note that the wire itself modifies the resonant frequency, since it is a dielectric⁹. Of course, a good alignment is needed between the wire and the axis of the cavities in order to have the same perturbation in all the cavities.
- (2) A perturbing object (the bead) is put on the wire. The dimensions should be little enough to perturb as little as possible the field distribution, but sufficient to give a good signal noise ratio. Using a cylindrical shape (a needle for example), the perturbation acts on the axis and only the longitudinal component of the electric field is perturbed.
- (3) The network analyzer drives the structure at the resonant frequency. The bead perturbs the electric field distribution along the axis and this implies a change in frequency¹⁰ and then, in the phase of the signal detected by the network analyzer.

⁹The nylon wire lowers the frequency since it acts in a zone where electric field is strong and, as in a capacitor, it canalizes the field lines.

¹⁰Strictly speaking, the bead grows the frequency.

Therefore, around resonances, the relative change of electric field is proportional to the change in phase shown by the network analyzer¹¹

$$\frac{\Delta E^2}{E^2} \propto \frac{\Delta \Phi}{\Phi}, \quad \text{for each cavity,}$$

- (4) The measurement is made in the time domain. The motor moves the wire and the bead through the cavities and the network analyzer shows the relative electric field level for each cavity. The longer is the measurement time, the more precise the measurement is. At high resonant frequencies, very long times need a temperature controlled laboratory, since even little changes in temperature imply changes of resonant frequency and this implies a linear slope in the output graph.

The figure 5.12 shows a schematic view of a bead pulling apparatus and the figure 5.13 shows a particular realization on the LIBO module. In a next paragraph several examples of bead pulling will be given, since the bead pulling measurement is a fundamental pawn to tune the LIBO module to the correct distribution field.

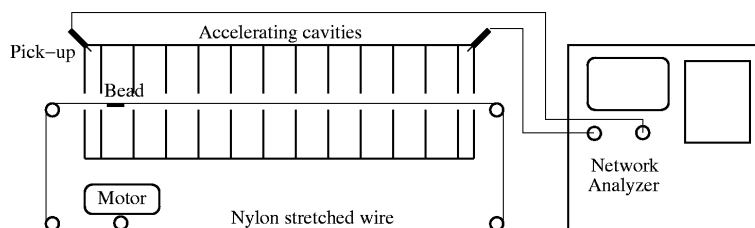


FIGURE 5.12. Sketch of a bead pulling measurement apparatus.

5. A tuning procedure for the LIBO module

In this section it is presented the procedure used to tune the first LIBO module. The bead pulling measurements reported on the following were made before the final brazing where the four tanks and the three bridge couplers were brazed together. The goal of the measurement was to fix the position of the rods tuners for the 102 cavities in the four tanks.

The facts are reported in a chronological order, and through the presentation of the followed steps, whereas it is convenient, some explanations are reported on the connected theory and on the technological aspect of the LIBO module.

¹¹It is better to use a driven frequency which is slightly different from the resonant frequency, because in this case the change in phase is always in the same direction, whereas at the exact resonant frequency some noise in the measurement can give results with a bigger error.

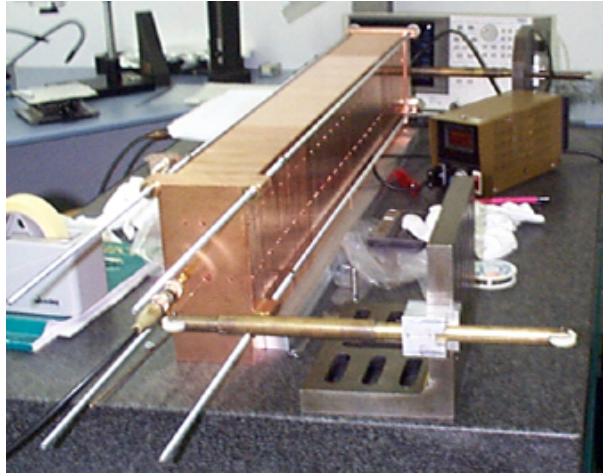


FIGURE 5.13. The particular realization of the bead pulling measurement for the LIBO module.

5.1. Preliminary considerations. In linear accelerators the level of the axial electric field in the accelerating cavities must be *flat* within a certain tolerance fixed by the dynamic of the beam. Usually, each cavity in LINACs has one or two tuners which are able to change the resonant frequency within 0.1% and, after that all the cavity are brazed together, these tuners are used for two important purposes: to make the whole resonant frequency at the value set by the power klystron, and to make the electric field level be flat in the cavities.

The beam dynamic of LIBO is not stringent and requires a flat field within $\pm 2.5\%$ [20, 21].

We remember that one LIBO module has 4 tanks and 3 bridge couplers. Each tank has 13 accelerating cells and 12 coupling cells which are out of beam axis. Each bridge coupler is composed by 3 cavities: two coupling cells and a cell which is equivalent to an accelerating cell but, as the others two cells, it is displaced out of the beam axis, in order to leave space for the permanent quadrupole magnet, placed between each two tanks.

It is worth remember that the resonant frequency of each cavity inside the four tanks ready for the bead pulling measurement has an error less than 500 kHz, respect to the $\pi/2$ frequency of the same tank. This result is obtained after the machining of the ring placed in each cavity, as it is explained in section 2.2. But this procedure does not leave out the possibility that the $\pi/2$ frequencies are different among the four tanks, in fact these were different within 500 kHz too. This means that we know that the tuners have to correct also this difference between the frequencies of the tanks.

Another consideration has be done about the bridge couplers. The movable tuners of this cells were used before the bead pulling, in order

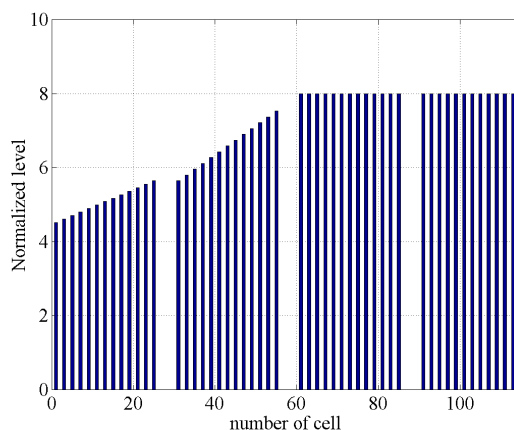


FIGURE 5.14. The bead pulling result after the bridge couplers tuning.

to have the design values for the frequencies, and, more important, to have the frequencies of the coupling cells perfectly equals. This is important, because any difference in the coupling cells of a bridge coupler produces a step in the electric field of the adjacent tanks.

5.2. Bead pulling measurement. The first bead pulling of the whole structure gave the result shown in figure 5.14. The figure shows the normalized level of the squared electric field in all the accelerating cavities; the space between two cavities represents the coupling cells. The space between two tanks is the one of the bridge coupler which is out of axis and the bead does not pass through its cells.

It is worth noting again that for the tuning procedure it is interesting only the relative levels between the tanks and not the absolute values, since this procedure is made at a low power level.

For the measurement of figure 5.14, the $\pi/2$ frequency was 2996.99 MHz. Taking into account all the variations due to the real conditions¹², the goal frequency should be 2997.10 MHz. The quality factor value was around 4500 which is a good value, but still far from the final 7200, this was due to the imperfect joints between the tanks and the bridge couplers, since they were not brazed together yet.

Also, in that configuration and from a frequency measurement, it was possible to evaluate the stop-band of the second nearest modes which was $SB_B = +216$ kHz. This stop-band is related to the *bump*-like behavior in the response of bead pulling measurement, its presence means that the second nearest modes in the dispersion diagram are excited and the behavior for these modes is just as a bump, having a minimum for the field (maximum) in the central bridge coupler cavity and a maximum field in the end cells (minimum).

¹²Vacuum effect, temperature, final brazing, etc..

tank #	cell type	left [mm]	right [mm]
1	AC	+2.3	+7.6
	CC	+0.3	+7.2
2	AC	+5.0	+6.2
	CC	+0.3	+7.2
3	AC	+5.0	+6.8
	CC	+0.3	+7.2
4	AC	out	+6.0
	CC	+0.3	+7.2

TABLE 5.1. Tuners positions for the bead pulling of figure 5.14.

Since all the bead pulling measurement was made feeding the module by the wave-guide, it was not possible to measure the first nearest mode stop-band. This stop-band is related to a *tilt*-like behavior in the response, since the nearest modes have a linear behavior from the first cell to the last one and have a null in the central cavity; this means that it is not possible to feed and to measure these modes from the wave-guide at a recognizable level.

Last, in the table 5.1 the tuners positions for the figure 5.14 are shown. Some comments on those values are necessary. For each tank, two *lines* of tuners are available for each type of cell¹³. Here, the left side is the one on the left when one looks the module from the first tank to the fourth one. It is also possible to act on one side at a time. The values shown represents the length of the part of the tuners that juts out of the tank side wall; again, this is not important for our purposes, since only relative displacement are relevant. In the table *out* means that the tuner are completely out and the end side of the tuner does not penetrate in the inner surface of the cavity. In the tuning process, the tuners for each tank have been moved all at the same time, as each tank should be one accelerating cavity and one coupling cavity and this fact has simplified very much the procedure. Consider the bead pulling measurement of figure 5.15. The only intervention was to push the tuners of ACs on the right side of tank #1 inside of +0.3 mm, because before the level of this tank was very low. Of course, the little displacement does not change dramatically the situation, but it is in the right direction since the level of tank #1 was increased. The $\pi/2$ frequency was increased to 2997.01 MHz and this was clear because the resonant frequencies of ACs of tank #1 were increased. The Bump stop-band was decreased to $SB_B = +201$ kHz and this was due to the fact that the mean frequencies of ACs increased where the ones of the CCs remained constant. In figure 5.16 is shown a bead pulling made

¹³A *lines* of tuners is constituted by a number of tuners that move together.

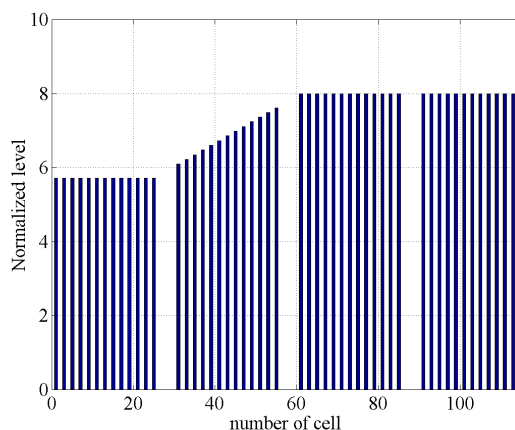


FIGURE 5.15. The bead pulling result after the first operation on tank #1.

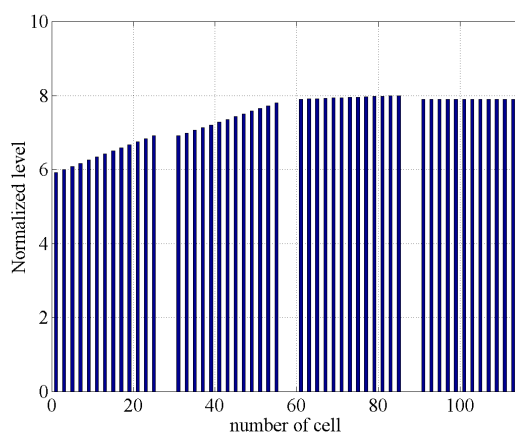


FIGURE 5.16. The bead pulling result before the first operation on all the CCs.

after similar intervention on the first two tanks. The $\pi/2$ frequency was increased to 2997.02 MHz and the bump stop-band was decreased to $SB_B = +178$ kHz. At that point an intervention on all the CCs was necessary in order to bring back the SB_B to bigger value.

This is a very important property of LIBO module, since it is possible to use the ACs tuning to level the field and to control the $\pi/2$ frequency and the CCs tuning to control the stop-bands.

But it is worth noting that the interventions on the tanks are effective and get clear results only if the stop-bands keep always the same sign. In fact, the bump and tilt effects are connected with the sign of the respective stop-bands and if one sign changes the relative effects change sign also (a bump with a maximum in the center becomes a one with a minimum in the center). For this reason, it was important

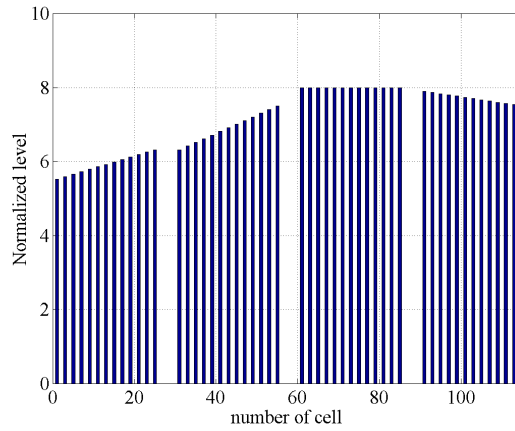


FIGURE 5.17. The bead pulling result after the first operation on all the CCs.

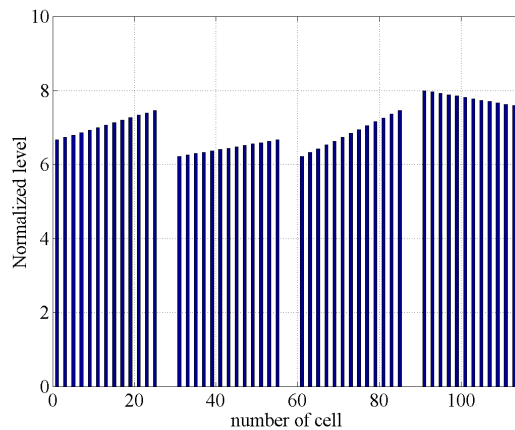


FIGURE 5.18. The bead pulling result for the tuners positions of table 5.2.

to keep the bump stop-band always to relatively big values, keeping in mind that at the end of the tuning procedure it should have been possible to decrease the stop-bands using the CCs tuning.

The figure 5.17 shows the bead pulling measurement after that the CCs enter inside of +0.3 mm on the left side. The $\pi/2$ frequency was unchanged and the bump stop-band increased to +270 kHz. It is clear that the intervention made worse the field level. This happened because the stop-band was bigger than in the previous situation. In fact, the entity of the bump and tilt effects are directly related to the entity of the respectively stop-bands. The bigger is the stop-band, the bigger is the effect of the nearest modes on the field level of $\pi/2$ mode.

tank #	cell type	left [mm]	right [mm]
1	AC	+3.5	+7.9
	CC	+0.3	+7.0
2	AC	+6.7	+6.2
	CC	+0.3	+7.0
3	AC	+5.0	+6.2
	CC	+0.3	+7.0
4	AC	out	+4.4
	CC	+0.3	+7.0

TABLE 5.2. tuners positions for the bead pulling of figure 5.18.

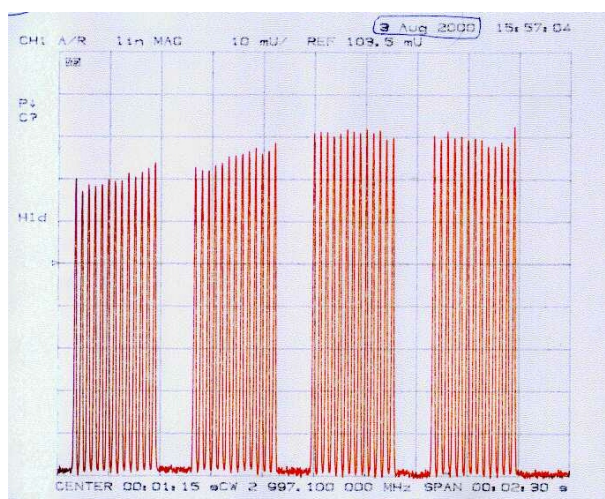


FIGURE 5.19. The first good bead pulling result.

The figure 5.18 shows the bead pulling measurement after some interventions on the tuners resumed in the table 5.2. The $\pi/2$ frequency was 2996.96 MHz and $SB_B = +222$ kHz.

6. The final steps of the tuning procedure

It is clear from the previous section that the tuning procedure should be made by little steps in order to be sure to keep positive the two stop-bands and to fully understand the results on the field level. Unfortunately, sometimes the intervention on one tank has also effect on the near tanks and this implies that all the interventions must be careful made and without big displacements of the tuners.

The figure 5.19 shows a bead pulling measurement¹⁴ that was quite good since the field level was flat within $\pm 5\%$. The $\pi/2$ frequency was

¹⁴Note that the figure 5.19 is the output plot of the network analyzer. The scale is the same of the previous figures, the maximum being 8 divisions.

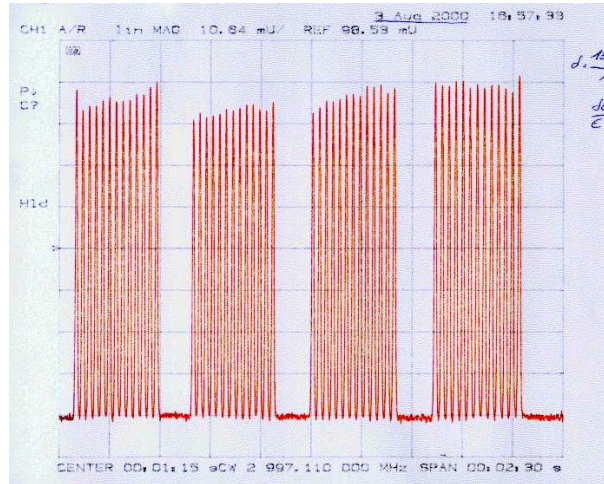


FIGURE 5.20. A bead pulling with the field level flat within $\pm 2.85\%$.

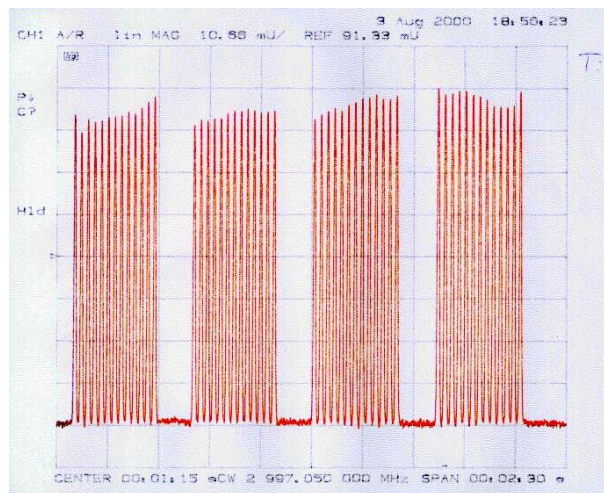


FIGURE 5.21. The final bead pulling with the field level flat within $\pm 2.5\%$.

2997.075 MHz and the $SB_B = +160$ kHz. After some interventions on the tanks #2 and #3, the bead pulling was the one of figure 5.20 which was flat within $\pm 2.85\%$.

The $\pi/2$ frequency was 2997.080 MHz and the $SB_B = +145$ kHz.

The final result is shown in figure 5.21 with the tuners positions shown in table 5.3. The $\pi/2$ frequency was 2997.025 MHz and it took into account the effect of temperature and of the nylon wire stretched along the axis. The bump stop-band was $SB_B = +212$ kHz.

6.1. Rejection to the disturbs. When a Side Coupled Linac is well tuned, namely the field level is flat and the stop-bands are little, the structure is able to reject disturbs. This means that, starting from

tank #	cell type	left [mm]	right [mm]
1	AC	+4.5	+6.6
	CC	+1.2	+6.4
2	AC	+6.2	+6.8
	CC	+1.2	+6.4
3	AC	+5.9	+4.4
	CC	+1.2	+6.4
4	AC	+2.0	+4.6
	CC	+1.2	+6.4

TABLE 5.3. The final tuners positions.

such a condition, a local error does not change significantly the flatness of field and the $\pi/2$ frequency. The figure 5.22 shows four cases of

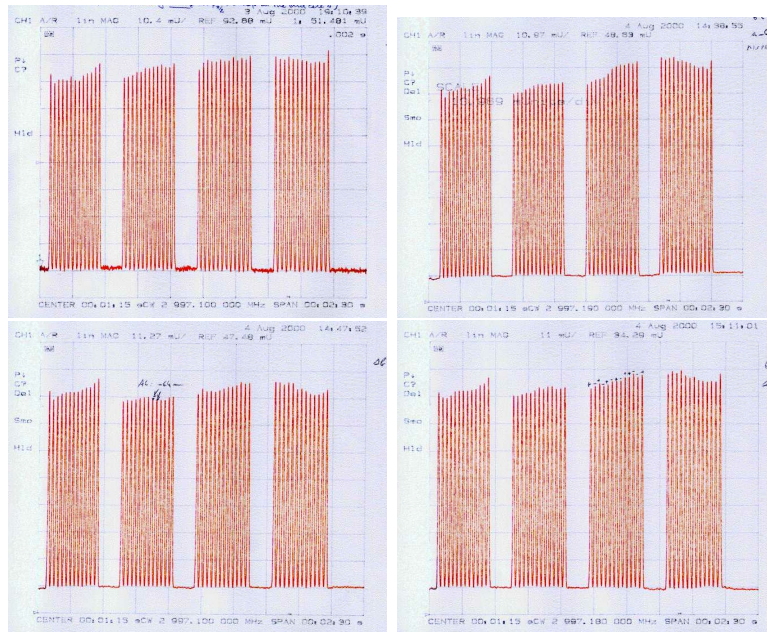


FIGURE 5.22. The effect of perturbations a) in the end cell, b) in 6 CCs (two for tank #1, #3 and #4), c) in 2 ACs in tank #2, d) in all the ACs of tank #3.

perturbation on the structure. In the case a) a magnetic loop was introduced in the end cell of the fourth tank and this implied a shift of the resonant frequency of 40 kHz. In the case b) the tuners of two CCs for the tanks #1, #3 and #4 were brought out of 0.3 mm. In the case c) the tuners of two ACs of tank #2 were completely brought out and, at last, in the case d) the tuners of seven ACs of tank #3 were brought out of 0.4 mm and the tuners of six ACs of tank #3 were pushed inside of 0.4 mm.

In all the cases it is clear that the differences respect the reference case of figure 5.21 were acceptable.

In figure 5.23 is shown the effect of a perturbation on the CCs which are nearest to the bridge coupler. From first bead pulling, which are the reference, it is apparent that the level of field in the last AC of tank #1 is high respect to the mean of the tank, the theory says that if the nearest CC is changed the level in the following AC (respect to the feeder) changes also.

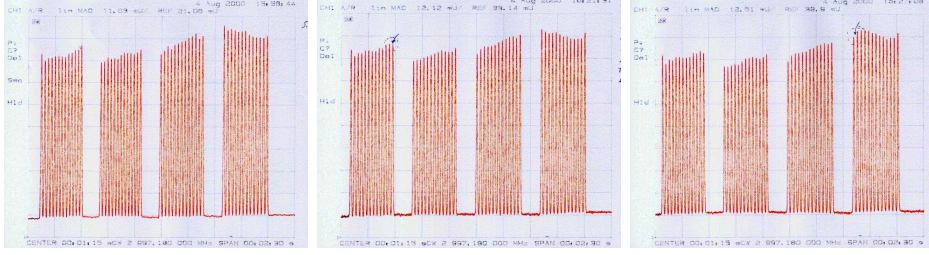


FIGURE 5.23. The effect of local perturbations in the CCs at the end of a tank.

7. Measurement of the coupling between the module and the waveguide through an iris

In this paragraph the procedure to measure the coupling between the power waveguide and the LIBO module is explained [34]. The procedure is exportable to other cases, as the case of multi-cells structures fed by one cavity through an iris.

First, we introduce some basic concepts and the equivalent circuit, then we introduce some figures of merit to evaluate the correct matching, next we explain the RF procedure to get the numerical data with the help of a Network Analyzer; last we introduce a numeric MATLAB program that, starting from the measurement data, is able to deduce the desired figures of merit, and finally we comment the results.

7.1. The equivalent circuit for one cavity. In the previous chapters we already introduced the concept of equivalent lumped elements circuit for resonant cavities. Of course, we know that the equivalent description is rather difficult because, as in wave-guides, the ordinary concept of voltage and current does not play its usual role.

$$\omega_0^2 = 1/LC, \quad Q_0 = \frac{\omega_0 L}{R_s}, \quad R_0 = \omega_0 L Q_0 = \frac{(\omega_0 L)^2}{R_s} \quad (5.14)$$

The three quantities defined by these relations can be measured experimentally, as it is shown in the previous sections, and can be used to establish the lumped elements

$$L = \frac{R_0}{\omega_0 Q_0}, \quad C = \frac{Q_0}{\omega_0 R_0}, \quad R_s = \frac{R_0}{Q_0^2}. \quad (5.15)$$

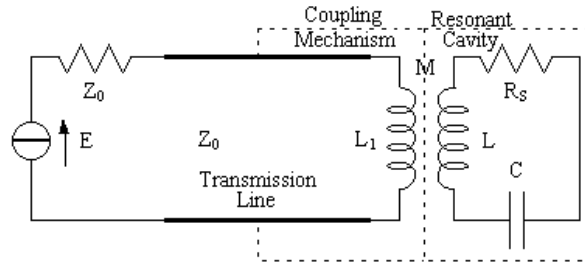


FIGURE 5.24. Coupling through an iris. Sketch of a resonant cavity coupled with a transmission line.

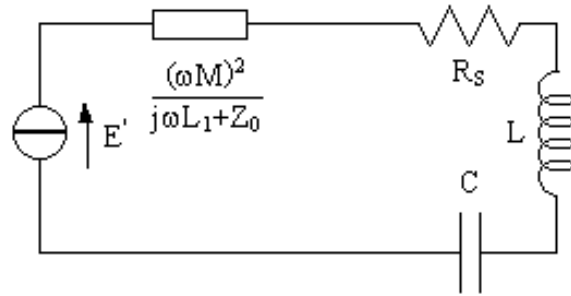


FIGURE 5.25. Coupling through an iris. The generator is referred to the secondary.

These set of parameters are involved in a equivalent circuit that represent the cavity in one mode and can be used in most applications.

7.2. Equivalent circuits, definitions of Q_0 , Q_L , Q_{ext} and coupling coefficient β . Consider a signal generator connected to a transmission line, those characteristic impedance Z_0 is equal to the internal impedance of the generator. The transmission line is coupled to a resonant cavity through a magnetic coupling mechanism. The resonant cavity is represented by a lumped circuit as it is shown in figure 5.24.

The magnetic coupling mechanism is represented as a transformer, where L_1 is the auto-inductance and M is the mutual-inductance of the transformer. The coupling mechanism is supposed to be without loss.

We can either refer the cavity impedance to the primary or to refer the generator to the secondary. The latter case leads to the definition of *matched generator*, whose internal impedance is

$$Z = \frac{(\omega M)^2}{j\omega L_1 + Z_0}, \quad (5.16)$$

and this leads to the circuit of figure 5.25.

We can write the definition (5.16) as

$$Z = \frac{(\omega M)^2}{Z_0[1 + (X_1/Z_0)^2]}(1 - jX_1/Z_0) = R_c(1 - jX_1/Z_0), \quad (5.17)$$

where R_c is called *coupled resistance* and $X_1 = \omega L_1$. Let us introduce the definition of *coupling coefficient*¹⁵

$$\beta = \frac{(\omega M)^2}{Z_0 R_s} \frac{1}{[1 + (X_1/Z_0)^2]} = \beta_1 \frac{1}{[1 + (X_1/Z_0)^2]} = \frac{R_c}{R_s}, \quad (5.18)$$

therefore, from the principle of maximum transfer of power, it is clear that when $\beta = 1$ the coupled resistance and cavity losses are equal, and the cavity is said to be *critically* coupled. When $\beta < 1$ the cavity is said to be *undercoupled*; when $\beta > 1$, the cavity is called *overcoupled*.

It is worth note that under most circumstances, the term $[1 + (X_1/Z_0)^2]$ is nearly equal to unity and $\beta \approx \beta_1$. Moreover, The definition (5.16) can be written

$$Z = \beta R_s(1 - jX_1/Z_0), \quad (5.19)$$

The *loaded Q* value of the system is defined as the ratio of the total reactance to the total series loss. It is given by

$$Q_L = \frac{\omega L - \beta R_s X_1/Z_0}{R_s(1 + \beta)} = \frac{\omega L}{R_s} \frac{1 - (\beta R_s/Z_0)(X_1/\omega L)}{1 + \beta}, \quad (5.20)$$

and if it is valid that

- $\omega = \omega_0 = 1/\sqrt{LC}$,
- the *unloaded Q* is $Q_0 = \omega_0 R_s/L$, and
- $(\beta R_s/Z_0)(X_1/\omega L) \ll 1$,

then we can write the following relations

$$Q_L = \frac{Q_0}{1 + \beta}, \quad \frac{1}{Q_L} = \frac{1}{Q_0} + \frac{\beta}{Q_0}, \quad Q_{ext} = \frac{Q_0}{\beta}, \quad (5.21)$$

where Q_{ext} is called *external Q*. It is worth noting that at the critical coupling ($\beta \approx 1$), $Q_L \approx Q_0/2$.

7.3. Detuned short position. The solution of many problems involving resonant cavities can be simplified by considering, either graphically or numerically, the cavity input impedance in the complex impedance plane.

The impedance at the generic terminals $a - a'$ in figure 5.26 is equal to

$$\begin{aligned} Z_{aa'} &= jX_1 + \frac{(\omega M)^2}{R_s + j(\omega L - 1/\omega C)} \rightarrow \\ \frac{Z_{aa'}}{Z_0} &= j \frac{X_1}{Z_0} + \frac{\beta_1}{1 + j(\omega L/R_s)[1 - (\omega_0/\omega)^2]}. \end{aligned} \quad (5.22)$$

¹⁵It is worth note that β is the same symbol used for the speed of particles, namely $v = \beta c$; the significance should be apparent from the context.

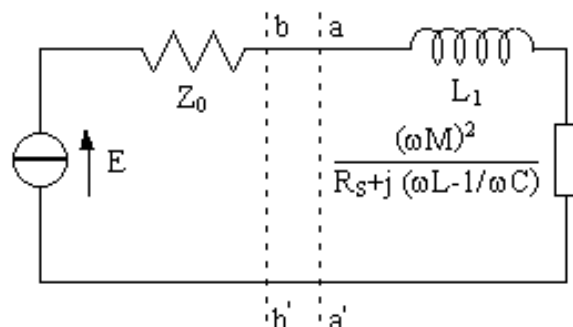


FIGURE 5.26. Coupling through an iris. The cavity is referred to the primary.

For cavities with high quality factor $\omega \approx \omega_0$ and then, equation (5.22) can be written as

$$\frac{Z_{aa'}}{Z_0} = j \frac{X_1}{Z_0} + \frac{\beta_1}{1 + j2Q_0\delta}, \quad \delta = \frac{\omega - \omega_0}{\omega_0}, \quad (5.23)$$

and the quantity δ is called the *frequency tuning parameter*. The second term of equation (5.23) corresponds to a circle on the complex impedance plane, where the first term expresses the effect of the self-reactance of the coupling system.

We can choose the reference planes along the transmission line at which the first term disappears and this series of positions are called the *detuned short positions*. Let the terminals $b - b'$ be selected at a distance l away from the terminals $a - a'$. The impedance $Z_{aa'}$ can be transformed in

$$\frac{Z_{bb'}}{Z_0} = \frac{Z_{aa'} + jZ_0 \tan \alpha l}{Z_0 + jZ_{aa'} \tan \alpha l}, \quad (5.24)$$

where α is the propagation number. The location of terminals $b - b'$ can be chosen so that the impedance at terminals $b - b'$ becomes zero when the cavity is detuned. This means that the impedance locus is symmetric respect to the real axis on the complex impedance plane, since the far points out of resonance are near the point where $R = \infty$.

7.4. RF procedure. In this section we derive a RF measurement recipe that implies only the use of a Network Analyzer. The used functions are so general that each specific model should have them.

- First, we assumed that the source of our cavity had an internal impedance Z_0 equal to the characteristic one of the transmission line used to feed the cavity in the previous relations. This implies that the network analyzer cables and the other tools used to feed the cavity right on to the coupling mechanism should be perfectly matched too.
- Then, we consider the measurement of reflection coefficient S_{11} and we use the Smith chart visualization of it. If the frequency

range is set around the resonance, the locus of impedance points describes a complete circle which should be seen on the display.

- Next, we use the phase offset option to make the circle symmetric respect to the real axis of Smith Chart. By this way, we put our point of view in a *detuned short position*.
- Last, we store the data on a diskette, in order to continue the procedure on a personal computer.

By using definitions (5.21), we can write

$$\begin{aligned} \frac{Z_{bb}}{Z_0} &= \frac{\beta}{1 + j2Q_0(\delta - \delta_0)} = \frac{\beta}{1 + j2Q_L(1 + \beta)(\delta - \delta_0)} \\ &= \frac{\beta}{1 + j2Q_{ext}\beta(\delta - \delta_0)}. \end{aligned} \quad (5.25)$$

By then, we use a matlab program that numerically finds the frequency points where the following relation occurs

$$\frac{Z_{bb}}{Z_0} = \frac{\beta}{1 \pm j},$$

and, in this case, it is true that $2Q_0(\delta - \delta_0) = \pm 1$. Let us call δ_1 and δ_2 the two points where they occur, then

$$Q_0 = \frac{1}{\delta_1 - \delta_2} = \frac{f_0}{f_1 - f_2}, \quad (5.26)$$

f_1 and f_2 are called *half power* points. In analogous way, we can find points where

$$\frac{Z_{bb}}{Z_0} = \frac{\beta}{1 \pm j(1 + \beta)} \rightarrow \frac{Y_{bb}}{Y_0} = G \pm jB = \frac{1}{\beta} \pm j\left(\frac{1}{\beta} + 1\right)$$

and, in this case, it is true that $2Q_L(\delta - \delta_0) = \pm 1$. Then, it is sufficient to find the points where $B = G + 1$, let us call δ_3 and δ_4 the two points where it occurs, next

$$Q_L = \frac{1}{\delta_3 - \delta_4} = \frac{f_0}{f_3 - f_4}, \quad (5.27)$$

Finally, we can find points where

$$\frac{Z_{bb}}{Z_0} = \frac{\beta}{1 \pm j\beta} \rightarrow \frac{Y_{bb}}{Y_0} = G \pm jB = \frac{1}{\beta} \pm j1$$

and, in this case, it is true that $2Q_{ext}(\delta - \delta_0) = \pm 1$. Then, it is sufficient to find the points where $B = 1$, let us call δ_5 and δ_6 the two points where it occurs, next

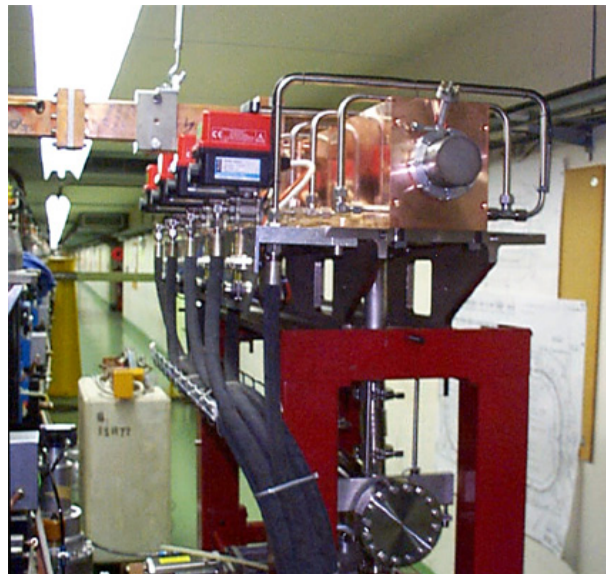
$$Q_{ext} = \frac{1}{\delta_5 - \delta_6} = \frac{f_0}{f_5 - f_6}, \quad (5.28)$$

Of course, this procedure could be manually carried out, by using Smith Chart. The relevant points are shown in figure 5.27. Finally,

Conclusions and Outlook

In this thesis the study and the development of the radiofrequency design of a module prototype for a linear accelerator intended to be used for hadrontherapy have been carried out. The aim was to proof the feasibility of such a structure in a not expensive way, together with the development of techniques to be used in a future industrial production. The conclusions to draw are on different levels and concern the various treated aspects.

Concerning the realized module prototype, the result was quite satisfactory. The following figure shows the successful installation of the prototype in the LIL area at Cern in Geneva in the first days of November 2000. The reached performances of the module were 25% better than what was expected.



This result means that the adopted design was sufficiently robust to support better performances and that some conservative approaches, as the one concerning the *bravery factor* for the Kilpatrick limit, could be relaxed in the next realization, leading to a shorter accelerator. This thing does not have to astonish the reader, since the first LIBO module was thought as a proof of principle and, from this point of view, it was realized *golden plated*.

Concerning the design procedure, the conclusion to draw is that the engineering procedures for an industrial production of this kind of structures still need lots of work to simplify the construction respect to the usual procedures used for the high energy physics linear accelerators. Even though, several innovative approaches have been carried out during the development.

First of all, the design steps have been rewritten with a top-down methodology. The best advantage of this approach should be the study of an equivalent circuit model before the detailed design of the mechanical pieces, as the tiles. In this case, one can fix the largest mechanical tolerances to satisfy the requested electromagnetic parameters of the structure.

This preliminary study can be carried out by using either a full numerical approach, as the one with Spice-like simulators, or a transmission matrix representation that easily allows a perturbation study of the structure. With this latter approach good results were reached.

Concerning the resonant frequency of a coupled cavities chain, the deviation depends only on the errors in the accelerating cavities, which are the charged ones for the mode $\pi/2$ mode. It is worth noting that this result was obtained only under the hypothesis of negligible non-adjacent cavities coupling, but it should be also true without the previous hypothesis, and leads to very interesting and simplified tuning procedure of such a structure: One could think to act on all the accelerating cavity frequencies of the same quantity, in order to change only the mean value. This point really simplified the tuning procedure.

About the flatness of the axial field, it was found a manageable formula that could be used in a numerical program that makes the permutation and use a mean square error as optimization parameter. Concerning this last point, it is worth noting that the errors in the cavities are experimentally measured and, as we stated before, they are affected by a measurement error. Therefore, the procedure of optimization is effective when the measurement error is proportionally smaller than the measured values.

The full numerical approach could be used as a further proof of the criteria expressed by the perturbation approach.

For the realization of the first LIBO prototype module, the radiofrequency measurement was the strongest tool of correction and understanding of the structure behaviour. With respect to the literature on the argument, the developed procedures seem to be easier and more understandable. A further consideration has to be made on the possibility to make automatic measurement: the use of simplified formulas, as the ones of the perturbation approach, together with a skilled use of a network analyzer, a personal computer and some motors, etc., should permit the realization of an automatic measurement station on these structures, where the man power would not be high qualified.

Finally, a comment on the next future possibility to make 6–11 GHz models of these structures. Actually, the optimization and measurement criteria should allow a feasible design without the requirement of stringent tolerances that should grow up the costs.

Bibliography

- [1] U. Amaldi and M. Silari editors, The TERA Project and the Centre for Oncological Hadrontherapy, The TERA Collaboration, Frascati, 1994.
- [2] U. Amaldi, M. Grandolfo and L. Picardi, The RITA Network and the Design of Compact Proton Accelerators, The TERA Collaboration, Frascati, 1996.
- [3] Mostra - Atomi per la Salute - La Fisica in Medicina e in Biologia, by W. Kienzle e A. Pascolini, CERN Ginevra; see also at <http://www.tera.it> for more information.
- [4] U. Amaldi and G. Tosi, Per un Centro di Teleterapia con Adroni, TERA Report 91/1, 1991.
- [5] G. Ising, Archiv of Mathematical Physics, **18** (No. 30), pp. 1 – 4, 1924.
- [6] R. Wideröe, Archiv für Elektrotechnik, **21**, p. 387, 1928.
- [7] L.W. Alvarez, Physical Review, **70**, p. 799, 1946.
- [8] L.W. Alvarez et al., Review of Scientific Instruments, **26**, p. 111, 1955 and p. 210, 1955.
- [9] L. Picardi, C. Ronsivalle and A. Vignati, Struttura SCDTL, Patent n.RM95-A000564, Owner ENEA, Italy.
- [10] L. Picardi, C. Ronsivalle and A. Vignati, Progetto del TOP Linac, ENEA Report, ISSN/1120 – 5571, 1997.
- [11] J.D. Jackson, Classical Electrodynamics, John Wiley & Sons, New York, 1998.
- [12] RF Engineering for particle accelerators, CERN Yellow report, CERN 92 – 03, vol. I and II, 1992.
- [13] P. Lapostolle and M. Weiss, Formulae and procedures useful for the design of linear accelerators, CERN-PS-2000 – 001 (DR), Geneva, 2000.
- [14] G. Dôme, in Linear Accelerators, P.M. Lapostolle and A.L. Septier editors, Wiley, New York, 1970.
- [15] P.M. Lapostolle, Proton Linear Accelerators: A Theoretical and Historical Introduction, Los Alamos Report LA-11601-MS, 1989.
- [16] T. Wangler, RF Linear Accelerators, John Wiley & sons, New York, 1998.
- [17] D.E. Nagle, E.A. Knapp and B.C. Knapp, Coupled resonator model for standing wave accelerator tanks, The Review of Scientific Instruments, (**38**)11, pp. 1583 – 1587, 1967.
- [18] E.A. Knapp, B.C. Knapp and J.M. Potter, Standing wave high energy Linear Accelerator Structures, The Review of Scientific Instruments, (**39**)7, pp. 979 – 991, 1968.
- [19] R.K. Cooper, Y. Iwashita, J.M. Potter, S.O. Schriber, D.A. Swenson, J.M. Watson, L.C. Wilkerson and L.M. Young, Radio-Frequency Structure Development for the Los Alamos/NBS Racetrack Microtron, LA-UR-83-95, LANL, Los Alamos, 1983.
- [20] M. Vretenar, private communication.
- [21] M. Weiss, private communication.
- [22] K. Crandall and M. Weiss, Preliminary Design of a Compact Linac for TERA, TERA Report 94/34 ACC20, 1994.

- [23] U. Amaldi, B. Szeless, M. Vretenar, E. Wilson, K. Crandall, J. Stovall and M. Weiss, LIBO - A 3 GHz Proton Linac Booster of 200 MeV for Cancer Treatment, Proceedings of LINAC98 Conference, Chicago, 1998.
- [24] P. Berra, S. Mathot, E. Rosso, B. Szeless, M. Vretenar, U. Amaldi, K. Crandall, D. Toet, M. Weiss, R. Zennaro, C. Cicardi, D. Giove, C. De Martinis, D. Davino, M.R. Masullo and V.G. Vaccaro, Study, Construction and Test of a 3 GHz Proton Linac-Booster (LIBO) for Cancer Therapy, Proceedings of EPAC2000 Conference, Wien, 2000.
- [25] P. Berra et al., Status of the LIBO Project, TERA Report 2000/3 ACC33, 2000.
- [26] W.D. Kilpatrick, Review of Scientific Instruments, vol. **28**, p. 824, 1957.
- [27] T.J.Jr. Boyd, Kilpatrick's Criterion, Los Alamos Group AT-1, Report AT-1:82 – 28, 1982.
- [28] A. Vladimirescu, The Spice Book, John Wiley & Sons, New York, 1994.
- [29] D.A. Swenson and C.R. Chang, Studies of a TM012 Bridge Coupler, Proceedings of LINAC92 Conference, Ottawa, 1992.
- [30] H. Henke and W. Wuensch, Computer Design of Iris Coupled Radio Frequency Structures, Clic note 108, CERN, 1990.
- [31] H. Hanaki, Numerical Design of an RF-Coupling Iris, LAL/RT 91 – 09, LAL, 1991.
- [32] S. Yamaguchi, Y. Igarashi, A. Enomoto and I. Sato, Design of Input and Output Couplers for Linear Accelerator Structures, Proceedings of LINAC92 Conference, Ottawa, 1992.
- [33] R.E. Collin, Foundations for Microwave Engineering, Mc Graw-Hill, New York, 1966.
- [34] E.L. Ginzton, Microwave Measurements, Mc. Graw-Hill, New York, 1957.
- [35] H. Araki, J. Ehlers, K. Hepp, R. Kippenhahn, D. Ruelle, H.A. Weidenmüller, J. Wess and J. Zittartz, Frontiers of Particle Beams; Observation, Diagnosis and Correction, Springer-Verlag, Berlin, 1989.
- [36] J.C. Slater, Microwave Electronics, D. Van Nostrand Company, Princeton, N.J., 1950.
- [37] L.C. Maier and J.C. Slater, Field Strength Measurements in Resonant Cavities, Journal of Applied Physics, **23**, pp. 68 – 83, 1952.
- [38] L. Picardi, C. Ronsivalle and B. Spataro, Numerical studies and measurements on the side coupled drift tube linac (SCDTL) accelerating structure, Nuclear Instrumentation and Method in Physical Research B, NIMB **170**, pp. 219–229, 2000.

List of Figures

1.1	The Bragg peak phenomenon. Comparison between proton and electron penetration depth in water. Also shown is a proton depth dose curve with a spread-out Bragg (SOBP) of 5 cm.	4
1.2	The Spread out Bragg peak. Combining beams with different energies it is possible to describe a longitudinal profile.	5
1.3	A sketch of Loma Linda radiotherapy center in California.	5
2.1	Dispersion diagram of a periodic structure (loaded waveguide); unloaded cavity case is shown for comparison.	8
2.2	$N + 1$ coupled cavities. The first and last cells are half cavities which act as an <i>electric mirror</i> for the boundary conditions.	9
2.3	$N = 7$ coupled cavities. The Brillouin diagram is sampled in 7 frequencies. We can recognize modes 0, $\pi/2$ and π .	10
2.4	Schematic view of the Wideröe drift-tube linac.	12
2.5	Schematic view of the Alvarez drift-tube linac.	13
2.6	Schematic view of the Side Coupled Drift-Tube Linac.	14
2.7	Different solutions for the realization of a biperiodic chain of cavities.	15
2.8	A Side Coupled Linac example.	15
2.9	The dispersion diagrams in the case of a biperiodic structure with $f_a = 3$ GHz, $f_c = 3$ GHz, $k = 0.04$, $k_2 = 0.005$ and $k_3 = 0$ on the left and $f_c = f_a/\sqrt{1 - k_2}$ on the right.	16
2.10	A perspective image of a LIBO installation.	17
2.11	The layout of the first module of LIBO, with details of a half-cell-plate (left) and of a bridge coupler (right).	18

2.12	Drawing of the first tank of first LIBO module (left). The first tank after the brazing (right).	18
2.13	Half-cell-plates showing a coupling half cell (left) and an accelerating half cell (right). Note the coupling slot.	18
3.1	Schematic view of a Linac.	23
3.2	The design of a Linac with a top-down methodology.	24
3.3	The behavior of Kilpatrick formula 3.1.	26
3.4	The equivalent circuit for two half cavities coupled through a cavity with different parameters (coupling cell).	28
3.5	Spice simulation for a periodic chain without next nearest neighbor coupling.	30
3.6	Spice simulation for a periodic chain without next nearest neighbor coupling. The coupling cavities are nominally uncharged.	30
3.7	Spice simulation for a periodic chain with next nearest neighbor coupling.	31
3.8	Spice simulation for a biperiodic chain with next nearest neighbor coupling.	31
3.9	Particulars of the machinable ring and of the tuning rod hole for the coupling cavities (top) and for the accelerating cavities (down).	34
3.10	Schematic view of the Bridge Coupler functionality.	35
3.11	The LIBO Bridge Coupler with the feeding waveguide.	36
3.12	Coupling between the waveguide and Bridge Coupler. The structure simulated with MAFIA having two waveguides and one cavity.	38
3.13	The equivalent circuit of the structure simulated with MAFIA. Two transmission lines and a purely reactance.	39
3.14	An example of reactance coming from MAFIA. The iris has dimensions $35 \times 10 \times 2$ mm (model made in Naples).	39
3.15	The equivalent circuit of the reactance X_i of the coupling mechanism (left) and a possible equivalent circuit from the cavity point of view (right).	40
3.16	The final equivalent circuit for a cavity seen from the waveguide through the iris.	41

3.17	The Reactance of a $41 \times 10 \times 2$ mm iris. The dashed line interpolates the circles that are Superfish points. The continuous line interpolates points from Mafia.	43
3.18	Dependence of Γ on d2 (left). Dependence of Γ on C1 (right).	43
4.1	A generic two-ports network.	45
4.2	The equivalent circuit for a single cell representing two magnetically coupled half cavities.	46
4.3	The two-ports representing two coupled half cavities with different parameters.	52
4.4	The relative level of field in the cavities in the unperturbed case.	62
4.5	The relative level of field in the cavities for a generic disposition of the cavities.	65
4.6	The relative level of field in the cavities for the best disposition of the cavities	66
5.1	The flux diagram of the measurement and machining procedure.	68
5.2	Electric pick-up (up) and Magnetic loop (down) for radiofrequency measurement in cavities.	70
5.3	Mechanical tools for RF measurement on the LIBO tiles. On the top right the use of these tools is shown.	71
5.4	The dispersion of frequencies before and after two steps of machining on the rings for the accelerating and coupling half cavities in the tank #1.	73
5.5	The change in frequency due to a metallic plunger for the measurement of r over Q .	75
5.6	The result of the line method applied to two coupled cavities.	77
5.7	The result of parabola method applied to two coupled cavities.	78
5.8	Measurement on a stacked CC using the rods.	80
5.9	Measurement on a stacked AC using the rods.	80
5.10	Measurement for the coupling for stacked cavities. In order to apply line and parabola methods, in addition to the AC and CC screws, one can move also (*) rod to change the CC frequency.	81
5.11	Measurement for the second order coupling for stacked cavities. In order to apply line and parabola	

	methods, in addition to the AC and CC screws, you can move also (*) rod to change the CC frequency.	81
5.12	Sketch of a bead pulling measurement apparatus.	83
5.13	The particular realization of the bead pulling measurement for the LIBO module.	84
5.14	The bead pulling result after the bridge couplers tuning.	85
5.15	The bead pulling result after the first operation on tank #1.	87
5.16	The bead pulling result before the first operation on all the CCs.	87
5.17	The bead pulling result after the first operation on all the CCs.	88
5.18	The bead pulling result for the tuners positions of table 5.2.	88
5.19	The first good bead pulling result.	89
5.20	A bead pulling with the field level flat within $\pm 2.85\%$.	90
5.21	The final bead pulling with the field level flat within $\pm 2.5\%$.	90
5.22	The effect of perturbations a) in the end cell, b) in 6 CCs (two for tank), c) in 2 ACs in tank #2, d) in all the ACs of tank #3.	91
5.23	The effect of local perturbations in the CCs at the end of a tank.	92
5.24	Coupling through an iris. Sketch of a resonant cavity coupled with a transmission line.	93
5.25	Coupling through an iris. The generator is referred to the secondary.	93
5.26	Coupling through an iris. The cavity is referred to the primary.	95
5.27	Identification of the half-power points from the Smith chart. Q_0 locus is given by $X = R$ ($B = G$); Q_L by $B = G + 1$ and Q_{ext} by $B = 1$.	97

Acknowledgements

I start these acknowledgements thanking Loredana Lombardi, the only person who always gives me her support in a non-trivial and non-conventional way, acting as a real friend and this is not bad for a *girlfriend*.

A scientific work, which has not only theoretical but also technological and experimental aspects, cannot be ascribed to one person, and also this Ph.D. thesis confirms this rule. It contains the contribution of some people that I would like to thank in the following.

In first place, I would like to thank Prof. Vittorio G. Vaccaro who gives me the opportunity to join in the LIBO project where I found lots of professional satisfaction.

At CERN, I found always a comfortable environment from the human point of view, and stimulating challenges from the intellectual point of view. For these reasons I would like to thank Prof. Ugo Amaldi, Ettore Rosso, Balazs Szeless, Maurizio Vretenar and Riccardo Zennaro. In particular I thank Mario Weiss, the project leader: I really appreciated his professionalism, together with his kindness and distinction. Also I cannot forget the hospitality of Paolo Berra, who provides me a *roof on the head* for those times I was not able to find anyone.

At INFN Sez. di Napoli, I worked with Iaia Masullo, a physicist, and this was for me an important experience. She has been improved both my experimental attitude and my mood with her catching joy. Also thanks to all the administrative people, in particular Mrs. Mariella Russo, for their kindness answers to my requests.

At the Department of Electrical Engineering in Naples, I found always a pleasant environment and valid people. I would thank all of them and in particular Amedeo Andreotti, Lorenza Corti, Massimiliano de Magistris, Antonio Maffucci, Giovanni Miano, Giovanni Rumolo, Claudio Serpico and Ciro Visone. I would thank also Prof. Luciano De Menna, my tutor, who follows me in this project with a great passion, working with me side by side. Finally, I thank Luigi Verolino: he was not directly involved in the project, but he was always able to utilize my *free* time with interesting researches and nice collaborations, always driven in a genuine and *invasing* way! A sincere thanks also to Fulvio Schettino for his friendship.

Last but not least, I am grateful to my parents for their patience, love and for the way they have always accepted my decisions.

Naples, Italy
November 30, 2000

Daniele DAVINO